MASTER

Finite element simulation of extensional-flow-induced crystallization in a filament stretching rheometer
modeling of isotactic polypropylene

van Berlo, Frank P.A.

Award date:
2019

Finite element simulation of extensional-flow-induced crystallization in a filament stretching rheometer

modeling of isotactic polypropylene

Master thesis

By: Van Berlo, F.P.A.
                 0893564

Supervisors: prof. dr. ir. Anderson, P.D.
                  dr.ir. Cardinaels, R.M.

Winter - Autumn 2019

Contents

Nomenclature

<u>Abbreviations</u>

FIC	Flow-induced crystallization
FiSER	Filament stretching extensional rheometer
HDPE	High-density polyethylene
HMW	High molecular weight
iPP	Isotactic polypropylene
LLDPE	Linear low-density polyethylene
SAXS	Small-angle X-ray scattering
SER	Sentmanat extensional rheometer
WAXD	Wide-angle X-ray diffraction
XPP	eXtended Pom-Pom (constitutive equation)

<u>List of symbols</u>

α	pressure constant of a phase	$[\mathrm{kg^{-1}\,m\,s^2}]$
α_s	stretch relaxation time coefficient (flow)	$[\mathrm{m^{-3}}]$
$\bar{\eta}$	extensional viscosity	$[\mathrm{kg\,m^{-1}\,s^{-1}}]$
$\bar{\eta}^+$	transient extensional viscosity	$[\mathrm{kg\,m^{-1}\,s^{-1}}]$
$\bar{\eta}_a^+$	apparent transient extensional viscosity	$[\mathrm{kg\,m^{-1}\,s^{-1}}]$
$\bar{\eta}_c^+$	corrected transient extensional viscosity	$[\mathrm{kg\,m^{-1}\,s^{-1}}]$
$\bar{\eta}_R^+$	real transient extensional viscosity	$[\mathrm{kg\,m^{-1}\,s^{-1}}]$
$\bar{\eta}_{\mathrm{LVE}}^+$	linear viscoelastic transient extensional viscosity	$[\mathrm{kg\,m^{-1}\,s^{-1}}]$
$\bar{\eta}_{\mathrm{Old\text{-}B}}^+$	pure uniaxial extensional viscosity using the Oldroyd-B model	$[\mathrm{kg\,m^{-1}\,s^{-1}}]$
$\bar{\eta}_{\mathrm{XPP}}^+$	pure uniaxial extensional viscosity using the XPP model	$[\mathrm{kg\,m^{-1}\,s^{-1}}]$
β_s	stretch relaxation time coefficient (X-ray)	$[\mathrm{m^{-3}}]$
$\boldsymbol{\Lambda}$	stretch tensor	$[-]$
$\boldsymbol{\sigma}$	Cauchy stress tensor	$[\mathrm{kg\,m^{-1}\,s^{-2}}]$
$\boldsymbol{\tau}$	extra stress tensor	$[\mathrm{kg\,m^{-1}\,s^{-2}}]$
$\boldsymbol{c}_i$	i-th mode conformation tensor	$[-]$
$\boldsymbol{c}_{\mathrm{HMW}}$	conformation tensor of the highest mode	$[-]$
$\boldsymbol{D}$	rate of deformation tensor	$[\mathrm{s^{-1}}]$
$\boldsymbol{d}$	displacement vector	$[\mathrm{m}]$
$\boldsymbol{F}$	deformation tensor	$[-]$
$\boldsymbol{f}$	right-hand-side force vector	$[\mathrm{kg\,m\,s^{-2}}]$
$\boldsymbol{f}_r$	residual force vector	$[\mathrm{kg\,m\,s^{-2}}]$
$\boldsymbol{F}_{\mathrm{reac}}$	reaction force vector	$[\mathrm{kg\,m\,s^{-2}}]$
$\boldsymbol{F}_s$	free surface force vector	$[\mathrm{kg\,m\,s^{-2}}]$
$\boldsymbol{K}$	stiffness tensor	$[\mathrm{kg\,s^{-2}}]$
$\boldsymbol{n}$	normal vector	$[-]$
$\boldsymbol{u}$	velocity vector	$[\mathrm{m\,s^{-1}}]$
$\boldsymbol{x}$	position vector	$[\mathrm{m}]$
$\Delta\varepsilon_z^{ff}$	feed-forward strain contribution	$[-]$
ΔH	heat of fusion	$[\mathrm{m^2\,s^{-2}}]$
ΔN_f^*	difference of dimensionless amount of flow-induced nuclei	$[-]$
Δt	time step	$[\mathrm{s}]$
Δt_{max}	maximum time step	$[\mathrm{s}]$
$\dot{\gamma}$	shear rate	$[\mathrm{s^{-1}}]$
$\dot{\gamma}_{\mathrm{eff}}$	magnitude of the rate of deformation tensor	$[-]$
$\dot{\varepsilon}$	strain rate	$[\mathrm{s^{-1}}]$
$\dot{\varepsilon}_{\mathrm{eff}}$	effective strain rate	$[-]$

$\dot{L}$	lengthwise propagation of shish	$[\mathrm{m\,s^{-1}}]$
ϵ_F	error of force simulation	$[-]$
η	shear viscosity	$[\mathrm{kg\,m^{-1}\,s^{-1}}]$
η_0	zero-shear viscosity	$[\mathrm{kg\,m^{-1}\,s^{-1}}]$
η_i	i-th mode viscosity	$[\mathrm{kg\,m^{-1}\,s^{-1}}]$
η_s	solvent viscosity	$[\mathrm{kg\,m^{-1}\,s^{-1}}]$
η_{LVE}	linear viscoelastic shear viscosity	$[\mathrm{kg\,m^{-1}\,s^{-1}}]$
Γ	boundary	$[-]$
$\hat{\gamma}$	surface tension	$[\mathrm{kg\,s^{-2}}]$
κ	pressure shift constant	$[\mathrm{kg^{-1}\,m\,s^2}]$
λ	relaxation time	$[\mathrm{s}]$
Λ_0	initial aspect ratio	$[-]$
λ_b	backbone relaxation time	$[\mathrm{s}]$
Λ_c	compressed aspect ratio	$[-]$
λ_c	characteristic relaxation time	$[\mathrm{s}]$
Λ_i	i-th mode molecular backbone stretch	$[-]$
λ_k	thermal conductivity coefficient	$[\mathrm{kg\,m\,s^{-3}\,K^{-1}}]$
λ_s	stretch relaxation time	$[\mathrm{s}]$
Λ_{HMW}	molecular backbone stretch of the highest mode	$[-]$
λ_G	chain relaxation time after flow pulse	$[\mathrm{s^{-1}}]$
$\mathcal{X}$	crystallinity	$[-]$
$\mathcal{X}_\infty$	crystallinity at equilibrium state	$[-]$
$\mathcal{X}_{\mathrm{tot}}$	total crystallinity	$[-]$
μ	ratio of the modulus of the crystal and the melt	$[-]$
μ_n	nucleation rate scaling parameter	$[-]$
∇_s	surface gradient operator	$[-]$
ν_i	i-th mode non-linearity parameter (XPP model)	$[-]$
Φ_j	quiescent crystal volume (0), -surface (1), -radius (2) and -rate (3)	
Ψ_j	flow-induced crystal volume (0), -surface (1), -radius (2) and -rate (3)	
ρ_0	initial density	$[\mathrm{kg\,m^{-3}}]$
ρ_k	density of material k	$[\mathrm{kg\,m^{-3}}]$
Bo	Bond number	$[-]$
Ca	capillary number	$[-]$
De	Deborah number	$[-]$
Nu	Nusselt number	$[-]$
Re	Reynolds number	$[-]$
Wi	Weissenberg number	$[-]$
θ	angle between the piston and the free surface	$[\mathrm{rad}]$
ε	mid-radius based strain	$[-]$
ε_H	Hencky strain	$[-]$
ε_z	length based strain	$[-]$
$\varepsilon_{\mathrm{ideal}}$	ideal mid-radius based strain	$[-]$
$\varepsilon_{\mathrm{meas}}$	measured mid-radius based strain	$[-]$
$\varepsilon_{\mathrm{pre}}$	pre-strain	$[-]$
ε_c	critical crystallization strain	$[-]$
ξ	space filling	$[-]$
ξ_∞	space filling at equilibrium state	$[-]$
ξ_{seg}	chain segment length	$[\mathrm{m}]$
ξ_{tot}	total space filling	$[-]$
ζ	pressure dependence of the melting temperature	$[\mathrm{K\,kg^{-1}\,m\,s^2}]$
a, b, c	fitting parameters	
A^e	area of an element	$[\mathrm{m^2}]$
A_0^e	intial area of an element	$[\mathrm{m^2}]$

a_p	pressure shift factor	$[-]$
a_T	temperature shift factor	$[-]$
b_s	slope of the difference of dimensionless amount of flow-induced nuclei in time	$[\mathrm{s}^{-1}]$
c_G	growth rate constant of a phase	$[\mathrm{K}^{-1}]$
c_N	nucleation density rate constant	$[\mathrm{K}^{-1}]$
c_p	specific heat at constant pressure	$[\mathrm{kg\,s}^{-2}\,\mathrm{m}^2\,\mathrm{kg}^{-1}\,\mathrm{K}^{-1}]$
c_b	coefficient in radiation-induced nucleation rate equation (X-ray)	$[\mathrm{kg\,s}^{-3}]$
$c_{n,p}$	pressure dependent scaling parameter	$[\mathrm{kg}^{-1}\,\mathrm{m\,s}^2]$
$c_{n,T}$	temperature dependent scaling parameter	$[\mathrm{K}^{-1}]$
E_a	activation energy	$[\mathrm{kg\,s}^{-2}\,\mathrm{m}^2\,\mathrm{mol}^{-1}]$
f	growth rate fraction	$[-]$
f_1^e	change in area of an element	$[-]$
f_2^e	change in aspect ratio of an element	$[-]$
f_f	flow-induced growth rate fraction	$[-]$
f_q	quiescent growth rate fraction	$[-]$
F_{drag}	drag force	$[\mathrm{kg\,m\,s}^{-2}]$
F_{piston}	force on bottom piston	$[\mathrm{kg\,m\,s}^{-2}]$
f_{shear}	shear correction factor	$[-]$
G	growth rate	$[\mathrm{m\,s}^{-1}]$
g	gravitational acceleration on earth	$[\mathrm{m\,s}^{-2}]$
g_i	i-th mode relaxation strength	$[-]$
g_n	pressure and temperature dependent scaling parameter	$[\mathrm{s}^{-1}]$
G_{flow}	kebab growth rate increase after flow pulse	$[\mathrm{s}^{-1}]$
G_{max}	maximum growth rate	$[\mathrm{m\,s}^{-1}]$
$g_{n,\mathrm{ref}}$	reference pressure and temperature dependent scaling parameter	$[\mathrm{s}^{-1}]$
h	element size	$[\mathrm{m}]$
h_k	convection coefficient	$[\mathrm{kg\,s}^{-3}\,\mathrm{K}^{-1}]$
h_{ini}	initial element size at the piston boundary	$[\mathrm{m}]$
h_{mid}	element size at the mid-radius of the sample	$[\mathrm{m}]$
i	index number	$[-]$
I_b	intensity of the X-ray beam	$[\mathrm{kg\,s}^{-3}]$
J	Jacobian	$[-]$
K	compression modulus	$[\mathrm{kg\,m}^{-1}\,\mathrm{s}^{-2}]$
K_i	integral gain	$[-]$
K_p	proportional gain	$[-]$
L	length of a sample	$[\mathrm{m}]$
L_0	initial length of the sample after pre-stretching	$[\mathrm{m}]$
L_c	length of compressed sample	$[\mathrm{m}]$
L_i	length of cylindrical sample	$[\mathrm{m}]$
L_p	length of the pistons	$[\mathrm{m}]$
L_{max}^e	maximum length of the sides of an element	$[\mathrm{m}]$
L_{tot}	specific shish length	$[\mathrm{m}^{-2}]$
M_n	number-average molecular weight	$[\mathrm{kg\,mol}^{-1}]$
M_w	weight-average molecular weight	$[\mathrm{kg\,mol}^{-1}]$
N	nucleation density	$[\mathrm{m}^{-3}]$
N_b	radiation-induced nucleation density (X-ray)	$[\mathrm{m}^{-3}]$
N_f	flow-induced nucleation density	$[\mathrm{m}^{-3}]$
N_q	quiescent nucleation density	$[\mathrm{m}^{-3}]$
n_{ini}	initial amount of elements at the piston boundary	$[-]$
n_{mid}	amount of elements at the mid-radius of the sample	$[-]$
N_{ref}	number of nuclei at the reference temperature $T_{N,\mathrm{ref}}$	$[\mathrm{m}^{-3}]$
N_{tot}	total nucleation density	$[\mathrm{m}^{-3}]$
p	pressure	$[\mathrm{kg\,m}^{-1}\,\mathrm{s}^{-2}]$

p_0	initial pressure	$[\mathrm{kg\,m^{-1}\,s^{-2}}]$
p_{ref}	reference pressure	$[\mathrm{kg\,m^{-1}\,s^{-2}}]$
q	proportion of units cross-linked	$[-]$
q_0	proportion of units cross-linked per unit of radiational doses	$[\mathrm{m^{-2}\,s^2}]$
q_i	i-th mode non-linearity parameter (XPP model)	$[-]$
R	radius of the middle of the filament	$[\mathrm{m}]$
r	radial position	$[\mathrm{m}]$
R^*	universal gas constant	$[\mathrm{kg\,s^{-2}\,m^2\,mol^{-1}\,K^{-1}}]$
r^*	dimensionless radial position at $z = 0$	$[\mathrm{m}]$
R_0	initial radius of middle of the sample after pre-stretching	$[\mathrm{m}]$
R_c	radius of the compressed sample	$[\mathrm{m}]$
R_i	radius of the cylindrical sample	$[\mathrm{m}]$
R_p	radius of the pistons	$[\mathrm{m}]$
r_{eff}	effective radius of a shish	$[\mathrm{m}]$
R_{ideal}	ideal radius of the middle of the filament	$[\mathrm{m}]$
R_{Xray}	dose of X-ray radiation	$[\mathrm{m^2\,s^{-2}}]$
S	surface	$[-]$
S^e	aspect ratio of an element	$[-]$
S_0^e	initial aspect ratio of an element	$[-]$
T	temperature	$[\mathrm{K}]$
t	time	$[\mathrm{s}]$
T_0	initial temperature	$[\mathrm{K}]$
T_∞	temperature of the environment	$[\mathrm{K}]$
T_{ref}	reference temperature	$[\mathrm{K}]$
$T_{G,\mathrm{ref}}$	reference temperature of the growth rate function of a phase	$[\mathrm{K^{-1}}]$
$T_{N,\mathrm{ref}}$	reference temperature of the nucleation density function	$[\mathrm{K^{-1}}]$
V	volume of a sample	$[\mathrm{m^3}]$
v_{eff}	effective space filling of shish-kebab	$[\mathrm{m^{-3}}]$
v_{piston}	piston velocity	$[\mathrm{m\,s^{-1}}]$
z	axial position	$[\mathrm{m}]$

Abstract

A finite element model is presented to describe the flow, resulting stresses and crystallization of an isotactic polypropylene in a filament extensional stretching rheometer. This model incorporates non-linear viscoelasticity, compressibility, non-isothermal process conditions due to shear heating and heat release due to crystallization and the effect of crystallization on relaxation times and viscosity. Also a radius-based controller is added to mimic the typical extensional flow in a filament stretching rheometer. The model is validated by comparing force simulations with measurements and analytical solutions. The first part of this work involves the investigation of shear effects in the extensional flow. Herein, a correction factor for the shear effects in the non-linear viscoelastic flow regime is derived. This shear correction factor shows good agreement with simulations performed at multiple aspect ratios, strain rates and (non-linear) rheological parameters (materials). In the second part, the onset of crystallization in a filament stretching rheometer is investigated. Here it is shown that even before crystallization starts, the rheology of the material changes because of flow-induced nucleation. Besides, multiple simulations are performed to find the relation between of the onset of crystallization and aspect ratio, temperature and strain rate. In the last part, the effect of radiation (X-ray) on crystallization in a filament stretching rheometer is investigated. In this part, the previously described model is extended by introducing a relation for radiation-based cross-linking. These results are compared, in a qualitative sense, to experiments performed at a synchroton X-ray radiation facility.

1   Introduction

Polyethylene and polypropylene are two polymers of major industrial importance [1, 2]. They are two of the most widely used plastics. Although crystallization of these polymers has been studied for more than sixty years [3–8], many questions are still unanswered. While their chemical structure is simple, the crystal types and relation with the morphologies formed during processing are complex and not well-understood. Therefore, a wide range of processing techniques are developed to obtain different structures and morphologies which consequently result in distinctly different physical properties.

Flow is known to facilitate crystallization of polymers through alignment and deformation of entangled tubes of constrained polymer chains [5]. Compared with shear, extension is much stronger to deform polymer chains and hence to facilitate crystallization [9]. Therefore, it is relevant to investigate the extensional *flow-induced crystallization* (FIC). To measure extensional properties of polymers, many measuring techniques have been developed over the years. Examples of these measuring techniques are fiber spinning [10], contraction flows in extrusion dies [11], filament stretching rheometry [12] and Sentmanat extensional rheometry [13]. In literature it has been shown that for example with the *Sentmanat extensional rheometer* (SER) and the *filament stretching extensional rheometer* (FiSER) it is possible to obtain information about extensional flow-induced crystallization of polymers. Sentmantat et al. [14] studied the crystallization of an ethylene-based butane plastomer in a SER, while White et al. [15] performed ex-situ crystallization measurements in a *filament stretching extensional rheometer* FiSER. Within our group, a special type of FiSER is developed to measure in-situ extensional flow-induced crystallization [16]. With this FiSER, it is possible to measure the morphology of crystalline polymers in extension by in-situ *wide-angle X-ray diffraction* (WAXD) and *small-angle X-ray scattering* (SAXS) measurements.

Since it is difficult to perform controlled and local measurements of crystallinity, especially within industrial equipment devices, it is interesting to have numerical models that can predict crystallization during processing. This also holds for the FiSER developed within our group, because only at specific processing conditions crystallization can be measured [16]. Recently, Roozemond et al. presented a numerical model which captures both rheology and crystallization of *isotactic polypropylene* (iPP) at high shear rates [17, 18]. In these papers, the rheology and crystallization of iPP is fully characterized, modeled and implemented in a finite element package, developed within our group [19]. This model shows good agreement with experimental data for crystallization over a very wide range of shear rates, pressures and temperatures [18].

1.1 Scope and outline

In this thesis, the focus will be on the development and use of finite element simulations of the FiSER, which can capture rheology, flow and crystallization of iPP. Three goals are formulated:

- The fist goal is to develop finite element simulations that can predict the flow of iPP in the filament stretching rheometer. With these simulations, the extensional flow and resulting stresses on the pistons will be investigated and recommendations will be given about the correction of shear contributions of non-linear polymers in the FiSER.

- The second goal is to develop finite element simulations that can predict extensional flow-induced crystallization in the FiSER for iPP. To do so, a crystallization model, derived from the model of Roozemond et al. [17] and Grosso et al. [20], is used to investigate the effect of strain rate and temperature on the crystallization in the FiSER. With these results, advise can be given about performing extensional flow-induced crystallization measurements in the FiSER.

- At last, the finite element simulations are compared with in-situ crystallization measurements of the FiSER. Here, a *high molecular weight* (HMW) iPP will be used. The goal is to validate the crystallization model of Grosso et al. [20] in extensional flows and to point out some improvement for this crystallization model.

In Chapter 2, the investigation concerning the first goal is reported. Here, the shear contribution in the are investigated. Chapter 3 reports on the second goal. Herein, the extensional flow-induced crystallization simulations of the FiSER are shown for different aspect ratios, strain rates and temperatures. Next, in Chapter 4, in-situ crystallization measurements are compared with simulations of the FiSER (see the third goal), whereby an extension of the crystallization model of the HMW iPP is introduced. Finally, the main conclusions of the work are reiterated in Chapter 5 and recommendations for future work are given.

2 Modelling the effect of shear contributions on extensional viscosity measurements in a filament stretching rheometer

2.1 Introduction

2.1.1 Test protocol

A wide range of techniques can be used to obtain information about the properties of polymers. A rheometer used to characterize polymers in extension is the filament stretching extensional rheometer. Measurements done with the FiSER aim to create a purely uniaxial extensional flow. With this simple flow, the uniaxial extensional viscosity of a polymer sample can be determined. This material property is widely used in polymer processing to characterize the material behaviour in extensional flow.

The processes of stretching a polymer sample in the FiSER is shown in Figure 2.1. The process starts with an initial cylindrical sample with a radius R_i and length L_i. This sample has to stick to the bottom and top piston. Therefore, the sample is slightly compressed to a length L_c. The aspect ratio of this compressed sample is defined as $\Lambda_c = L_c/R_c$, with R_c the radius of the sample after compression. The initial aspect ratio of a sample determines the flow type at the start of the experiment (34). Therefore, it is common to "slowly" pre-stretch the sample to a length L_0. This increases the initial aspect ratio to $\Lambda_0 = L_0/R_0$, where R_0 is the mid-radius of the sample after pre-stretch. Subsequently, the pistons are simultaneously moved apart to a length $L(t)$ (with a velocity $v_{\text{piston}}(t)$), in such a way that the middle of the sample is extended with a constant strain rate. Eventually, the mid-radius of the filament, $R(t)$, will become so small that the sample breaks. This type of filament stretching experiment was firstly discussed by Kolte et al. [12].
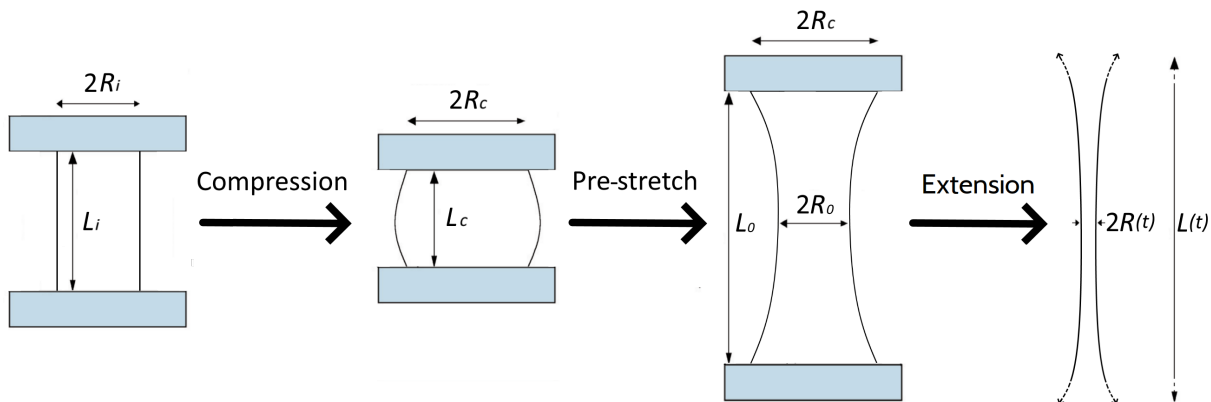
Figure 2.1: Schematic drawing of the process of stretching a polymer sample in our filament stretching rheometer. The pistons are simultaneously moved apart in opposite direction.

2.1.2 Theory on filament stretching rheometry

It is assumed that the geometry of the sample is axisymmetric. A steady uniaxial extensional flow, which is desired in the FiSER, is then described by the following velocity field:

$$u_r(t) = -\dot{\varepsilon}r/2 \tag{1}$$
$$u_z(t) = \dot{\varepsilon}z, \tag{2}$$

where, u_r and u_z are the radial and axial velocity respectively and $\dot{\varepsilon}$ is the instantaneous constant rate of extension. Likewise, r and z are the radial and axial position respectively. The equations above are

reformulated in terms of the evolution of a fluid particle position in the following equations:

$$r(t) = r(t') \exp(\varepsilon(t', t)/2), \tag{3}$$

$$z(t) = z(t') \exp(\varepsilon(t', t)), \tag{4}$$

where $\varepsilon(t', t)$ is the strain experienced by a fluid element from time t' to t. For polymer melts subjected to a deformation, the stress is a function of the whole deformation history. A logarithmic definition of the strain is used, because it is a consistent way of describing the strain path of a fluid element. For this constant strain rate, the logarithmic strain (Hencky strain) is given by:

$$\varepsilon(t', t) = \dot{\varepsilon} \cdot (t' - t), \tag{5}$$

The Hencky strain is the strain definition used throughout the rest of the report. The desired material function is the transient extensional viscosity, $\bar{\eta}^+$, as a function of time and strain rate. This material function is defined as the average stress difference divided by the strain rate:

$$\bar{\eta}^+(t, \dot{\varepsilon}) = \frac{\langle \sigma_{zz}(t) - \sigma_{rr}(t) \rangle}{\dot{\varepsilon}}, \tag{6}$$

where $\boldsymbol{\sigma}$ is the total-stress tensor for a fluid undergoing homogeneous uniaxial extensional flow; σ_{zz} and σ_{rr} are the total-stress in radial and axial direction. As time increases, the transient extensional viscosity may reach a steady-state value, $\bar{\eta}$. The (steady-state) extensional viscosity is a material property of the fluid and is a function of only the strain rate (and temperature).

To mimic the velocity field of the uniaxial extension in a filament stretching rheometer, a fluid sample is placed between two circular pistons (see Figure 2.2). For a (theoretical) uniaxial extension, the mid-radius of the sample has to decrease exponentially in time:

$$R(t) = R_0 \exp\left(-\frac{1}{2}\varepsilon(t)\right), \tag{7}$$

with ε the mid-radius based Hencky strain. Theoretically, the pistons should be moved apart so that the gap between the plates increases exponentially in time. To do so, the pistons have to move simultaneously with the same (opposite) velocity:

$$v_{\text{piston}}(t) = \dot{\varepsilon}_z L(t)/2 = \dot{\varepsilon}_z L_0 \exp(\varepsilon_z(t))/2, \tag{8}$$

wherein, ε_z is the length based Hencky strain and $\dot{\varepsilon}_z$ the length based Hencky strain rate. In theory, this length based Hencky strain ε_z and the radius based Hencky strain ε are equal. In reality however, due to the lack of uniformity of the flow along the axis of extension, the length based Hencky strain and the radius based Hencky strain are not the same. As a result, the radius is not decreasing exponentially and the effective strain rate at the middle of the sample is not constant during the flow. Therefore, a strain based controller is developed by Marin et al. [21], which adjusts the piston velocity so that the mid-radius of the sample decreases exponentially in time. This controller will be explained in more detail in Section 2.3.2.

Beside the mid-radius, also the force acting on one of the pistons is measured in the FiSER. By performing a force balance on the filament, the apparent transient extensional viscosity can be related to this force and the mid-radius by [22]:

$$\bar{\eta}_a^+(t, \dot{\varepsilon}) = \frac{F_{\text{piston}}(t)}{\pi R^2(t)\dot{\varepsilon}}, \tag{9}$$

where F_{piston} is the axial force on the bottom piston. The subscript a is used, because this apparent extensional viscosity is not corrected for physical phenomena like gravity and surface tension.

4

2.1.3 Shear contributions in the filament stretching rheometer

Though, it is theoretically possible to perform a uniaxial extension with a FiSER, this is not the case in reality. One of the issues is that the polymer sample is connected to two pistons. The sample sticks to the pistons forming no-slip boundary conditions. These boundary conditions give rise to radial pressure variations near the pistons. Therefore, a shearing flow is introduced, which can significantly affect the measured extensional viscosity at the start of the experiment ($\varepsilon_H < 1.5$) [23]. After a Hencky strain of approximately 1.5, locally (at the middle of the sample) a uniaxial extension flow develops and the extensional viscosity measured at the plates grows to the theoretical pure uniaxial extensional viscosity [23].

In this part of the report, the shear contributions are investigated by means of numerical simulations. The model used to simulate the FiSER will be explained in Section 2.2. Subsequently in Section 2.3, the method to measure the shear contributions with the numerical model are described. Thereafter in Section 2.4, results are shown from the numerical model. Here, a validation of the numerical simulations is given, which is followed by results of the numerical measurements of the shear contribution. At last in Section 2.5, this part of the report is summarized.

2.2 Modelling

The material used is an isotactic polypropylene (iPP) homopolymer (Borealis HD601CF, $M_w = 365$ kg/mol, and $M_n = 68$ kg/mol), which is also examined in other studies [17, 24, 25]. The rheological properties of this material are given in Appendix A.1.

2.2.1 Geometry

To model the flow of the iPP in a FiSER, the geometry shown in Figure 2.3 is used. On this geometry the governing equations are solved. Flow is applied in this geometry, by simultaneously moving (in opposite directions) the two pistons at $z = \pm L/2$. It is assumed that the sample is axisymmetric, meaning that only a two dimensional geometry is needed, with a symmetry condition at $r = 0$. In this geometry, boundary Γ_1 is the free surface. The simulations start after the pre-stretch, where the shape of the free surface is either a circle or an ellipse. A circular arc (as shown in Figure 2.3) is only possible if $(R_c - R_0) \leq L_0/2$. Here R_c is the compressed radius of the sample, which is in the simulations always equal to the radius of the piston, R_p. But in the home-build FiSER, it is often the case that the sample is not pre-stretched sufficiently to satisfy this condition.

In this chapter, four different geometries are simulated. The four geometries have a compressed aspect ratio of 0.25, 0.42, 0.5 and 1.0, respectively. An overview of the studied geometries is given in Table 2.1.

Table 2.1: Overview of the geometries studied. The dimensions of the compressed and pre-stretched state are given. Simulations start from the (pre-stretched) initial shape.

N_{geo}	R_c [mm]	L_c [mm]	Λ_c	Compressed shape	R_0 [mm]	L_0 [mm]	Λ_0	ε_{pre}	Initial shape
1	1.5	1.5	1.0		1.0	2.5	2.5	0.8	
2	1.5	0.75	0.5		1.0	1.27	1.27	0.8	
3	1.5	0.63	0.42		1.0	1.13	1.13	0.8	
4	1.5	0.37	0.25		1.0	0.68	0.68	0.8	

Figure 2.2: Polymer sample between two pistons in a filament stretching extensional rheometer (Image reproduced from [26]).
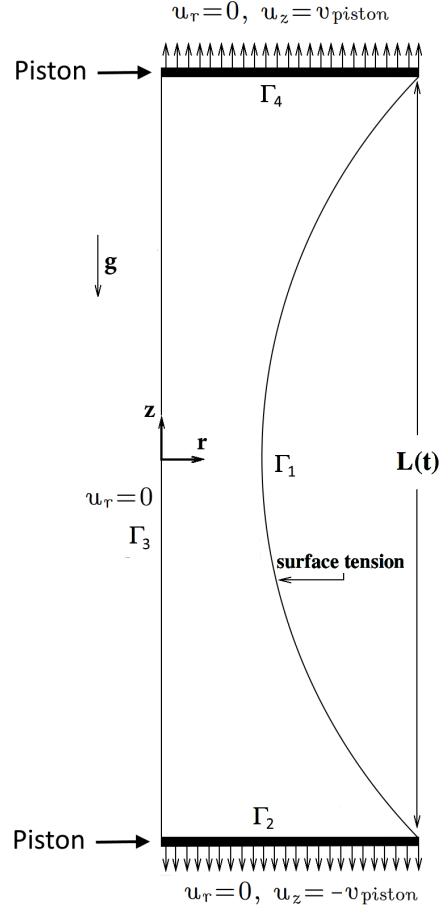

Figure 2.3: Geometry of a sample extended to the length L with a piston velocity of $u_z = \pm v_{\text{piston}}$.

2.2.2 Relevant physical phenomena

To determine whether viscoelasticity, inertia, surface tension and gravity are relevant physical phenomena in this problem, the following dimensionless quantities are studied:

- Deborah number: $\text{De} = \lambda_c \dot{\varepsilon}$, ratio of relaxation time of the material and characteristic time scale of the experiment.
- Reynolds number: $\text{Re} = R_0^2 \dot{\varepsilon} \rho / \eta_0$, ratio of fluid inertial forces and viscous forces.
- Capillary number: $\text{Ca}^{-1} = \hat{\gamma}/(R_0 \dot{\varepsilon} \eta_0)$, ratio of surface or interfacial tension forces to viscous forces.
- Bond number: $\text{Bo} = R_0^2 g \rho / \hat{\gamma}$, ratio of gravitational forces to capillary forces. This number is used as $\text{BoCa}^{-1} = R_0 g \rho / (\dot{\varepsilon} \eta_0)$, which defines the ratio of gravitational body forces to viscous forces.

Here λ_c is the average characteristic relaxation time defined as: $\lambda_c = \sum (\eta_i \lambda_{b,i}) / \eta_0$ and η_0 is the zero-shear viscosity defined as: $\eta_0 = \sum \eta_i$. Using the viscoelastic spectrum, the density and the surface tension, given in Appendix A.1, the dimensionless quantities are calculated for strain rates of 0.01 and 1.0 1/s. These strain rates are chosen, because the in-house developed FiSER is limited to these strain rates for the used iPP [16]. An overview of the dimensionless quantities can be found in Table 2.2. Here, an initial radius of $R_0 = 1$ mm is assumed and $g = 9.81$ ms^{-2}.

Table 2.2: Overview of the dimensionless quantities for iPP at 220 °C.

$\dot{\varepsilon}$	$0.01\ \mathrm{s}^{-1}$	$1.0\ \mathrm{s}^{-1}$
De	0.0063	0.63
Re	$1.2 \cdot 10^{-8}$	$1.2 \cdot 10^{-6}$
Ca^{-1}	1.30	0.013
$BoCa^{-1}$	0.76	0.0076

Once a material has a Deborah number of about one, it behaves as a non-Newtonian fluid. So for strain rates of $1.0\ \mathrm{s}^{-1}$, the non-Newtonian behaviour of iPP should be taken into account. This is done by using the *eXtended Pom-Pom* (XPP) constitutive equation [27] as described in Section 2.2.4. From this table it also follows that the inertial effects are expected to be negligible, since the Reynolds number is very small. Therefore inertia will not be modelled. For small strain rates, the effect of the surface tension and gravity force are not negligible, because the capillary number and $BoCa^{-1}$ are approximately one. This means that the contributions of viscous forces, surface tension and gravity forces are approximately the same. Therefore both gravity and surface tension are included in the model. Surface tension is applied only to the free boundary as shown in Figure 2.3.

2.2.3 Momentum balance

The momentum balance is described as:

$$\rho(p)\frac{D\boldsymbol{u}}{Dt} = -\nabla p + \nabla \cdot \boldsymbol{\tau} + \nabla \cdot (2\eta_s \boldsymbol{D}), \tag{10}$$

where $\boldsymbol{u}$ is the velocity, ρ the density of the material which depends on the pressure, p, according to (15) and $\boldsymbol{D}$ the deformation rate tensor. The extra stress tensor is defined by using the decomposition $\boldsymbol{\sigma} = -p\boldsymbol{I} + \boldsymbol{\tau}$, where $\boldsymbol{I}$ is the unity tensor. A relatively small viscous component η_s Pa s is added for numerical reasons. Since the XPP constitutive equation will be used, the extra stress tensor is given by:

$$\boldsymbol{\tau} = \sum_i g_i(\boldsymbol{c}_i - \boldsymbol{I}). \tag{11}$$

Here, g_i is the modulus of mode i and $\boldsymbol{c}_i$ the conformation tensor of mode i, calculated with the XPP constitutive equation [27] (shown in Section 2.2.4).

The fluid is at rest at the start of the simulation ($t = 0$). On the driving pistons, the velocity is prescribed as:

- $u_r = 0$ on Γ_2 and Γ_4

- $u_z = -v_{\mathrm{piston}}$ on Γ_2

- $u_z = v_{\mathrm{piston}}$ on Γ_4

On the symmetry line, the following applies:

- $u_r = 0$, on Γ_3

The remaining boundary is a free surface:

- $\boldsymbol{u} \cdot \boldsymbol{n} = \boldsymbol{0}$, on Γ_1,

where $\boldsymbol{n}$ is the unit normal vector on the surface S. On this boundary, the surface tension is applied using a Neumann boundary condition

- $(-p\boldsymbol{I} + 2\eta_s \boldsymbol{D} + \boldsymbol{\sigma}) \cdot \boldsymbol{n} = \nabla_s \cdot (\hat{\gamma}(\boldsymbol{I} - \boldsymbol{nn}))$, on Γ_1,

with ∇_s the surface gradient operator. A constant surface tension, $\hat{\gamma}$ is assumed (see Table A.2 in Appendix A.1).

7

2.2.4 Constitutive models

The constitutive model used for predicting the conformation tensor is the multi-mode XPP model [27]. Originally, the XPP model was proposed for branched polymers, but it also captures the physics of linear polymers, as shown by Verbeeten et al. for *high-density polyethylene* (HDPE) [28]. The differential equation of the XPP model is given by:

$$\overset{\triangledown}{\boldsymbol{c}}_i + 2\frac{\exp\left[\nu_i\left(\sqrt{\mathrm{tr}\boldsymbol{c}_i/3}-1\right)\right]}{\lambda_{s,i}}\left(1-\frac{3}{\mathrm{tr}\boldsymbol{c}_i}\right)\boldsymbol{c}_i + \frac{1}{\lambda_{b,i}}\left(\frac{3\boldsymbol{c}_i}{\mathrm{tr}\boldsymbol{c}_i}-\boldsymbol{I}\right) = \boldsymbol{0}, \tag{12}$$

where $\overset{\triangledown}{\boldsymbol{c}}_i$ denotes the upper convected derivative of the conformation tensor of mode i, $\lambda_{b,i}$ denotes the relaxation time for backbone tube orientation of mode i, $\lambda_{s,i}$ denotes the backbone stretch relaxation time of mode i and the parameter ν_i depends on the number of arms of the molecule q_i following $\nu_i = 2/q_i$ [27]. The Giesekus α-parameter is set to 0.

The viscoelastic spectrum of the iPP used in this study is determined by Roozemond et al. [17] and is given in Appendix A.1 in Table A.1. With the implicit and explicit addition of $\boldsymbol{c}/\lambda$, the time step can be larger than the smallest relaxation time. But in some cases (using the viscoelastic spectrum of Roozemond et al. [17]) the flow became unstable for these time steps. Therefore, it is chosen to increase the smallest relaxation times to $2\cdot10^{-4}$ s and take a time step smaller than this value. This slight increase in relaxation times hardly affects the flow for the strain rates used in this study. More information about the time step is given in Section 2.3.2.

Relaxation times shift with temperature according to an Arrhenius type relation, which is given by:

$$a_T = \exp\left[\frac{E_a}{R^*}\left(\frac{1}{T}-\frac{1}{T_{\mathrm{ref}}}\right)\right], \tag{13}$$

with a_T the temperature shift factor, T the absolute temperature, T_{ref} a reference temperature, $R^* = 8.314$ J/(K mol)] the universal gas constant and E_a the activation energy for flows. For iPP the activation energy for flows is $E_a = 40.0$ kJ/mol [17]. The pressure shift factor, a_p, is defined as [29]:

$$a_p = \exp(\kappa(p-p_{\mathrm{ref}})), \tag{14}$$

where κ is the pressure shift constant, p the pressure and p_{ref} the reference pressure of 1 bar. The pressure shift constant for iPP is $\kappa = 16.18$ GPa^{-1} [30].

The compressibility of the materials is taken into account by considering the polymer melt to be an elastic solid in volume [17]:

$$p = p_0 - K\ln J, \tag{15}$$

with p_0 the initial pressure, K the compression modulus and $J = \det\boldsymbol{F}$, where $\boldsymbol{F}$ is the deformation gradient tensor between the reference configuration and the current configuration. The compressibility modulus for iPP is approximately $K \approx 10^9$ [Pa] [17]. The Jacobian J is a measure of the change in volume and the density changes if the volume changes: $\rho = \rho_0/J$. It is expected that compressibility and pressure dependence of the viscosity only slightly affect the flow, since no significant pressure differences are expected during elongation.

2.2.5 Energy balance

To calculate the temperature in the polymer flow, the following energy balance is solved:

$$\rho_k c_{p,k}\frac{DT}{Dt} = \lambda_k\nabla^2 T + \boldsymbol{\tau}:\boldsymbol{D}, \tag{16}$$

where ρ is the density, c_p the heat capacity at constant pressure, T the temperature, λ_k the thermal conductivity coefficient and subscript k denotes the material, which can be either the polymer, air or the steel of the pistons. Values of the parameters of the heat balance equation are given in Table A.2 in Appendix A.1. In this heat balance, heat conduction and stress work are taken into account. The changes of specific heat, thermal diffusivity, and density with temperature are neglected, because the temperature range is limited and these parameters are not so sensitive to temperature.

Isothermal experiments are considered, wherein the temperature is initially constant everywhere: $T(0) = T_0$ for all positions $\boldsymbol{x}$. The temperature of the air remains unaltered. The filament is subjected to heat loss at the free surface due to convection. Therefore, it is assumed that there is convection at the entire boundary Γ_1, according to:

- $-\lambda_p \nabla T \cdot \boldsymbol{n} = h_p(T - T_\infty)$, on Γ_1.

Here, h_p is the convective heat transfer coefficient of the polymer and $T_\infty (= T_0)$ the ambient temperature. To determine h_p, a Nusselt number of $Nu = h_p R_0 / \lambda_p \approx 0.72$ is assumed. This assumption is based on fiber spinning measurements on PE performed by Acierno et al. [31]. They found that very close to the spinneret and in still air the Nusselt number is constant. Using the thermal conductivity coefficient of the polymer in Table A.2 in Appendix A.1 and $R_0 \approx 1$ mm, the used convective heat transfer coefficient in this paper is assumed to be $h_p = 79$ kg K^{-1}s^{-3}.

The temperature at the pistons is assumed to be constant:

- $T = T_0$, on Γ_2 and Γ_4.

2.2.6 Numerical method

The model presented in this paper is solved numerically in two dimensions with an in-house finite element method (FEM) code [19]. The movement of the material is tracked using a moving mesh. The Arbitrary Lagrangian Eulerian (ALE) formulation is used to take this moving mesh into account [32]. The mesh velocity is calculated with a first-order backwards differencing scheme [33]. The governing equations are solved sequentially per time step. For the fist time step, semi-implicit Euler time stepping is employed, which is followed by a second-order semi-implicit Gear time stepping [34]. As the mesh is deformed in time, because both pistons move apart, elements may become too deformed to yield accurate solutions. A new mesh is generated by tracking the deformation of each element and determining the change in area and the change in aspect ratio of these elements. The change in area, f_1^e, and aspect ratio, f_2^e, of each element are defined as [33]:

$$f_1^e = |\log(A^e/A_0^e)| \qquad \& \qquad f_2^e = |\log(S^e/S_0^e)|, \qquad (17)$$

with A^e the element area, A_0^e the element area of the undeformed mesh and $S^e = (L_{\max}^e)^2/A_0^e$ the aspect ratio, where $L_{\max}^e$ is the maximum length of the sides of an element. Remeshing is invoked if either $f_1^e > 0.6$ or $f_2^e > 0.6$, which coincides with a change in area or aspect ratio by a factor 1.8. To solve the governing equations in the following steps after remeshing, the solution $\boldsymbol{u}^n$ is projected on a new mesh. Solutions $\boldsymbol{u}^n$ and $\boldsymbol{u}^{n-1}$ are projected, so that second-order (semi-implicit Gear) time stepping can be used after the projection.

Since Galerkin finite element approximations are used, stabilization techniques are needed. The techniques used in this study are: discrete elastic-viscoelastic stress split (DEVSS-G) [35], streamline-upwind Petrov-Galerking (SUPG) [36], log-conformation representation (LCR) [37], and implicit and explicit addition of $\boldsymbol{c}/\lambda$ [38]. In Appendix A.2, details about mesh and time step independency are provided.

2.3 Methods

To measure correct values for the extensional viscosity in a filament stretching rheometer, several actions have to be performed. Some of these actions have to be modelled in order to measure correct extensional viscosities with the simulations. The following actions are included in the model:

- Methods to measure the force on the pistons;
- A method to measure the radius at the middle of the sample;
- A controller to ensure a constant strain rate at the middle of the sample;
- Correction of the gravity and surface tension contributions;
- Correction of shear effects at the start of the experiments.

2.3.1 Measuring the force on the bottom piston

In a filament stretching rheometer, force measurements are done to be able to calculate the mean stress difference at the middle of the filament. With this stress difference, the extensional viscosity of the material can be calculated. The force is measured with a force transducer positioned at one of the two moving pistons. For the home-build FiSER, the force transducer is positioned at the bottom piston [16]. This means that during the simulations the force is measured at boundary Γ_2. The measurement of the force is done by calculating both the reaction forces and the drag force, which are explained below.

The reaction force (or the internal force) can be found via the residual, once the solution of the problem is known (i.e. the displacement vector). In finite element simulations, the system of equations for solving the displacement vector is usually expressed as:

$$\underline{\underline{K}}\,\underline{d} = \underline{f}, \tag{18}$$

where, $\underline{\underline{K}}$ is the global stiffness matrix, $\underline{d}$ the global displacement vector and $\underline{f}$ the right-hand side vector. To solve this set of equations, the prescribed boundary conditions (i.e. constraint degrees of freedom) are to be substituted in the system matrix. To do so, the system of equations is rewritten to:

$$\begin{bmatrix} \boldsymbol{K}_{uu} & \boldsymbol{K}_{up} \\ \boldsymbol{K}_{pu} & \boldsymbol{K}_{pp} \end{bmatrix} \begin{bmatrix} \boldsymbol{d}_u \\ \boldsymbol{d}_p \end{bmatrix} = \begin{bmatrix} \boldsymbol{f}_u \\ \boldsymbol{f}_p \end{bmatrix}. \tag{19}$$

Here, the subscript u indicating the unknown (unconstrained) part and p the prescribed (constrained) part. Because the prescribed displacements, $\boldsymbol{d}_p$ are known, the system that of equations that have to be solved can be reduced to:

$$\boldsymbol{K}_{uu} \cdot \boldsymbol{d}_u = \boldsymbol{K}_{up} \cdot \boldsymbol{d}_p - \boldsymbol{f}_u \tag{20}$$

With this equation, it is then possible to solve the unknown displacements $\boldsymbol{d}_u$. After solving this equation, the residual forces can be calculated. The residual force of the unknown part, which has no extensional applied loads, should be approximately zero and is given by:

$$\boldsymbol{f}_{r,u} = \boldsymbol{K}_{uu} \cdot \boldsymbol{d}_u + \boldsymbol{K}_{up} \cdot \boldsymbol{d}_p - \boldsymbol{f}_u \approx \boldsymbol{0}, \tag{21}$$

with $\boldsymbol{f}_{r,u}$ the residual of the unknown part. However, the residual forces in the Dirichlet nodes are not zero. The non-zero residual force are called the (prescribed) reaction forces, which can be found from the residual of the essential part:

$$\boldsymbol{F}_{\text{reac}} = \boldsymbol{f}_{r,p} = \boldsymbol{K}_{pu} \cdot \boldsymbol{d}_u + \boldsymbol{K}_{pp} \cdot \boldsymbol{d}_p - \boldsymbol{f}_p \neq \boldsymbol{0}, \tag{22}$$

where $\boldsymbol{F}_{\text{reac}}$ is the reaction force vector and $\boldsymbol{f}_{r,p}$ the residual of the prescribed part. Since the boundary at the piston consists only of Dirichlet nodes, the total reaction force, acting on the plate, can be found by adding the force contributions in the z-direction:

$$F_{\text{piston}} = \sum F_{\text{reac},z}. \tag{23}$$

Here, F_{piston} is the force action on the piston.

The drag force is found by solving the momentum balance on the geometry of the sample. Using conservation of mass, the drag force can be defined as the surface integral over the pressure, viscous stress

and viscoelastic stress. The drag force is always directly opposed to the velocity of the object. So in this case, the drag force is opposed to the velocity vector of the bottom piston, which is the inwards pointing normal vector $\boldsymbol{n}$ of boundary Γ_2 (see Figure 2.4). Then the drag force follows from:

$$F_{\text{drag}} = \left[\int_S (-p\boldsymbol{I} + 2\eta_s \boldsymbol{D} + \boldsymbol{\sigma}) \cdot \boldsymbol{n} \ dS + \boldsymbol{F}_s \right] \cdot \boldsymbol{n} \quad (= F_{\text{piston}}). \tag{24}$$

Here, F_{drag} is the drag force. Since surface tension is applied, an extra force contribution has to be added to the drag force, $\boldsymbol{F}_s$. The angle of the force contribution of the surface tension is the slope of the free surface at the bottom piston (see Figure 2.4).
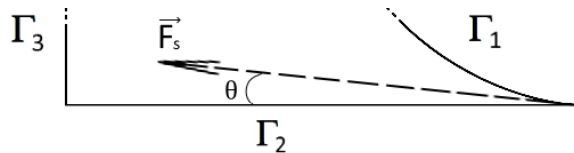
Figure 2.4: Schematic drawing of the force contribution of the surface tension on the bottom boundary of the geometry. The direction of the force is the slope given by the tangent of the free surface, Γ_1, with respect to the bottom piston, Γ_2.

The force is found by projecting the total force on the circumference of the piston and the surface tension:

$$\boldsymbol{F}_s = 2\pi R_{\text{p}} \begin{bmatrix} \cos(\theta) \\ \sin(\theta) \end{bmatrix} \hat{\gamma}, \tag{25}$$

where R_{p} is the radius of the piston, θ the angle between the piston and the free surface at $\boldsymbol{x} = [R_{\text{p}}, L/2]$. The surface tension is a material constant, which is given in Table A.2 in Appendix A.1. The mesh of the geometry consists of second-order elements. Therefore, the slope/angle of the force vector is found via a second-order (BDF2) derivative:

$$\theta = \tan^{-1}\left(\frac{1.5r_1 - 2r_2 + 0.5r_3}{z_1 - z_2} \right), \tag{26}$$

with r_j and z_j the radial and axial position of the j'th node on the interface closest to the piston.

2.3.2   Controller

To perform pure uniaxial extensional experiments with a FiSER, the strain rate at the middle of the fluid sample needs to be constant. Marin et al. developed a controller with both feed-back (PI) and feed-forward actions to control this strain rate [21]. In the proposed scheme, the motion of the pistons is commanded by controlling their velocity via the Hencky strain. In the feed-back loop the strain is corrected by comparing the actual radius with the ideal radius of the middle of the filament, R_{ideal}. To do so, the radius of the middle of the filament is measured with a laser and is used as an input in the next time step. The equation for the controller of the length based Hencky strain is given by:

$$\varepsilon_z(i+1) = \varepsilon_z(i) + K_p[\delta\varepsilon(i) - \delta\varepsilon(i-1)] + K_i\Delta t[\delta\varepsilon(i)] + \Delta\varepsilon_z^{ff}(i), \tag{27}$$

where $\varepsilon(i)$ is the mid-radius based Hencky strain at time step i (or time t), defined as:

$$\varepsilon(t) = -\frac{1}{2}\ln\left(\frac{R(t)}{R_0} \right). \tag{28}$$

In control language, ε_z is the actuated variable and ε the controlled variable. In Equation (27), the error $\delta\varepsilon$ is calculated as follows:

$$\delta\varepsilon = \varepsilon_{\text{ideal}} - \varepsilon_{\text{meas}} = 2\ln\left(\frac{R(i)}{R_{\text{ideal}}(i)}\right) \tag{29}$$

where, R_{ideal} is the ideal radius for pure uniaxial flow. The ideal radius follows from Equation (7) using that $\varepsilon(t) = \dot{\varepsilon}t$. The actual radius of the sample is measured with a laser and is defined as $R\ (= R_{\text{meas}})$. In the home-build FiSER, the time step of the laser is $\Delta t = 200\ \mu s$ and the PI gains are $K_p = 0$ and $K_i = 2.5$ [16]. Also a feed-forward contribution $\Delta\varepsilon_z^{ff}$ is added in the controller of the home-build FiSER. In the simulations this feed-forward contribution is superfluous and therefore set to zero.

With the controlled length based strain (given in Equation (27)), the piston velocity is calculated via Equation (8). In the simulations, this piston velocity is applied as a boundary condition each time step. The time step of the simulations is limited to a maximum of $(\Delta t)_{\text{max}} = 200\ \mu s$, which is the sample rate of the laser of the home-build FiSER. However, the integral gain is increased to a value of $K_i = 400$ in the simulations. In this way, the mid-radius of the sample is almost instantly following the ideal radius of pure uniaxial elongation. Increasing the integral gain even more for this time step, decreases the stability of the simulation and therefore the simulation crashes.

In the simulation, the strain rate is not limited to $\dot{\varepsilon} = 1\ s^{-1}$. To maintain stability of the simulation, the time step has to be decreased when increasing the strain rate. In Figure 2.5, the used time step is plotted as a function of the strain rate. This relation between the time step and strain rate is determined empirically and is tested for strain rates of 0.29, 0.71, 1.71, 4.14 and 10 s^{-1} for temperatures ranging from 110 °to 200 °C. These time steps are not the maximum time steps, but just time steps that seemed to work. For strain rates of $\dot{\varepsilon} > 10$, the correctness of this relation is questionable. Therefore, a strain rate of $\dot{\varepsilon} = 10\ s^{-1}$ is used as the maximum applied strain rate. The relation of the time step shown in Figure 2.5 is given by:

$$\Delta t = \begin{cases} \Delta t_{\text{max}} & \text{for } \dot{\varepsilon} \leq 1\ s^{-1} \\ \Delta t_{\text{max}}/\dot{\varepsilon} & \text{for } 1 < \dot{\varepsilon} \leq 10\ s^{-1}, \end{cases} \tag{30}$$

with $\Delta t_{\text{max}} = 2 \cdot 10^{-4}\ s^{-1}$ the maximum time step.
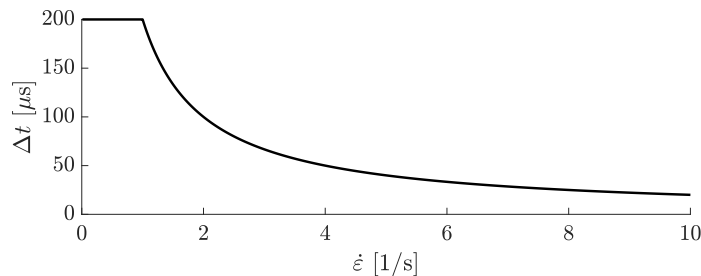

Figure 2.5: Empirically determined relation between the time step and strain rate.

In Equation (27), the term $K_i\Delta t$ is used to correct for the error in the measured radius. For the controller to work properly, this term is kept constant at $K_i\Delta t = 0.08$. Because the times step decreases for increasing strain rates, the integral gain has to be increased. Since the time step is multiplied with the reciprocal of the strain rate, the integral gain has to increase linearly with the strain rate according to:

$$K_i = \begin{cases} 400 & \text{for } \dot{\varepsilon} \leq 1\ s^{-1} \\ 400\dot{\varepsilon} & \text{for } 1 < \dot{\varepsilon} \leq 10\ s^{-1}. \end{cases} \tag{31}$$

This relation is tested up to strain rates of 10 s^{-1}. In Section 2.4.1 it will be shown that the controller works very well for all processing conditions used in this report.

2.3.3 Correction of the gravity and surface tension

In Equation (9), the apparent extensional viscosity function, depending on the measured force, measured radius and strain rate is given. This definition of the transient extensional viscosity does not account for the gravity and surface tension, which contribute to the measured force. To calculate the real transient extensional viscosity, the force balance with both the gravity and surface tension is solved. This results in the following definition for the real transient extensional viscosity [22]:

$$\bar{\eta}_R^+ = \bar{\eta}_a^+ - \frac{\hat{\gamma}/R(t) + \rho g V/(2\pi R^2(t))}{\dot{\varepsilon}} = \frac{F_{\text{piston}}(t)/(\pi R^2(t)) - \hat{\gamma}/R(t) - \rho g V/(2\pi R^2(t))}{\dot{\varepsilon}}, \quad (32)$$

with V the volume of the polymer sample. The subscript a and R are used to distinguish the apparent and real extensional viscosity. In this equation, the effect of inertia is neglected. For polymer melts this inertia term can usually be neglected in the determination of the extensional viscosity [22]. In Section 2.2.1 this is shown for the iPP used in this study, because the Reynolds number is much smaller than one for the flow conditions used in the FiSER.

2.3.4 Shear correction factor

One of the goals of this report is develop a recommendation about correcting for shear contributions in the filament stretching rheometer. In this paper, the shear correction factor is defined as:

$$f_{\text{shear}} = \frac{\bar{\eta}_{\text{XPP}}^+}{\bar{\eta}_R^+}. \quad (33)$$

Here, $\bar{\eta}_{\text{XPP}}^+$ is determined by solving the XPP constitutive equation for a pure uniaxial extensional flow of the multi-mode iPP starting from rest. This definition is different from other work in literature about the shear correction factor. Therein, the pure uniaxial extensional viscosity was calculated using (analytical) solutions of a linear viscous model. Therefore, the present work allows to study the validity of the shear correction factor under non-linear conditions.

In literature, several expressions for the shear correction factor have been derived [23, 26, 39, 40]. The most common one is the theoretical correction derived by Spiegelberg et al. [23]. In this study it is assumed that the fluid sample is very viscous and has an initial aspect ratio smaller than one. Therefore, a lubrication approach is used to describe the initial deformation of the fluid sample. Since this fluid sample is confined between two cylinders, the problem resembles a squeeze flow problem (with reversed direction of motion). Based on this theory, the following expression for the shear correction factor is derived [23]:

$$f_{\text{shear}} = \left[1 + \left(\frac{R(t)}{R_c} \right)^{\frac{14}{3}} / (3\Lambda_c^2) \right]^{-1}, \quad (34)$$

where R_c and Λ_c are the compressed radius and aspect ratio (shown in Figure 2.1). It should be noted, that the period before pre-stretch is not included in this equation. The radius $R(t)$ should be measured after pre-stretch, so that $R(t = 0) = R_0$ is the initial radius after pre-stretch. By using the compressed initial aspect ratio (instead of the pre-stretched aspect ratio, Λ_0), this equation also works for pre-stretched samples.

To simplify the use of this equation with pre-stretched samples, Nielsen et al. [39] have rewritten this equation in terms of strain and pre-strain. The shear correction factor is then given by:

$$f_{\text{shear}} = \left[1 + \frac{\exp(-7(\varepsilon(t) + \varepsilon_{\text{pre}})/3)}{3\Lambda_c^2} \right]^{-1}, \quad (35)$$

with the pre-strain defined as:

$$\varepsilon_{\text{pre}} = 2\ln(R_c/R_0). \quad (36)$$

Here, $t = 0$ is defined after pre-stretch and therefore R_0 is the mid-radius of the polymer sample after

pre-stretch (same definition for $\varepsilon(t)$ and R_0 as in this report). By using the compressed aspect ratio in Equation (34), the expressions of Spiegelberg and Nielsen match.

Rasmussen et al. [40] have tried to improve the theoretical shear correction factor given in Equation (34). They found an empirical function for the shear correction, which ensures less than 3% deviation from there FiSER simulations. A Newtonian sample was used in these simulations and the shear correction factor was determined in the linear regime. No pre-stretching was done, meaning that the simulations start with cylindrical initial geometries. These geometries have an initial aspect ratio range of $\Lambda_0 = 0.2$ to 1.5. The shear correction factor is defined as [40]:

$$f_{\text{shear}} = \left[\left(1 + \left(\frac{R(t)}{R_c} \right)^{\frac{10}{3}} \exp\left(-\Lambda_c^3 \right) \right) / \left(3\Lambda_c^2 \right) \right]^{-1} . \tag{37}$$

Again, the pre-stretch is not included in this equation. The radius $R(t)$ should be measured after pre-stretch, so that $R(t = 0) = R_0$ is the initial radius after pre-stretch. Huang et al. [26] rewrote the expression above in terms of strain and pre-strain. The expression for the shear correction factor is then given by [26]:

$$f_{\text{shear}} = \left[1 + \frac{\exp\left(-5(\varepsilon(t) + \varepsilon_{\text{pre}})/3 - \Lambda_c^3 \right)}{3\Lambda_c^2} \right]^{-1} . \tag{38}$$

All the shear correction factors above do not include the strain rate. This because the theory of Spiegelberg et al. is based on a Newtonian (viscous) fluid, which is strain rate independent. Therefore, these shear correction factors are only valid for strains in the linear viscoelastic region ($\varepsilon < 1.5$) [23].

2.4   Results and discussion

Fist, a validation of the simulations is given. Here, the controlled radius is validated and the simulations are compared with measurements from literature. Subsequently, strain rate distributions over the radius of the sample are shown. Finally, the shear correction factor is discussed, where the effect of aspect ratio and strain rate on the shear correction factor is shown.

2.4.1   Validation

One of the requirements for a pure uniaxial flow is that the mid-radius of the sample decreases exponentially with strain. A mentioned before, a controller is used to ensure this exponential decrease (see Section 2.3.2). In Figure 2.6, the mid-radius of the filament is given as a function of the Hencky strain. Here, the simulated radius immediately (after one time step of $\varepsilon_H = 0.015$) follows the ideal exponential profile. The slopes of the measured and ideal radius are identical. This means that the strain-based controller of the simulations is fast and works properly. In the FiSER experiments, the controller is slower, because a lower value of the integral gain ($K_i = 2.5$) is used.
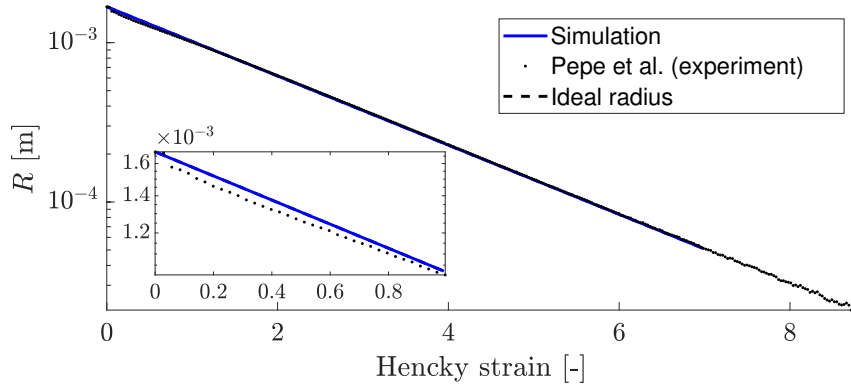
Figure 2.6: Mid-radius measurements with the home-build FiSER at a strain rate of $\dot\varepsilon = 0.71$ s^{-1} and temperature of 150 °C [16]. The sample dimensions are: $R_c = 4$, $L_c = 1.14$, $R_0 = 1.68$ and $L_0 = 3.64$ mm. The solid line represents the simulation of the FiSER with the XPP model and the dashed line is the ideal mid-radius following from Equation (7).

To validate the simulated forces of the FiSER, the force on the bottom piston is compared to the force results in the simulations of Kolte et al. [12]. The force is measured in two ways: via the reaction forces in the nodes and via the drag force on the piston. For a Newtonian fluid, the flow field is solved using the incompressible Navier-Stokes constitutive equations [41] (i.e. Stokes equations). The simulated force on the piston is shown in Figure 2.7. In this figure three curves can be seen: an analytical pure uniaxial solution which follows from the force balance given in Equation (9) with $\eta_e = 3\eta_0$, the simulation results of Kolte et al. [12] and the simulation results of the FiSER model. In case of a Newtonian fluid, the drag force and reaction force match and lay on top of each other. The simulated force matches the analytical pure uniaxial solution for Hencky strains of $\varepsilon_H > 1.5$, whereas for $\varepsilon_H < 1.5$ the force overshoots due to shear effects from the pistons. In this Newtonian simulation at a Hencky strain of 0.1, these shear effects result in an error of approximately 13%.
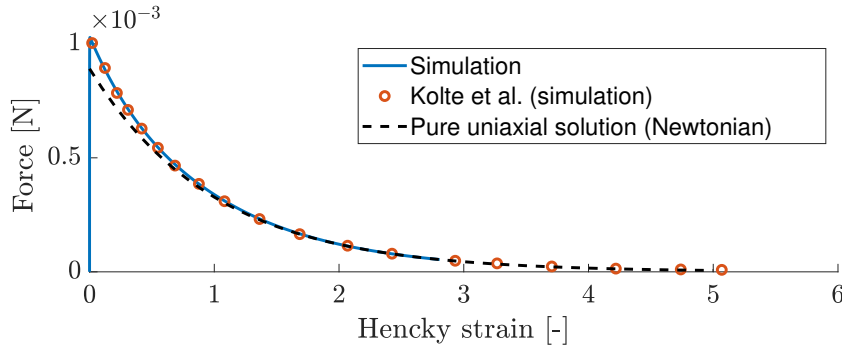
Figure 2.7: Force as a function of the Hencky strain for a Newtonian sample extended with a strain rate of $\dot\varepsilon = 2.0/s$ using the Stokes equations. The used viscosity is $\eta_0 = 21.0$ Pa s and the surface tension is neglected. The dimensions of the initial sample are $L_c = L_0 = 1.5$ mm and $R_c = R_0 = 1.5$ mm.

Subsequently, a viscoelastic multi-mode Oldroyd-B model is implemented in the finite element model. In order to validate the forces found in these simulations, the analytical solution for a pure uniaxial extensional flow of a multi-mode Oldroyd-B model is derived. The expression for the apparent extensional viscosity is given by [12]:

$$\bar\eta^+_{\text{Old-B,a}}(t,\dot\varepsilon) = 3\eta_s + \sum_{i=1}^{N} \eta_i \left(\frac{2}{(1-2\text{De}_i)(1+\text{De}_i)} - \frac{2\exp[-(\frac{1}{\text{De}_i}-2)\dot\varepsilon t]}{1-2\text{De}_i} - \frac{\exp[-(\frac{1}{\text{De}_i}+1)\dot\varepsilon t]}{1+\text{De}_i} \right), \quad (39)$$

with $\mathrm{De}_i = \dot{\varepsilon}\lambda_i$ the Deborah number for the i'th mode and N the number of modes. With this extensional viscosity, the analytical force is found via the force balance given in (9). For the same material, the force is also determined by Kolte et al. [12] and Tirtaadmadja et al. [22]. Kolte et al. [12] determined the force by means of similar simulations as presented in this work. Tirtaadmadja et al. [22] performed controlled FiSER measurements to determine the force. A comparison of all simulated and experimentally determined forces is given in Figure 2.8. Here it can be seen that the simulated force match the simulated force of Kolte et al. [12] and the experimental force determined by Tirtaadmadja et al. [22]. Again at the small Hencky strains, shear affects the simulated and experimental force results and therefore they do not match the analytical pure uniaxial solution. In this viscoelastic simulation at a Hencky strain of 0.1, this shear effects result in an error of approximately 11%, which is slightly lower than the error in the Newtonian simulation. The simulated reaction force and drag force are approximately the same. It is known that the reaction force is slightly more accurate than the drag force, therefore the reaction force will be used throughout the rest of the report.
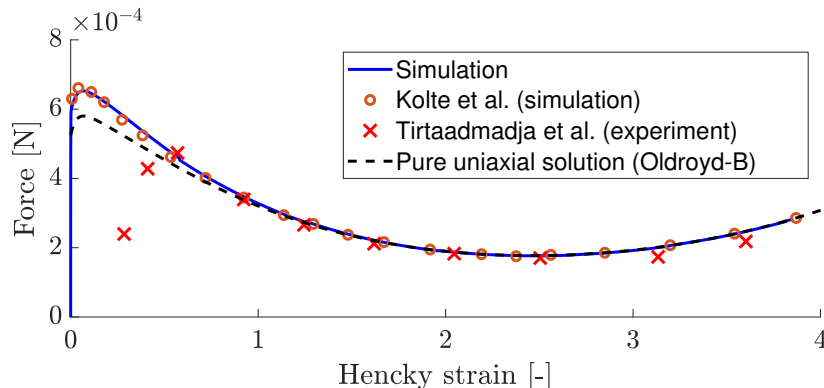
Figure 2.8: Force as a function of the Hencky strain of a sample extended with a strain rate of $\dot{\varepsilon} = 2.0$ s^{-1} using a four mode Oldroyd-B model. The solvent viscosity, polymer viscosities and relaxation times of the PIB used are $\eta_s = 12.4$ Pa s, $\eta_i = [1.69 \ 2.56 \ 2.53 \ 1.85]$ Pa s and $\lambda = [4.20 \ 1.12 \ 0.167 \ 0.0149]$ s. The surface tension is neglected and the sample dimensions are $L_c = L_0 = 1.5$ mm and $R_c = R_0 = 1.5$ mm.

To simulate the flow in the FiSER with the XPP model, the same governing equations as for the Oldroyd-B model are used. Therefore, only the constitutive relation is changed when using the XPP model. In Figure 2.9, the XPP simulations of the used iPP in the FiSER are validated. In this figure, force measurements with the home-developed FiSER at a strain rate of $\dot{\varepsilon} = 0.71$ s^{-1} and a temperature of $T = 150$ °C are shown. These measurements were performed by J. Pepe [16]. The scattering in the data is a result of the limited accuracy of the force transducer. The dimensions of the polymer sample are $R_c = 4$ mm , $L_c = 1.14$ mm, $R_0 = 1.68$ mm and $L_0 = 3.64$ mm.

For the pure uniaxial extensional solution, the real extensional viscosity is calculated with Equation (32). This implies that gravity and surface tension are included. Herein, the apparent extensional viscosity is found by solving the multi-mode XPP model for a pure uniaxial extensional flow. The pure uniaxial extensional viscosity can be compared with the linear viscoelastic envelope (LVE). For the linear viscoelastic envelope, the apparent extensional viscosity is found as follows [42, 43]:

$$\bar{\eta}^+_{\mathrm{LVE,a}}(t) = 3\eta_{\mathrm{LVE}} = 3\left[\eta_s + \sum_{i=1}^{N} \eta_i \left(1 - \exp\left(\frac{-t}{\lambda_{b,i}}\right)\right)\right] \tag{40}$$

with η_{LVE}, the linear viscoelastic viscosity. The subscript a is added to show that this viscosity is not corrected for physical phenomena like surface tension and gravity.

From Figure 2.9 follows that the pure uniaxial solution calculated with the XPP model does not match the linear viscoelastic envelope (LVE). The reason for this is that slightly non-linear behaviour is already

obtained at a strain rate of $\dot{\varepsilon} = 0.71$ s$^-1$. Furthermore, it can be seen that the simulations of the FiSER match with the pure uniaxial solution and the LVE after a strain of approximately $\varepsilon_H > 1.5$. Because an aspect ratio of $\Lambda_c = 0.29$ is used, the simulated force is significantly different from the pure uniaxial force at strains smaller than 1.5 (13% difference at $\varepsilon_H = 0.25$). This difference is defined as the force overshoot, where the ratio of the two is defined as the shear correction factor (see Equation (33)). Though there is lot of scattering on the experimental data, it can be seen that simulation matches the experimental force. Especially at low Hencky strains, where the force is the highest and the scattering is the lowest, good agreement is found between the simulated force and experimental data. A validation of the mesh and time step is given in Appendix A.2.
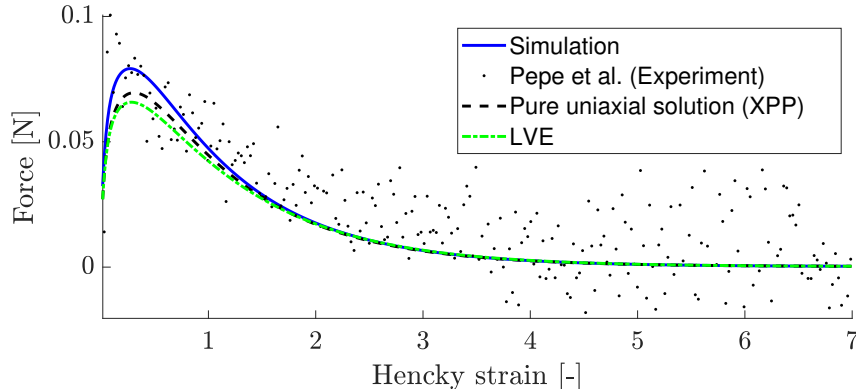
Figure 2.9: Force measurements with the home-build FiSER at a strain rate of $\dot{\varepsilon} = 0.71$ s^{-1} and temperature of 150 °C [16]. The sample dimensions are: $R_c = 4$, $L_c = 1.14$, $R_0 = 1.68$ and $L_0 = 3.64$ mm. The solid line represents the simulation of the FiSER with the XPP model, the dashed line is the pure uniaxial force from the XPP model and the dashed dotted line is the linear viscoelastic envelope in pure uniaxial extension determined with Equation (40).

2.4.2 Strain rate distributions

A constant strain rate at the middle of the sample is required for a pure uniaxial extension. It is mentioned before that at the start of the FiSER experiments, shear contributions affect the flow field. To see how this affects the strain rate, the effective strain rate is calculated. The effective strain rate is defined as:

$$\dot{\varepsilon}_{\text{eff}} = \frac{\dot{\gamma}_{\text{eff}}}{\sqrt{3}} = \sqrt{\frac{2\boldsymbol{D}:\boldsymbol{D}}{3}} \tag{41}$$

where, $\dot{\varepsilon}_{\text{eff}}$ and $\dot{\gamma}_{\text{eff}}$ are the effective strain rate and shear rate, respectively. In case of pure uniaxial elongation, the effective strain rate equals the applied strain rate. For a simulation of the FiSER with a strain rate of $\dot{\varepsilon} = 0.29$ s^{-1}, the effective strain rates are plotted in Figure 2.10.
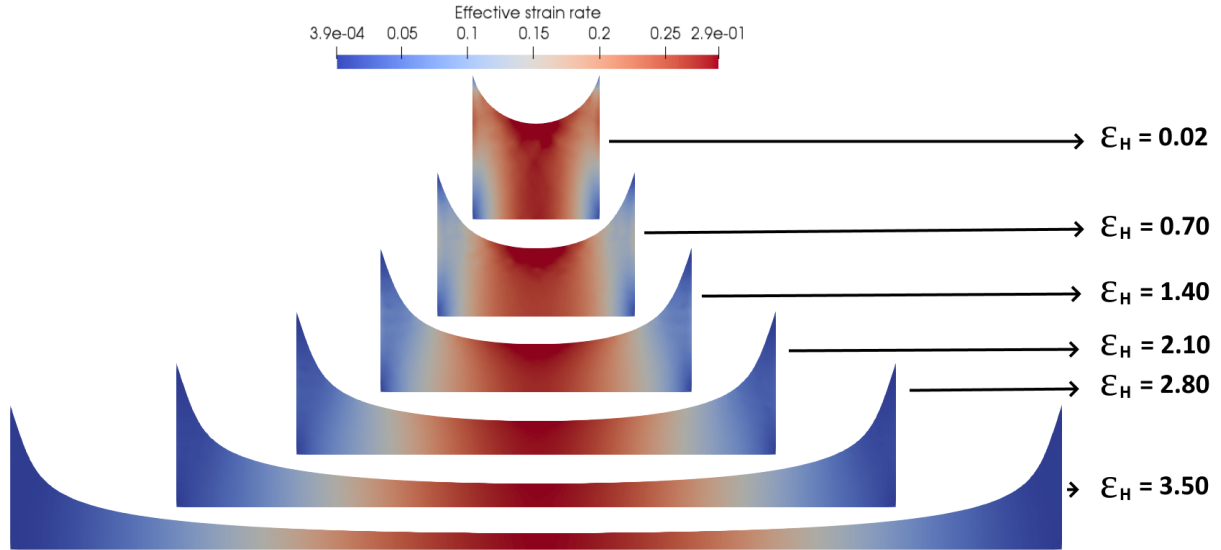
Figure 2.10: Simulation results of the effective strain rate as a function of Hencky strain. The used iPP is extended with a strain rate of $\dot{\varepsilon} = 0.29 \text{ s}^{-1}$ at a temperature of $T = 200$ °C.

In this figure, for low strains ($\varepsilon_H < 2.1$), a strain rate distribution over the middle of the filament ($z = 0$) can be seen. At the free surface ($r = R_0$), the effective shear rate is higher than at the centre of the filament ($r = 0$). To quantify the effective strain rate during elongation, the average effective strain rate on the middle of the filament ($z = 0$) is plotted against the Hencky strain in Figure 2.11.
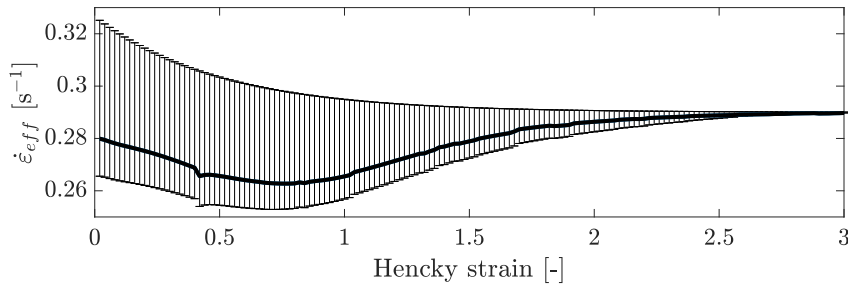
Figure 2.11: Simulation results of the effective strain rate at the middle of the filament as a function of Hencky strain. The error bars show the minimum and maximum effective strain rate over the middle of the filament and the solid line is the effective strain rate averaged over mid-radius of the filament. The used iPP is extended with a strain rate of $\dot{\varepsilon} = 0.29 \text{ s}^{-1}$ at a temperature of $T = 200$ °C.

From this figure it follows that the effective strain rate averaged over the mid-radius of the sample converges to the applied strain rate of $\dot{\varepsilon} = 0.29 \text{ s}^{-1}$. Also the maximum and minimum effective strain rate converge to the applied strain rate. Because the mid-radius is decreasing exponentially, the deviation from the applied strain rate is a result of the the shear effects (i.e. radial pressure drop) induced by the pistons. Note that this averaged effective strain rate is only used to visualize the convergence to the applied strain rate. The value namely depends on the homogeneity of the mesh.

In Figure 2.12, the distribution over the radius at a Hencky strain of $\varepsilon_H = 0.6$ is shown. Here again, it can be seen that the strain rate is not constant, but has a gradient over the radius. These gradients in strain rate affect the measured force, resulting in an incorrect (non-uniaxial) extensional viscosity. Therefore, a shear correction factor is introduced by Speigelberg et al. [23] as mentioned before.
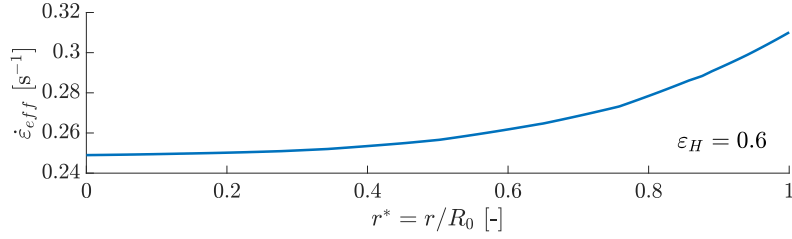
Figure 2.12: Simulation results of the effective strain rate as a function of the dimensionless radius at the middle of the filament for a Hencky strain of $\varepsilon_H = 0.6$. The used iPP is extended with a strain rate of $\dot{\varepsilon} = 0.29$ s^{-1} at a temperature of $T = 200$ °C.

2.4.3 Shear correction factor

In order to give recommendations about measuring with the FiSER, the shear correction factor for multiple geometries is investigated. The geometries used here are given in Table 2.1 and have a compressed aspect ratio of 1.0, 0.5, 0.42 and 0.25, respectively. The effect of these aspect ratios on the shear correction factor is shown in Figure 2.13. In this figure it can be seen that the shear correction factor increases with an increasing aspect ratio. This corresponds with the theory of Spiegelberg, where it is stated that a larger correction for shear contributions is needed for small aspect ratios [23].
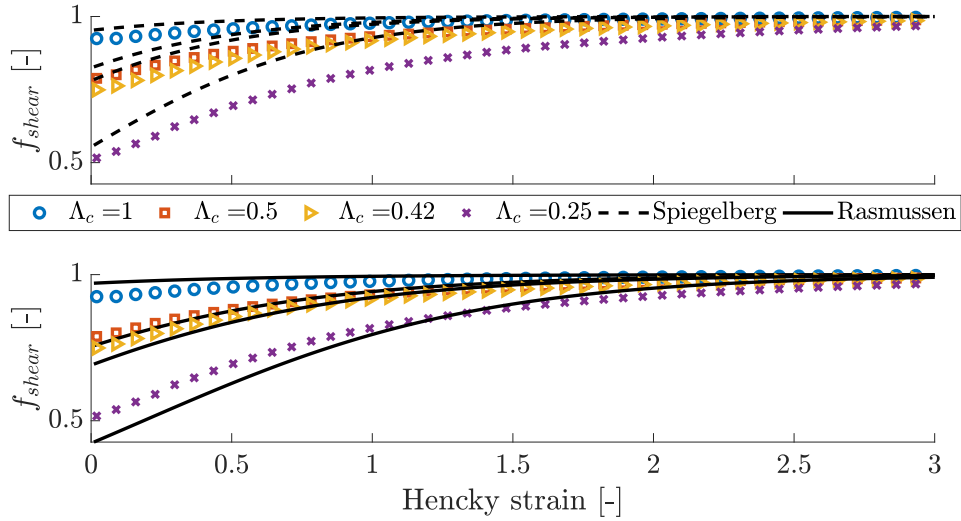
Figure 2.13: Simulated shear correction factor compared with the correction factors found in literature for different aspect ratios. The top figure shows the simulation results compared to the theoretical relation of Spiegelberg et al. given in Equation (34). The bottom figure shows the simulation results compared to the empirical relation of Rasmussen et al. given in Equation (37). The iPP is extended with a strain rate of $\dot{\varepsilon} = 10$ s^{-1} at a temperature of $T = 160$ °C.

To evaluate the models given in literature, Equation (34) and (37) are calculated for the given aspect ratios. From Figure 2.13 follows that the empirical relation of Rasmussen et al. [40] is better in predicting the shear correction factor than the model of Spiegelberg et al. [23]. Nevertheless, the error of this empirical relation is bigger than the claimed 3% (see Section 2.3.4). These shear correction factors from literature are based on a viscous (linear) Newtonian material. But the iPP used in this study is non-linear viscoelastic and therefore the definition of the shear correction factor was changed to Equation (33). To define a more accurate shear correction factor based on the simulated (non-linear) shear correction factor

in Figure 2.13, an improved empirical relation is proposed. This equation is found by fitting the simulated shear correction factors given in Figure 2.13 with the following function:

$$f_{\text{shear}} = \left[1 + \frac{\exp(-a(\varepsilon(t) + \varepsilon_{\text{pre}})/3 - b)}{3\Lambda_c^2}\right]^{-1},\tag{42}$$

with a and b the fitting parameters. For the four compressed aspect ratios, a turns out to be approximately 4, while b decreased with increasing aspect ratio. To fit b per aspect ratio, a function needs to be used that starts at one and decreases to zero for infinite aspect ratios. Therefore, the following exponential function is used to fit b:

$$b = \exp(-\Lambda_c/c),\tag{43}$$

Good agreement with b per aspect ratio is found for $c = 1$. Combining Equation (42) and (43) with $a = 4$ and $c = 1$ results in the proposal of the following non-linear shear correction factor:

$$f_{\text{shear}} = \left[1 + \frac{\exp(-4(\varepsilon(t) + \varepsilon_{\text{pre}})/3 - \exp(-\Lambda_c))}{3\Lambda_c^2}\right]^{-1}.\tag{44}$$

In Figure 2.14, this proposed shear correction factor is compared with the simulated shear correction factors. It can be seen that the error of the improved shear correction factor relation is within 3% for all aspect ratios.
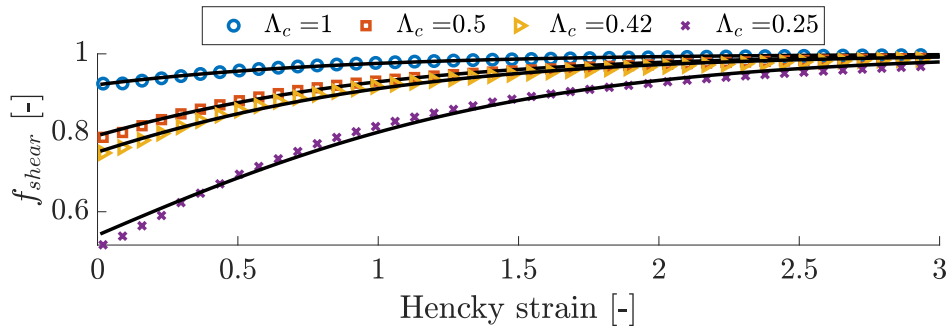
Figure 2.14: Simulated shear correction factor compared with the new relation for the correction factors given in Equation (44) for different aspect ratios. The iPP (characterized by Grosso et al. [20]) is extended with a strain rate of $\dot{\varepsilon} = 10$ s^{-1} at a temperature of $T = 160$ °C.

From Figure 2.9 it follows that already at small strains, the non-linearity of the iPP affects the extensional viscosity, since the linear viscoelastic envelope does not match the pure uniaxial force of the (non-linear) XPP model. This indicates that non-linear effects play a role at small strains. These non-linear effects might affect the shear correction factor, since the flow of non-linear viscoelastic materials is affected by the applied strain rate. Therefore, the effect of strain rate on the shear correction factor is studied. For the used iPP, four strain rates are simulated: 0.71, 1.71, 4.14 and 10.0 s^{-1} with a compressed aspect ratio of $\Lambda_c = 0.5$ and $\Lambda_c = 1.0$. The results are shown in Figure 2.15. At an aspect ratio of $\Lambda_c = 0.5$, the strain rate slightly ($\approx 2\%$) affects the shear correction factors at small strains ($\varepsilon_H < 3.0$). For an aspect ratio of $\Lambda_c = 1$, this effect is even smaller ($< 1\%$).
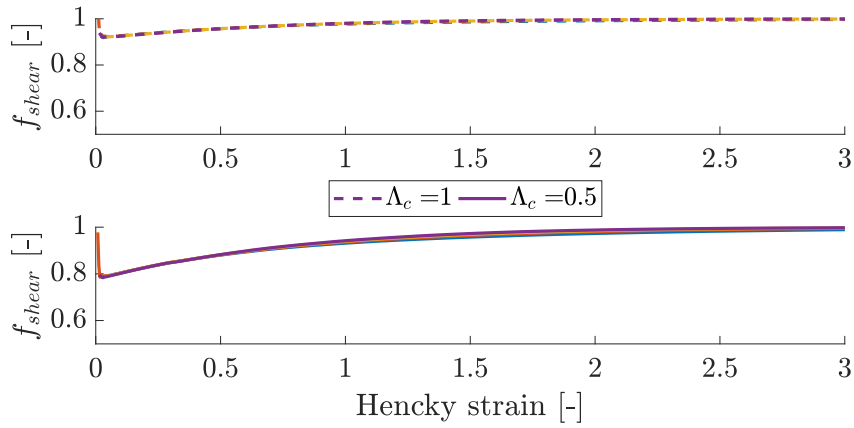
Figure 2.15: Simulated shear correction factors for the iPP of Grosso et al. [20] at strain rates of $\dot{\varepsilon} = 0.71$, $\dot{\varepsilon} = 1.71$, $\dot{\varepsilon} = 4.14$ and $\dot{\varepsilon} = 10.0$ s^{-1}. In the upper figure a aspect ratio of $\Lambda_c = 1.0$ is used and in the bottom figure $\Lambda_c = 0.5$ (for $T = 160$ °C).

According to the correspondence principle of linear viscoelasticity, the same correction factor should be measured for all types of fluids. To test whether this statement holds for the newly developed shear correction factor, the shear correction factor is determined for the iPP characterized by Roozemond (see Appendix A.1) and a *linear low-density polyethylene* (LLDPE). This LLDPE is characterized by Van Drongelen et al. [44]. For both these materials and the iPP characterized by Grosso et al. [20], the extensional viscosity as a function of the strain rate is given in Figure 2.16. The shear rate as a function of the shear rate is given in Figure 2.17.
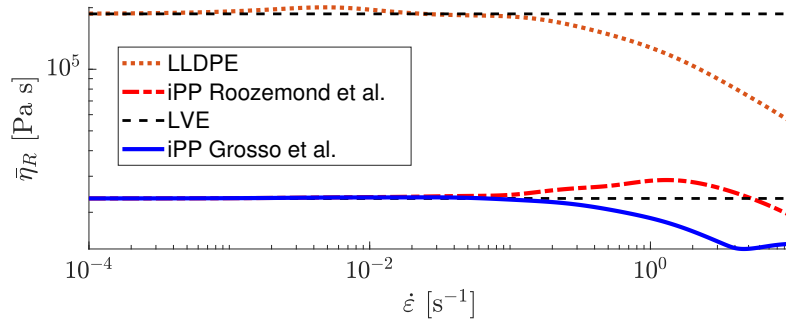
Figure 2.16: Extensional viscosity as a function of the strain rate given by the XPP model. Three differently characterized materials are used: the iPP of Roozemond et al. [17], the iPP of Grosso et al. [20] and the LLDPE of Van Drongelen et al. [44] ($T = 160$ °C).
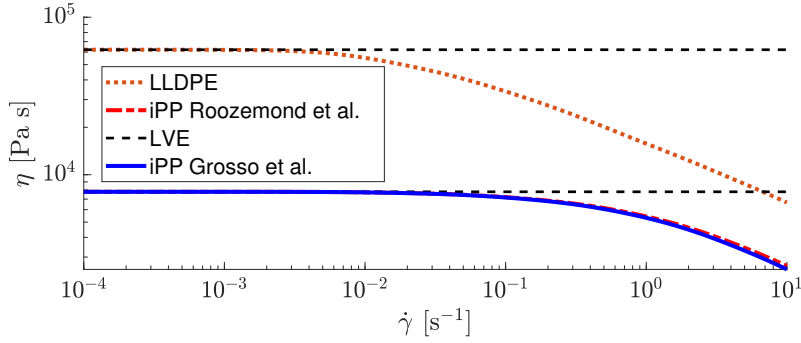
Figure 2.17: Shear viscosity as a function of the shear rate given by the XPP model. Three differently characterized materials are used: the iPP of Roozemond et al. [17], the iPP of Grosso et al. [20] and the LLDPE of Van Drongelen et al. [44] ($T = 160$ °C).

From these two figures can be concluded that the non-linear behavior is completely different for this set of materials. For the LLDPE, the highest degree of non-linear behaviour in extension is observed at a strain rate of $\dot{\varepsilon} = 10$ s^{-1}. In Figure 2.18, the non-linear extensional viscosity of this LLDPE is shown. The simulation is performed at a strain rate of $\dot{\varepsilon} = 10$ s^{-1}, a temperature of $T = 160$ °C and a compressed aspect ratio of $\Lambda_c = 0.42$ (geometry 3). Because of the non-linear XPP model, the pure uniaxial solution starts deviating from the linear viscoelastic envelop already at very small Hencky strains. At large strains ($\varepsilon_H > 2.1$), the simulations converge towards the pure uniaxial solution.
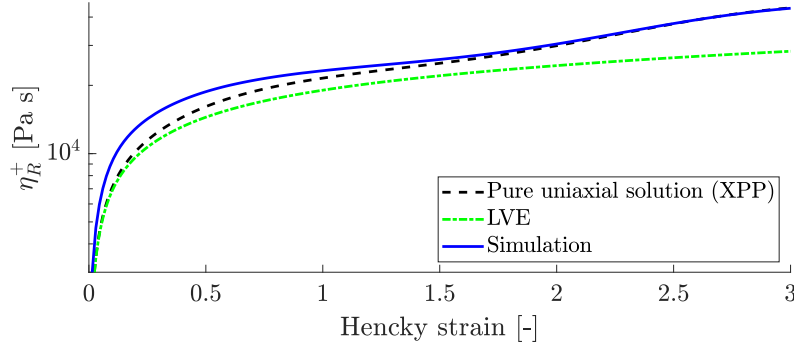

Figure 2.18: Extensional viscosity of a LLDPE sample at a strain rate of $\dot{\varepsilon} = 10$ s^{-1} and a temperature of $T = 160$ °C. Geometry 3 is used with a compressed aspect ratio of $\Lambda_c = 0.42$. The numerical simulations are preformed with the XPP model. The pure uniaxial solution is found with the XPP model.

The shear correction factors of the iPP characterized by Roozemond et al. [17] and the LLDPE are shown in Figure 2.19. From this figure it follows that the materials approximately have the same correction factor. This means that although the materials have completely different non-linear behavior, the shear correction factors match. This supports the newly developed shear correction factor in Equation (44), which is material independent and independent of the strain rate. Also, this implies that the correspondence principle of linear viscoelasticity holds within the range of non-linear conditions considered here. A possible explanation can be that the shear correction factor in Equation 33 includes a non-linear pure uniaxial solution $\bar{\eta}_{\mathrm{XPP}}^+$. Therefore, the simulated non-linear behavior is divided out of the shear correction factor, so that only the effect of the shear contributions on the extensional viscosity is left.
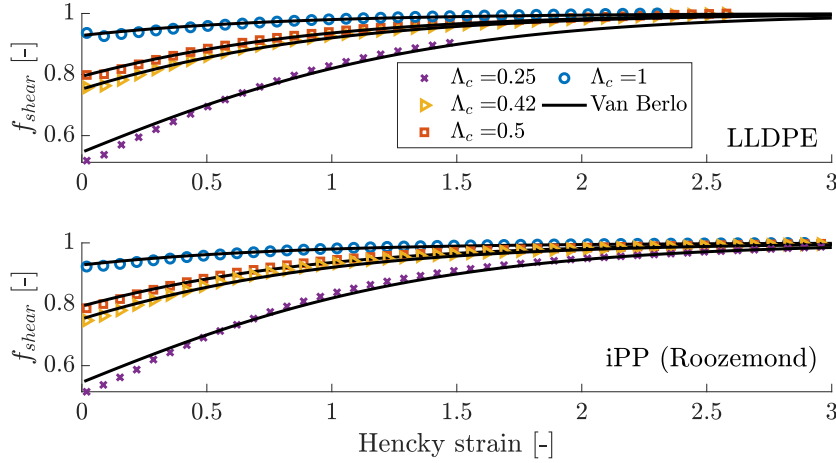
Figure 2.19: Simulated shear correction factors for iPP (Roozemond) and LLDPE compared to the newly developed shear correction factor given in Equation (44). The filaments are extended with a strain rate of $\dot{\varepsilon} = 10$ s^{-1} at a temperature of $T = 160$ °C.

To investigate the shear correction factors of each material more thoroughly, the effective strain rate distributions are compared in Figure 2.20. For the distributions, the geometry with a compressed aspect ratio of $\Lambda_c = 0.42$ is used, which is extended at a strain rate of 10 s^{-1}. The distributions are plotted at a Hencky strain of 0.25, where there are significant shear contributions (see Figure 2.19). From Figure 2.20 it follows that the distributions are approximately the same. This implies that although the rheological and non-linear behaviour of the materials is different, the flow at the middle of the filament is the same. Besides, the diameter at the middle of the sample is the same for the three materials due to the controller. At small strains ($\varepsilon_H < 0.7$), the shape of the free surface of the samples match. But for Hencky strains bigger than 0.7, the controller changes the velocity of the pistons to control the mid-radius. Therefore, the length of the samples and their free surfaces are different. Nevertheless, the mid-radius is not changed and the strain rate distributions are still approximately the same.
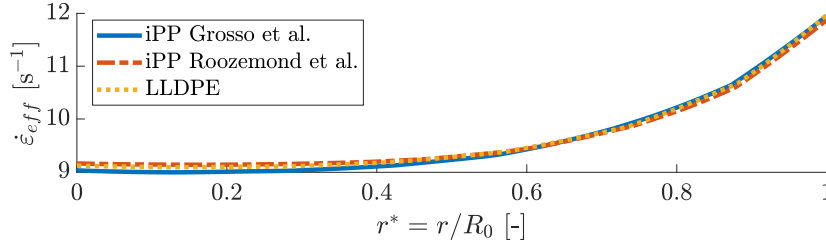

Figure 2.20: Effective strain rate distributions for the iPP characterized by Grosso et al. [20] and Roozemond et al. [17] and the LLDPE at a Hencky strain of $\varepsilon_H = 0.25$. The filaments have a compressed aspect ratio of $\Lambda_c = 0.42$ and are extended with a strain rate of $\dot{\varepsilon} = 10$ s^{-1} at $T = 160$ °C.

All in all it is concluded that for the used non-linear materials at strain rates up to 10 s^{-1}, the simulated shear correction factors match. This conclusion supports the derived empirical shear correction factor in Equation (44), because this relation is material and strain rate independent. Therefore, it is possible to use this relation in a wide range of FiSER experiments.

2.5   Summary

In this work, the shear contributions in a filament stretching extensional rheometer are investigated. To do so, finite element simulations are developed, which can simulate the extension of an iPP polymer at different temperatures, strain rates and initial aspect ratios (geometries). The used constitutive model is the extended pom-pom model, which is a non-linear viscoelastic model. In literature, these shear contributions are quantified with the shear correction factor. Two relations for the shear correction factor are available in literature, which are both based on Newtonian (linear) fluids. Since a non-linear constitutive model is used, a new correlation for the shear correction factor is proposed in this work.

To test the validity of the simulations, the simulated force is compared with measurements with an in-house developed FiSER. The mid-radius of the sample is controlled and it is shown that this radius follows the desired exponential decrease as in the FiSER measurements. Because the shear correction factors from literature are based on Newtonian materials, their correctness is re-examined. To do so, multiple geometries are simulated with different aspect ratios. It is found that these relations from literature can approximate the simulated (non-linear) shear correction factor. Nevertheless, the error of the relations from literature compared to the simulated shear correction factors can be more than 10 %. Therefore, a new relation for the shear correction is derived. The error of this shear correction factor is significantly lower ($< 3\%$). Also it is shown that the shear correction factor is material and strain rate independent for a wide range of parameter values, making it a useful tool in FiSER experiments.

A Appendix

A.1 Material characterization

The meaning of the different parameters in the tables below can be found in the List of symbols.

Table A.1: Viscoelastic model parameters of the XPP model for iPP at reference temperatures of $T = 220\,°C$. Columns 4 and 5 give the spectra used by Roozemond et al. [45], while columns 6 and 7 provide the values derived by using molecular considerations by Grosso et al. [20]. The latter values derived by using molecular considerations are used in this report.

N	η_i [Pa s]	$\lambda_{b,i}$ [s]	$\lambda_{s,i}$ [s] extens.	ν_i [-] extens.	$\lambda_{s,i}$ [s] molec.	ν_i [-] molec.
1	30.00	$5\cdot10^{-5}$	$2\cdot10^{-5}$	2	$6.00\cdot10^{-6}$	0.05
2	130.76	0.0014	$4\cdot10^{-4}$	2	$6.67\cdot10^{-6}$	0.05
3	303.60	0.011	0.0027	2	$5.24\cdot10^{-5}$	0.05
4	480.00	0.060	0.015	2	$2.86\cdot10^{-4}$	0.05
5	377.00	0.29	0.073	2	0.0014	0.05
6	183.70	1.67	0.42	0.25	0.0080	0.05
7	46.00	11.5	2.21	0.17	0.055	0.017

Table A.2: Parameters for the heat balance and the surface tension.

Material	ρ [kg/m³]	c_p [J/(kg K)]	λ [W/(m K)]	χ_∞ [-]	ΔH [J/g]	$\hat{\gamma}$ [mN/m]
iPP [17]	800	3157	0.11	0.650	207	30.2
LLDPE [44]	760	3000	0.23	0.457	279 [46]	28.8
steel [17]	8000	670	80	x	x	x
glass [44]	2500	0.5	1.05	x	x	x

A.2 Mesh and time step convergence

To study the mesh convergence of the system, simulations are performed on five different meshes given in Table A.3. Here, $n_{\mathrm{ini}} = R_p/h_{\mathrm{ini}}$ is the number of elements at the piston boundaries, with h_{ini} the initial element size. At the start of the experiment, the initial element size is used in the entire domain.

For the convergence study, remeshing is included. During remeshing, the mesh at the middle of the filament is refined, such that at every remeshing step $h_{\mathrm{mid}} \leq R/n_{\mathrm{mid}}$. At the pistons, the same element size is used as initially defined.

Table A.3: Mesh resolution of different surface meshes in the convergence study. The star symbol: * indicates that this is the reference mesh.

Mesh	n_{ini}	h_{ini} [mm]	n_{mid}
M1	2	2.0	5
M1	4	1.0	5
M3	6	0.67	5
M4	10	0.4	5
M5*	18	0.22	5

Simulations up to a strain of $\varepsilon_H = 1.5$ are performed, with a time step of $\Delta t = 10^{-5}$ s, a strain rate of $\dot{\varepsilon} = 10\ \mathrm{s}^{-1}$ and an initial temperature of $T_0 = 200\,°C$. The sample dimensions are: $R_p = 4$, $R_0 = 3$ and $L_0 = 6$ mm. At a strain of $\varepsilon_H > 1.5$, the simulated force is close to the theoretical (pure uniaxial) force [23]. Therefore, it is chosen only to simulate up to a strain of 1.5. In Figure A.1, the simulated forces are shown for the different meshes. At a strain of 1.5, the simulated force of the reference solution is close

to the pure uniaxial force determined with the XPP model (as expected). Also a convergence of these forces can be seen at the maximum force ($\varepsilon_h = 0.37$).
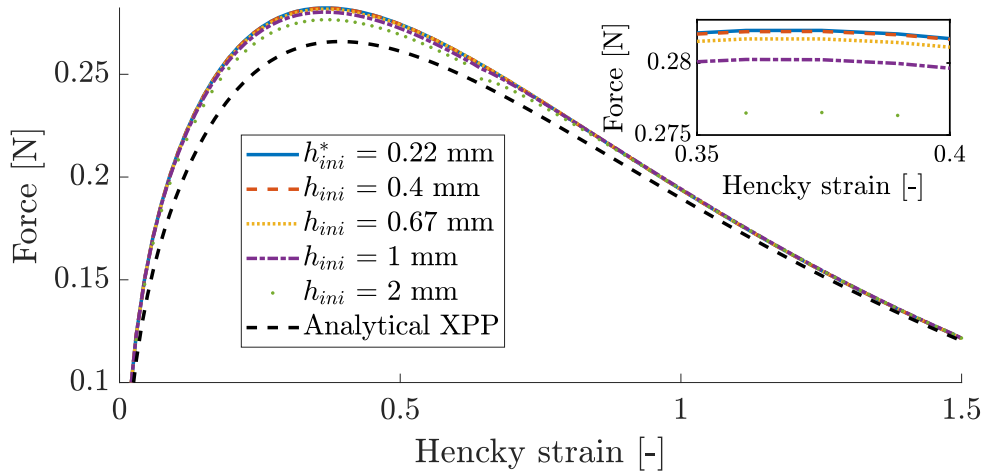

Figure A.1: Simulated forces and the pure uniaxial solution calculated with the XPP model. The reference force curve has an initial element size of $h^*_{\text{ini}} = 0.22$ mm.

In order to investigate this convergence in a more quantitative manner, the following error is defined:

$$\epsilon_F(\varepsilon_H) = \frac{|F(\varepsilon_H) - F^*(\varepsilon_H)|}{F^*(\varepsilon_H)}, \tag{45}$$

with F the simulated force, F^* the simulated force for the reference mesh M5* as indicated in Table A.3. The error is calculated for the different meshes at a strain of $\varepsilon = 0.37$ and $\varepsilon = 1.5$, as shown in Figure A.2. The convergence at a strain of 0.37 seems to be cubic. This rate of convergence is expected based on the order of interpolation of the elements (quadratic elements). For a strain of 1.5, the convergence seems to be quadratic. This is lower than the expected convergence. One of the possible reasons is that remeshing changes the convergence rate. Also other numerical errors can affect the convergence rate. In this work, the M4 mesh is used to simulate the flow in the FiSER. The error of this mesh is smaller than 10^{-4} at a strain of 1.5 compared to the reference mesh.
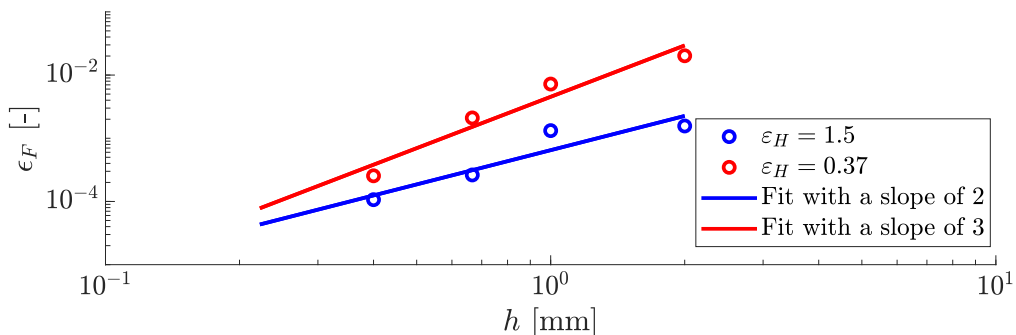

Figure A.2: Mesh convergence at a strain of 0.37 and 1.5. For these simulations, a time step of $\Delta t = 10^{-5}$ s, a strain rate of $\dot{\varepsilon} = 10 \text{ s}^{-1}$ and an initial temperature of $T_0 = 200$ °C are used.

A suitable time step has to be chosen for the simulations. Therefore, a time dependency study is performed on the M4 mesh. The same conditions are used as for the mesh dependency study. There is a limit on

how large the time step size can be, because of the controller ($\Delta t_{\mathrm{max}} = 2 \cdot 10^{-4}$). Besides at higher strain rates, the time step is linearly decreased to maintain stability of the simulation (see Section 2.3.2).

The time dependency is studied in a quantitative manner by using Equation (45). The reference time step is taken as $\Delta t_1^* = 1 \cdot 10^{-7}$. At the used strain rate of $\dot{\varepsilon} = 10$ s^{-1}, the smallest time step possible is $\Delta t_5 = 1 \cdot 10^{-5}$. In Figure A.3, the result of the convergence of the time step is shown. For both strains, the convergence seems to be linear. This figure also shows that the errors are quite small compared to the error in the mesh convergence, indicating that it is only important that the time step is smaller than the time step limit due to the controller. The convergence rate is lower than the expected one, since a second-order time stepping scheme is used. This is possibly caused by the remeshing, because the remeshing causes small numerical errors.
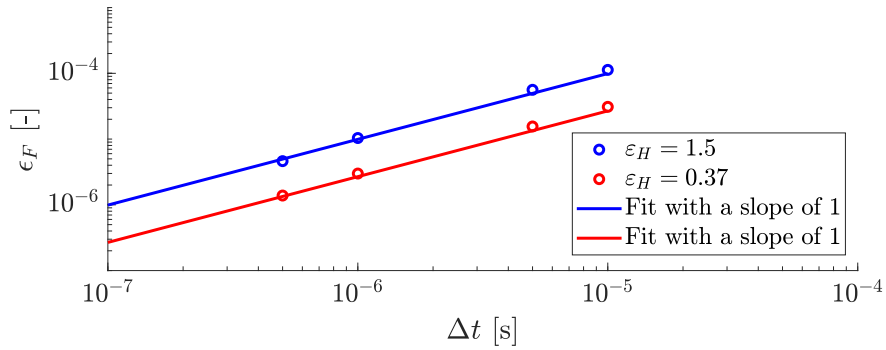

Figure A.3: Time step convergence at a strain of 0.37 and 1.5. For these simulations a M4 mesh is used with a strain rate of $\dot{\varepsilon} = 10$ s^{-1} and an initial temperature of $T_0 = 200$ °C.

3 Modelling crystallization in a filament extensional stretching rheometer

3.1 Introduction

Semi-crystalline polymers, like polyethylene (PE) and isotactic polypropylene (iPP), are most often processed in the molten state and therefore subjected to (strong) flows when shaped into the final product. It is well-known that these flows can accelerate crystallization kinetics and can drastically change the crystalline morphology from spherulites to highly oriented shish-kebab crystals [17]. These morphological changes are important, because they determine the final properties of polymer products. Therefore, a full understanding of the relation between flow, crystallization kinetics, and the resulting morphology is needed to properly design these products. In this work, the flow in a filament stretching rheometer is simulated to examine the relation between extensional flow and crystallization kinetics. For comparison, a FiSER is developed within our group, that can capture flow-induced crystallization by means of in-situ X-ray measurements [16].

3.1.1 Background

When a polymer is cooled from the melt without any disturbance, i.e. in quiescent conditions, nucleation sites appear below the melting temperature. From these nuclei, crystal lamellae grow radially outwards and from spherulites (see Figure 3.1). During the growth process, the stacked lamellae spread apart continuously and branch occasionally. The continuous growth of the primary lamellae forms a spherical skeleton, and the secondary lamellae fill up the space between the primary lamellae. During polymer processing such as fiber spinning, injection molding, and film blowing, polymers flow under high shear and extensional stresses. These stresses result in so called flow-induced crystallization. The flow-induced crystallization process enhances crystallization kinetics and induces new crystal forms and the formation of oriented crystalline structures. Strong flow is able to significantly stretch polymer chains to form shish-kebab structures [47]. In Figure 3.1 a schematic representation is given of the different morphologies generated during flow.
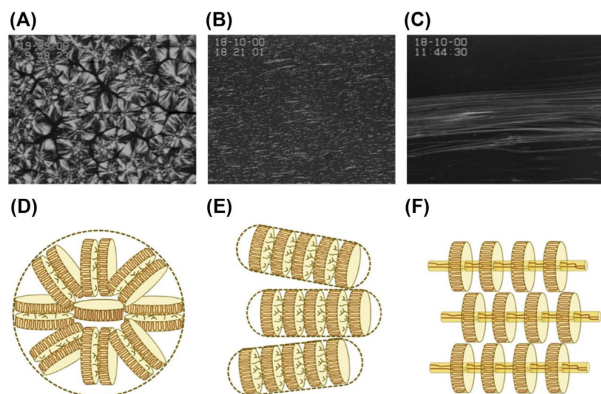

Figure 3.1: Typical morphologies of flow-induced crystallization with (A) no flow, (B) weak flow, and (C) strong flow. The difference in crystalline structures is illustrated in (D-F) (Image reproduced from [48]).
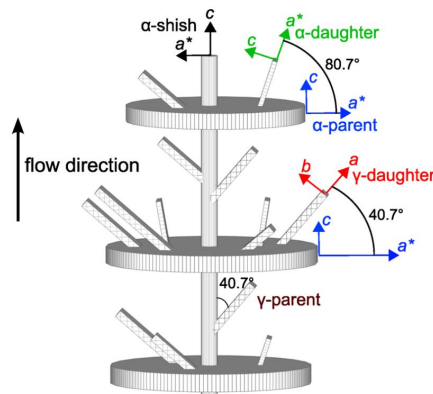

Figure 3.2: Schematic of the morphology of shish-kebab structure of iPP containing α- and γ-"parents" and α- and γ-"daughters" lamellae (Image reproduced from [47]).

Some polymers exhibit polymorphism, i.e. the ability to exist in more than one crystal form. Focusing on iPP, three different crystal forms (α-phase, β-phase, and γ-phase) and a mesophase are found. Under quiescent conditions, iPP crystallizes in the α-monoclinic form by isothermal crystallization. This phase is the most stable. The β-hexagonal and γ-triclinic phases may be crystallized from the melt under

high undercooling or high pressure conditions, or by the addition of nucleating agents. There is also a mesophase in iPP, which is an ordered structure between that of the amorphous and crystalline phases. This phase is for example seen when iPP is quenched from the melt to below 0 °C at a rate faster than 80 °C/s [49].

In injection-molding of iPP, where a distinctive skin-core structure is observed, all these phases can be found. From the wall to the center, this structure consists of a quenched layer due to rapid cooling at the mold wall, a highly anisotropic shear-layer containing shish-kebab structures, a fine-grained layer with low crystal orientation and high nucleation density, and an isotropic core crystallizing at elevated pressures [47]. Due to high cooling rates in the quenched layer, it mainly consists of mesophase. Furthermore, α- and γ-phase are present in the shear layer and the isotropic core, because of high molecular orientation due to flow and elevated pressure. In this region, the polymer is highly oriented and therefore shish-kebab crystals can form. In Figure 3.2 a shish-kebab structure is shown with the different α- and γ-phases growing on it. From the shish lateral surface, α-parents kebabs can grow. On these kebabs, α- and γ-daughters lamellae can nucleate and grow.

3.1.2 Scope and outline

In our group, a modeling framework is developed to describe the crystallization of isotactic polypropylene including all mentioned morphologies and polymorphism [17]. The main goal of this chapter is to expand the finite element model of the FiSER used in Chapter 2, by including the crystallization model of Roozemond et al. [17], so that extensional flow-induced crystallization of iPP can be simulated. This finite element model then includes both rheology and crystallization of iPP. The complete model is elaborated in Section 3.2.

When the model is fully implemented, the effect of the extensional flow on crystallization in the FiSER is investigated. With these simulations, the goal is to give advise about improving the quality of the experimental FiSER measurements. To investigate the effect of extensional flow-induced crystallization, multiple processing conditions are simulated. To measure this crystallization, numerical methods are developed, which are described in Section 3.3. To adjust the processing conditions, different strain rates and temperatures are simulated. In Section 3.4, the results of these simulations are given. Here, a study on the critical crystallization strain is performed. This strain definition was found by White et al [15]. They show that the strain at which crystallisation of IPP starts is constant with a range of strain rates ($\varepsilon_c = 5.8$ for $0.01 < \dot{\varepsilon} < 0.15$ s^{-1}) . In Section 3.4, the validity of this conclusion will be checked by performing simulations with a wide range of strain rates (up to 10 s^{-1}).

Moreover, Wingstrand et al. [50] have shown that the force overshoot due to shear not only affects the extensional viscosity, but also affects crystallization in FiSER measurements. The force overshoot observed in uniaxial extension was reflected in the final morphology of the samples. Since the shear contributions are reduced by increasing the aspect ratio, also the relation between aspect ratio and crystallization is examined in Section 3.4. Finally, the main findings of this chapter are summarized in Section 3.5.

3.2 Modelling

As mentioned in Section 3.1.2, recently Roozemond et al. [17] presented a theoretical model which captures both rheology and crystallization of iPP. This numerical model consists of the rheological model given in Section 2.2 and a crystallization model. The crystallization model can be divided into four model parts: a heat balance, a quiescent crystallization model, a flow-induced crystallization model and a model that describes the crystallization effects on the rheology. All model parts have been implemented in the in-home developed finite element package, TFEM [19]. In this section, the crystallization model is discussed. Since the model is originally shear-based, some equations had to be generalized to be applicable in extensional flows. For more information about numerical procedures and the rheological model, see Section 2.2.

3.2.1 Geometry

To solve the governing equations, first a geometry has to be defined. Because the crystallization process, both in terms of structure formation and crystal growth, is strongly dependent on temperature [17], it is chosen to model both the co-moving pistons and the sample. In this way, heat generated during crystallization in the sample can be transferred to the pistons by means of conduction or can be convected to the surroundings at the free surface. The (axisymmetric) geometry used in this chapter is given in Figure 3.3. Here, the gray areas are the pistons and the region in between is the polymer sample.
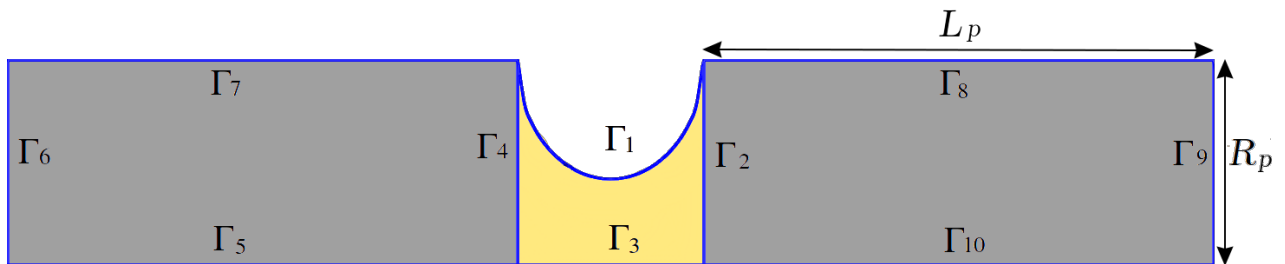
Figure 3.3: Initial axisymmetric geometry of a sample connected to two pistons (gray). Boundary Γ_3, Γ_5 and Γ_{10} are symmetry boundaries positioned at $r = 0$.

The geometries used in this chapter are given in Table 3.1. The dimensions are chosen, so that the effect of the compressed aspect ratio can be studied (as in the previous chapter). Therefore, the amount of pre-stretch is equivalent for all geometries. The dimensions of the pistons used in the simulations are $L_p = 10$ mm and $R_p = R_c = 4$ mm.

Table 3.1: Overview of the geometries studied with the crystallization model. The dimensions of the compressed and pre-stretched state are given. Simulations start from the (pre-stretched) initial shape.

N_{geo}	R_c [mm]	L_c [mm]	Λ_c	Compressed shape	R_0 [mm]	L_0 [mm]	Λ_0	ε_{pre}	Initial shape
1	4.0	1.1	0.3		1.68	3.64	2.17	1.74	
2	4.0	2.1	0.5		1.68	6.0	3.57	1.74	
3	4.0	3.8	1.0		1.68	10.0	5.92	1.74	
4	4.0	5.9	1.5		1.68	15.0	8.92	1.74	

3.2.2 Rheological model

To model the rheological behaviour of iPP, the same general equations as in Section 2.2 are used. Also compressibility is modeled in the same way. For the crystallization model, the backbone molecular stretch, Λ_i, is a commonly used parameter. This backbone stretch is defined as:

$$\Lambda_i = \sqrt{\mathrm{tr}\mathbf{c}_i/3}. \tag{46}$$

30

Here, the conformation tensor (of the i'th mode) is calculated with the XPP model given in Equation (12).

Boundary and initial conditions
Since in this part of the report the pistons are modeled as well, new boundary conditions have to be defined. At the start, the polymer sample is at rest.
  On the co-moving pistons, the velocity is prescribed as:

- $u_r = 0$ on Γ_2, Γ_4, Γ_5, Γ_6, Γ_7, Γ_8, Γ_9 and Γ_{10}

- $u_z = -v_{\text{piston}}$ on Γ_2, Γ_8, Γ_9 and Γ_{10}

- $u_z = v_{\text{piston}}$ on Γ_4, Γ_5, Γ_6 and Γ_7

On the symmetry line of the sample, the following applies:

- $u_r = 0$, on Γ_3

The remaining boundary is a free surface

- $\boldsymbol{u} \cdot \boldsymbol{n} = 0$, on Γ_1

where $\boldsymbol{n}$ is the unit normal vector on the surface S. On this boundary, the surface tension is applied using a Neumann boundary condition:

- $(-p\boldsymbol{I} + 2\eta_s\boldsymbol{D} + \boldsymbol{\sigma}) \cdot \boldsymbol{n} = \nabla_s \cdot (\hat{\gamma}(\boldsymbol{I} - \boldsymbol{nn}))$, on Γ_1

with ∇_s the surface gradient operator. A constant surface tension, $\hat{\gamma}$ is assumed (see Table A.2 in Appendix A.1).

3.2.3 Energy balance

The crystallization process, both in terms of structure formation and crystal growth, is strongly dependent on temperature [17]. To calculate the temperature, the following energy balance is solved:

$$\rho_k c_{p,k} \frac{DT}{Dt} = \lambda_k \nabla^2 T + \rho_k \chi_\infty \Delta H \dot{\xi} + \boldsymbol{\tau} : \boldsymbol{D}, \tag{47}$$

where ρ is the density, c_p the heat capacity at constant pressure, T the temperature, λ_k the thermal conductivity coefficient, χ_∞ the total crystallinity of the equilibrium state ($t = \infty$), ΔH the heat of fusion, ξ the space filling and subscript k denotes the material. Values of the parameters of the heat balance equation have been presented in Table A.2 in Appendix A.1. In this heat balance, heat conduction, latent heat release due to crystallization and shear heating is taken into account. The changes of specific heat, thermal diffusivity, and density with temperature or during phase transitions from the molten to the crystalline state are neglected.

Boundary and initial conditions
Isothermal experiments are considered, wherein the temperature is initially constant everywhere: $T(0) = T_0$ for all $\boldsymbol{x}$. The temperature of the air remains unaltered. Here, the temperature of the pistons is solved with Equation (47). For the temperature in the steel pistons, heat due to crystallization and shear heating are omitted.
The filament and pistons are subjected to heat loss at the free surface due to convection. Therefore, it is assumed that there is convection at the boundaries Γ_1, Γ_7 and Γ_8, according to:

- $-\lambda_k \nabla T \cdot \boldsymbol{n} = h_k(T - T_\infty)$, on Γ_1, Γ_7 and Γ_8.

Here, h_k is the convective heat transfer coefficient of the material k and $T_\infty (= T_0)$ the ambient temperature. To determine h_k, a Nusselt number of $Nu = h_k R_0 / \lambda_k \approx 0.72$ is assumed [31]. Using the thermal conductivity coefficient of iPP in Table A.2 in Appendix A.1 and $R_0 \approx 1$ mm, the used convective heat

transfer coefficient for the polymer is assumed to be $h_p = 79$ kg K^{-1}s^{-3}. Using the thermal conductivity coefficient of steel in Table A.2 in Appendix A.1 and $R_0 = R_p \approx 4$ mm, the used convective heat transfer coefficient for steel is assumed to be $h_s = 14 \cdot 10^3$ kg K^{-1}s^{-3}.

The temperature at the end of the pistons is assumed to be constant:

- $T = T_0$, on Γ_6 and Γ_9.

3.2.4 Quiescent crystallization model

Roozemond et al. [17] proposed a non-isothermal crystallization model that is based on the Kolmogoroff-Avrami expression. Space filling by primary crystallization is then given by

$$\xi(t) = \frac{\chi(t)}{\chi_\infty} = 1 - \exp\{-\Phi_0(t)\}, \tag{48}$$

where χ is the crystallized volume fraction at time t. The crystal volume Φ_0 represents the sum of the expected crystallized volumes of the different phases, $\Phi_0 = \sum \Phi_{0,i}(t)$. The subscript i indicates the phases of a multi-phase system ($\alpha-$, $\beta-$, $\gamma-$ and the mesophase).

For non-isothermal crystallization of spherulites, the crystal volumes $\Phi_{0,i}$ can be described by the Schneider's rate equations [51]. These equations are a set of differential equations, which describe the structure developing in quiescent conditions. The mean number of spherulites and their mean radius, surface and volume are calculated as follows:

$$\dot{\Phi}_{3,i} = 8\pi \dot{N}_i \qquad\qquad (\Phi_3 = 8\pi N) \qquad\qquad \text{'rate'} \tag{49}$$

$$\dot{\Phi}_{2,i} = G_i \Phi_{3,i} \qquad\qquad (\Phi_2 = 8\pi R_{\text{tot}}) \qquad\qquad \text{'radius'} \tag{50}$$

$$\dot{\Phi}_{1,i} = G_i \Phi_{2,i} \qquad\qquad (\Phi_1 = S_{\text{tot}}) \qquad\qquad \text{'surface'} \tag{51}$$

$$\dot{\Phi}_{0,i} = G_i \Phi_{1,i} \qquad\qquad (\Phi_0 = V_{\text{tot}}) \qquad\qquad \text{'volume'} \tag{52}$$

with the nucleation density N, the nucleation rate $\dot{N}$ and the growth rate G. The growth rate can be described by the following quadratic exponential function:

$$G_i(T) = G_{\text{max},i} \exp\{-c_{G,i}(T(t) - T_{G,\text{ref},i})^2\}. \tag{53}$$

Here, $G_{\text{max},i}$ is the growth rate at the reference temperature $T_{G,\text{ref},i}$ and $c_{G,i}$ a constant. Both the reference temperature and growth rate depend on the pressure. The relations used to describe the pressure dependency are [17]:

$$T_{G,\text{ref},i} = T_{G,\text{ref},i,0} + \zeta(p - p_0), \tag{54}$$

$$G_{\text{max},i} = G_{\text{max},i,0} \exp\{\alpha_i(p - p_0)\}, \tag{55}$$

where ζ, $T_{G,\text{ref},i,0}$, $G_{\text{max},i,0}$ and α_i are constant values and are given in Table B.1 in Appendix B.1. The reference pressure p_0 is 1 [bar]. The nucleation density and its derivative are given by a linear exponential function:

$$N_q(T) = N_{\text{ref}} \exp\{-c_N(T(t) - T_{N,\text{ref}})\}, \tag{56}$$

$$\frac{DN_q}{DT} = -c_N N_{\text{ref}} \exp\{-c_N(T(t) - T_{N,\text{ref}})\}. \tag{57}$$

Here, N_{ref} is the number of nuclei at the reference temperature $T_{N,\text{ref}}$ and c_N a constant. The values of N_{ref} and c_N are shown in Table B.1 in Appendix B.1. During solidification in a multi-phase system, every crystal form i generates a crystal volume fraction, $\Phi_{0,i}$, using a share of the available number of nuclei and having its own growth rate. The ratio by which the nuclei are divided between the crystal phases is not accessible experimentally. Therefore, the assumption is made that the allocation of nuclei to a given crystal form scales with the ratio of the individual crystal phase growth rates at the current

temperature and pressure. For isobaric conditions, the nucleation rate for a given crystal form is given by:

$$\dot{N}_{i,q} = f_{i,q} \frac{DN_q}{DT} \dot{T}, \tag{58}$$

with the quiescent growth rate fraction, $f_{i,q}$, defined as:

$$f_{i,q} = \frac{G_i}{\sum G_i}. \tag{59}$$

Here, the subscript q is used to define quiescent parameters. In the report of Roozemond et al. [17], the α-, β- and γ-phases of iPP are modelled. Since the β-phase only forms during flow, the quiescent growth rate fraction $f_{i,q}$ is restricted to $i = \alpha, \gamma$ and $f_{\beta,q} = 0$. With the nucleation density and individual growth rates modified for non-isothermal and isobaric conditions, the rate of space filling in a multi-phase structure is calculated as a function of time using:

$$\dot{\xi}_i(t) = (1 - \xi(t))\dot{\Phi}_{0,i}. \tag{60}$$

For computational purposes, the set of Schneider rate equations are numerically integrated using an explicit Euler scheme to calculate $\Phi_{0,i}$.

Initial conditions
The initial number of quiescent nuclei is calculated via Equation (58). Since the model is polymorph, the initial number of quiescent nuclei per phase is defined as:

$$N_{q,i}(T_0) = f_{i,q}N_q(T_0), \tag{61}$$

where the growth rate fraction, $f_{i,q}$, follows from Equation (59). The required growth rates per phase are also calculated by using the initial temperature, T_0.

3.2.5 Flow-induced nucleation and crystallization

The approach of coupling structure formation (crystallization) to deformation calculated with a rheological model on continuum level was first presented by Zuidema et al. [52]. The model presented by Zuidema was slightly modified by Steenbakkers et al. [53], who replaced the recoverable strain by backbone stretch, where shish started growing after a critical backbone stretch was reached in the high molecular weight tail. Instead, van Erp et al. [25] showed that a more realistic critical condition is a time integral over backbone stretch. This approach is also used by van Drongelen et al. [44] to model primary crystallization of LLDPE. An in-depth evaluation about the flow-induced-crystallization (FIC) model developed in our group, can be found in literature [25, 52, 53]. A different approach was used by Roozemond et al. [17], since in their model, shish growth is linked to flow deformation and not to a critical backbone stretch. It is shown that this model works well for the iPP used in this study. The model of Roozemond et al. [17] is explained below:

With flow, the total number of nuclei is the sum of the quiescent nuclei, N_q and the nuclei originating from FIC, N_f:

$$\dot{N}_{i,\text{tot}} = \dot{N}_{i,q} + f_{i,f}\dot{N}_f, \tag{62}$$

where $\dot{N}_{i,q}$ follows from (58). The total amount of nuclei is implemented in the Schneider rate equation (49). The flow enhanced nucleation rate is assumed to depend on the backbone stretch of a high-molecular weight mode via an exponential relation. This leads to:

$$\dot{N}_f = g_n(T,p)\exp\{\mu_n(\Lambda_{\text{HMW}}^2 - 1)\}. \tag{63}$$

Here, Λ_{HMW} is the high molecular weight stretch calculated according to (46), using the mode with the

longest relaxation time in the XPP constitutive model, and μ_n and g_n are scaling parameters. In both cases, it is envisioned that the stretch of the longest chains increases the number of aligned chain segments whose conformation is closer to the crystalline state. The scaling parameter g_n depends on temperature and pressure as follows:

$$g_n(T,p) = g_{n,\text{ref}}10^{c_{n,T}(T-T_{\text{ref}})+c_{n,p}(p-p_{\text{ref}})}. \tag{64}$$

All parameters in the two equations above are given in Table B.1 in Appendix B.1. For iPP in flow, the growth rate functions (given in (59)) are different, because of the possibility to grow β-phase crystals. The growth rate functions in flow are defined as [17]:

$$f_{\alpha,f} = (1 - f_{\beta,f})\frac{G_\alpha}{G_\alpha + G_\gamma}, \tag{65}$$

$$f_{\gamma,f} = (1 - f_{\beta,f})\frac{G_\gamma}{G_\alpha + G_\gamma}, \tag{66}$$

$$f_{\beta,f} = f_\beta, \tag{67}$$

with $f_\beta = 2 \cdot 10^{-3}$. The constant and low amount of β-phase can be explained in light of a limited region of space where it can be nucleated and lower crystal growth rate compared to the α- and γ-phase.

The growth of oriented structures (shish) is modeled differently for iPP as well. The growth mechanism is based on the "streamers" concept introduced by the Kornfield group [54]. Shish propagate in the lengthwise direction by addition of chain segments with length ξ_{seg}. Roughly speaking, the flow attaches these segments as crystals to the shish. Furthermore, it is assumed that the material deforms affinely. The expressions for the lengthwise propagation of shish then becomes:

$$\dot{L} = \dot{\gamma}\xi_{\text{seg}}. \tag{68}$$

Here, ξ_{seg} is the chain segment length given in Table B.1 in Appendix B.1. The lengthwise propagation of shish in iPP is modeled as a dependency on the shear rate, as shown in (68). Since the focus of this report is on elongational flows, the shear rate in this equation will be replaced with the magnitude of the rate of deformation tensor:

$$\dot{\gamma} = \dot{\gamma}_{\text{eff}} = \sqrt{2\boldsymbol{D} : \boldsymbol{D}}. \tag{69}$$

In case of (pure) uniaxial elongation, the effective strain rate becomes $\dot{\gamma}_{\text{eff}} = \sqrt{3}\dot{\varepsilon}$. Since it is assumed that the nucleation sites grow in the lengthwise direction, the total line nucleation density for kebabs, i.e. the specific shish length, is expressed as:

$$\dot{L}_{\text{tot}} = 2N_f\dot{L}, \tag{70}$$

where $\dot{L}_{\text{tot}}$ is the specific shish length growth. For the iPP model, there is no critical flow condition used for the formation of shish. However, for weak to mild flow conditions, no shish creation is observed, because nucleation rate $\dot{N}_f$ and propagation rate $\dot{L}$ are low for such flow conditions.

The undisturbed volume can be calculated in time from the calculated nucleation density and shish length. The crystalline volume fraction from the kebabs growing on shish is determined with rate equations. It is assumed that kebabs form on both the α- and γ-phase:

$$\dot{\Psi}_{1,\alpha} = 4\pi G_{\alpha,p}L_{\text{tot}}\frac{G_{\alpha,p}}{G_\alpha + G_\gamma}, \tag{71}$$

$$\dot{\Psi}_{1,\gamma} = 4\pi G_{\gamma,p}L_{\text{tot}}\frac{G_\gamma}{G_\alpha + G_\gamma}. \tag{72}$$

On α-kebabs, three different crystal morphologies can nucleate: α-parents, α-daughters and γ-daughters. In the model of Roozemond et al. [17], it is assumed that only the α-parents have increased growth rate due to orientation. The growth rate of the other two morphologies is always equal to the growth rate of the respective phases in quiescent conditions. It is assumed that on γ-kebabs, only γ-phase grows. These

conditions are mathematically expressed as follows:

$$\dot{\Psi}_{0,\alpha,p} = G_{\alpha,p}\Psi_{1,\alpha}\frac{G_{\alpha,p}}{G_{\alpha,p} + G_{\alpha,d} + G_\gamma}, \tag{73}$$

$$\dot{\Psi}_{0,\alpha,d} = G_{\alpha,d}\Psi_{1,\alpha}\frac{G_{\alpha,d}}{G_{\alpha,p} + G_{\alpha,d} + G_\gamma}, \tag{74}$$

$$\dot{\Psi}_{0,\gamma,p} = G_\gamma\Psi_{1,\alpha}\frac{G_\gamma}{G_{\alpha,p} + G_{\alpha,d} + G_\gamma}, \tag{75}$$

$$\dot{\Psi}_{0,\gamma,d} = G_\gamma\Psi_{1,\gamma}. \tag{76}$$

Here, subscripts p and d denote the volumes respectively in parent crystals or daughter crystals. The volume fraction of shish is neglected, because it is very small compared to the total volume of shish-kebabs.

Roozemond et al. [45] also propose that the growth of kebabs is promoted during the flow pulse and relaxation afterwards. This phenomenon is accounted for in the following way; during flow the growth rate of parents is increased with a factor G_{flow}. After flow, this effect relaxes due to chains relaxing toward their equilibrium conformation with a timescale λ_G. The growth rate of the parent lamellae $G_{\alpha,p}$ is given by:

$$G_{\alpha,p}(T,t) = G_\alpha(T)(1 + G_{\text{flow}}\exp\{-t/\lambda_G\}), \tag{77}$$

where $G_{\text{flow}} = 4$. The time scale with which the effect relaxes λ_G is 6 s in the extension experiments and 9 s in the slit flow experiments for the specific experimental conditions given in the paper of Roozemond et al. [45]. The extensional rheometer used to determine λ_G is a miniature extensional rheometer similar to a *Sentmantat extensional rheometer* (SER). This extensional measurement was performed at strain rates of about 3 to 20 s^{-1} and it is stated that the deformation is not perfectly uniaxial and probably at higher strains closer to biaxial [45]. It should be noted that (77) is not a general expression, because the relaxation time, λ_G depends on the flow type. To make this expression more general, it is modified by Grosso to [20]:

$$G_{\alpha,p}(T,t) = G_\alpha(T)(1 + G_{\text{flow}}\exp\{\text{tr}(\boldsymbol{c}_{\text{HMW}})\}), \tag{78}$$

with $G_{\text{flow}} = 0.009$. This equation will be used to model the growth rate of α-parents. Because of the flow-induced conformation, the formation of daughter morphology is less preferable. However, because growth of daughter crystals only becomes noticeable when the chains have relaxed to their equilibrium conformations, the growth rate for this species is taken equal to the quiescent growth rate:

$$G_{\alpha,d}(T,t) = G_\alpha(T). \tag{79}$$

To correct for the impingement of the shish-kebab structures, the Avrami equation (48) and equation (60) are adjusted. The total crystalline volume fraction and the space filling of each individual crystal phase is then given by:

$$\xi_{\text{tot}} = 1 - \exp\left[-\sum_{i,j}(\Phi_{0,i} + \Psi_{0,i,j})\right], \tag{80}$$

$$\dot{\xi}_i = (1 - \xi_{\text{tot}})\left(\dot{\Phi}_{0,i} + \sum_j \dot{\Psi}_{0,i,j}\right), \tag{81}$$

with the phase $i = \alpha, \gamma$ and the morphology $j = d, p$ (daughter or parent). The total space filling, ξ_{tot}, reaches 1 when the crystallization process is complete.

Initial conditions
Since the simulations start from rest, no flow is applied. This implies also that the initial number of flow-induced nuclei is approximately zero (10^{-6}). Also the space filling and shish growth parameters are set to approximately zero (10^{-6}). These values cannot be exactly zero, because the Schneider rate

equations are solved logarithmically for stability purposes. The initial values have been varied and the results do not depend on the exact initial values.

3.2.6 Crystallization effects on the rheology

It has been observed that shish strongly influence the rheology of the melt before the crystalline volume fraction reaches considerable proportions [17]. It is hypothesized that chains protruding from shish into the melt influence the rheology on a macroscopic scale. In the iPP model of Roozemond et al. [17], this is implemented in an empirical way by defining the effect of crystallization on the modulus as:

$$g_i = g_{0,i} 10^{\log_{10}(\mu) v_{\text{eff}}}, \tag{82}$$

wherein $g_{0,i}$ is the modulus of mode i given in Table A.1 in Appendix B.1, μ is the ratio between the modulus of the crystal and the one of the melt (for iPP $\mu = 10^4$) and v_{eff} is the effective space filling of shish-kebabs, given by;

$$v_{\text{eff}} = 1 - \exp\{-\pi L_{\text{tot}} r_{\text{eff}}^2\}, \tag{83}$$

where r_{eff} is the effective radius of a shish. Because this approach contains a number of uncertainties, the shish radius is an adjustable parameter on the order of 35 nm for iPP [17]. In this reference, good agreement with experiments was found for $r_{\text{eff}} = 50$ nm. In the work of Grosso et al. [20] molecular considerations are done. Because of these considerations, the effective shish radius and the modulus ratio between crystal and melt are adjusted to $r_{\text{eff}} = 30$ nm and $\mu = 5$ [20]. These values will be used in this work as well.

In case the more general expression for the α-parent growth rate is used (see Equation (78)), the Rouse relaxation times should be adjusted [20]. Housmans et al. [24] reports that the reptation time and the Rouse time are linear functions of the number densities of flow-induced precursors and nuclei [24]. The flow-induced nuclei are assumed to act as physical cross-links in the melt increasing the relaxation times of the high molecular weight chains. Following their approach, a dependence of the Rouse time only, on the number density of flow-induced nuclei in iPP is proposed:

$$\lambda_{s,i} = \lambda_{s,i_0} a_T a_p (1 + \alpha_s N_f), \tag{84}$$

where λ_{s,i_0} are the stretch relaxation times given in Table A.1 in Appendix B.1. Here a value of $\alpha_s = 10^{-4}$ mm^3 is derived by Grosso et al. for the used iPP [20].

3.3 Methods

In order to correctly measure the crystallization parameters with the simulations of the FiSER, multiple methods have to be introduced. The same methods as in Section 2.3 are used here. This includes the method for determining the force, measuring the radius of the filament, controlling the strain rate, correction for gravity and determining the shear correction factor. Besides, a method is developed to correctly measure the average percentage of crystallization. This will be explained below.

3.3.1 Crystallization measurements

During in-situ X-ray measurements, an X-ray beam is sent through the middle of the filament. The measured crystallization is then an "average" over the mid-radius of the filament. To mimic this procedure, a method has been developed to calculate the average crystallization over the radius of the sample. In the simulations, the total percentage of crystallinity is integrated over the dimensionless radius, $r^* = r/R_0$, according to:

$$\langle \chi_{\text{tot}} \rangle(t) = \int_0^1 \chi_{\text{tot}}(t, r^*) \, \mathrm{d}r^*, \tag{85}$$

where, $\langle \chi_{\text{tot}} \rangle$ is the total average crystallinity over the mid-radius of the filament. Since only about 5-6 elements are used at the middle of the sample, the amount of crystallization data acquired from the

mid-line of the sample is limited. Therefore, it is chosen not to use the mid-line, but a mid-region to process the data from the simulations (see Figure 3.4). In this way, more elements are included, resulting in more radial data points. It should be noted that this area is very small compared to the sample length at large strain rates. The same integration method can be used to for example determine the average fraction of α-phase.
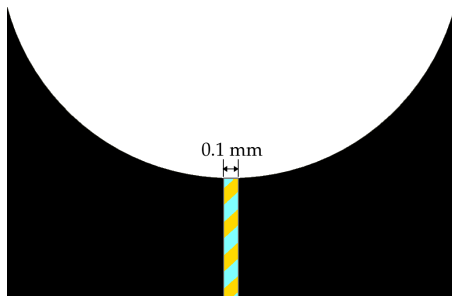

Figure 3.4: Geometry of a filament with a marked mid-region. The mid-region of 0.1 mm is used to increase the amount of elements to process crystallization data.

3.4 Results and discussion

In the first part of the results, the first geometry in Table 3.1 is simulated at a strain rate of 10 s^{-1} and a temperature of 140 °C. This is done to show the effect of nucleation on the rheological properties. Subsequently, the crystal growth is investigated for this sample at multiple temperatures and strain rates. This gives a clear overview of the effect of processing conditions on the crystallization in the FiSER. At last, the effect of the compressed aspect ratio on the crystallization is studied.

3.4.1 Effect of crystallization on the extensional viscosity

To investigate the crystallization in the FiSER, the first geometry in Table 3.1 is simulated. In these simulations, a strain rate of 10 s^{-1} and a temperature of 140 °C are applied. At this temperature, the quiescent crystallization is negligibly small. The result of the simulated extensional viscosity is shown in Figure 3.5. The pure uniaxial extensional solution, $\bar{\eta}_{\mathrm{XPP}}^{+}$, is given in Equation (33) (from the rheological XPP model). In Section 2.4, it is shown that in case of a pure rheological simulation, the pure uniaxial solution matches the simulated extensional viscosity at large strains. But, including the crystallization model results in a deviation from the pure uniaxial solution at large strains (as shown in Figure 3.5). This deviation is a result of flow-induced crystallization and nucleation growth. It is interesting to see that the deviation starts at a strain of approximately 3.8, while no crystallization is measured up until a strain of 4.5. When crystallization starts at a strain of 4.5, the simulated extensional viscosity rapidly increases. The primary increase in extensional viscosity (before crystallization) can be explained by the growth of flow-induced nuclei. According to Equation (63), the amount of flow-induced nuclei increases, because the stretch of the high molecular weight tail increases during the extensional flow in the FiSER. The flow-induced nuclei are assumed to act as physical cross-links in the melt, increasing the relaxation times of the high molecular weight chains [24]. As a result, the Rouse relaxation time is increased according to Equation (84). Therefore, the extensional viscosity increases. The relaxation times are only slightly affected by temperature before crystallization, because the temperature only increases with 0.2 °C ($\varepsilon_H < 4.5$). The secondary steep increase in the extensional viscosity is a result of crystallization. Because flow-induced crystals grow, the moduli of the polymer significantly increase, resulting in a steep increase of the extensional viscosity.
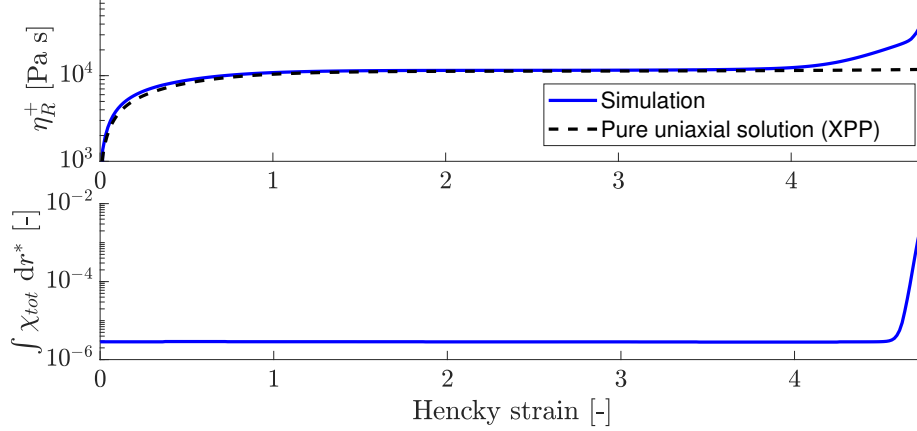
Figure 3.5: Extensional viscosity simulation result for a sample with a compressed aspect ratio of $\Lambda_c = 0.29$. The strain rate and temperature are $\dot{\varepsilon} = 10 \text{ s}^{-1}$ and $T_0 = 140 \text{ °C}$. The dashed line is the pure uniaxial solution calculated with the XPP model. The corresponding crystal fraction integrated over the radius is shown in the bottom figure.

Surprisingly, this crystallization is not constant over the mid-radius of the sample. At the centre, the percentage crystallinity is much lower than at the free surface. The crystallization distribution for the used geometry with a compressed aspect ratio of 0.29 is shown in Figure 3.6.
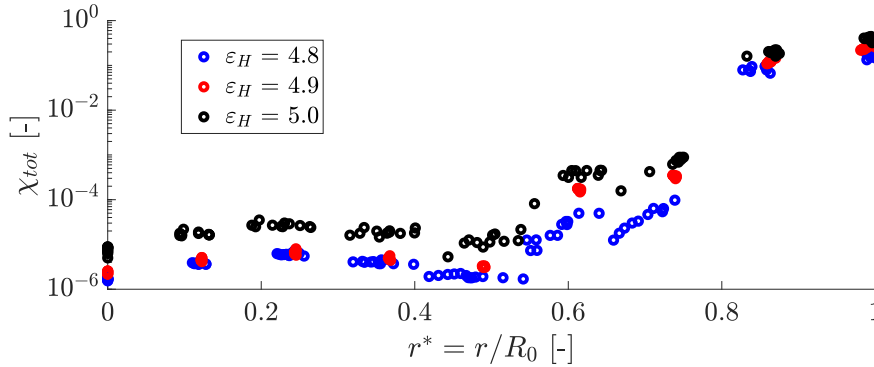
Figure 3.6: Crystallization distribution over the radius of the sample. Here, a sample with a compressed aspect ratio of $\Lambda_c = 0.29$ is used. The strain rate and temperature are $\dot{\varepsilon} = 10 \text{ s}^{-1}$ and $T_0 = 140 \text{ °C}$.

To explain the crystallization distribution over the radius, the period before crystallization is studied. In this study, the important parameters for the onset of flow-induced crystallization are visualized at the centre of the sample ($r = 0$) and at the free surface ($r = R_0$) in Figure 3.7. Starting with the magnitude of the rate of deformation tensor, $\dot{\gamma}_{\text{eff}}$, it can be seen that at the start of the simulation the flow field is non-uniform, due to shear contributions. The distribution of the magnitude of the rate of deformation tensor over the middle of the sample results in a distribution of high molecular weight stretch, Λ_{HMW}. This because the sample at the free surface is extended with a higher strain rate than at the centre of the sample ($\dot{\varepsilon}_{\text{eff}} = \dot{\gamma}_{\text{eff}}/\sqrt{3}$). As a result, the number of flow-induced nuclei increases faster at the free surface. Therefore, the lengthwise propagation of shish is higher at the free surface, resulting in a distribution of the total crystalline volume fraction and space filling over the radius of the sample (at $z = 0$).

Before crystallization, the temperature at the centre of the sample and at the free surface are almost the same (see Figure 3.7). But after crystallization, due to the rapid increase in crystallization at the free surface, the temperature of the sample is increased (according to Equation (47)). Since the crystallization starts at the free surface, also the temperature shows a distribution over the mid-radius of the filament.

38

Because iPP conducts heat well, the temperature at the centre of the polymer is increased due to the crystallization at the free surface. At higher temperatures, the growth rate of crystals is reduced. Since at the free surface the temperature increases rapidly because of crystallization, the temperature in the center of the sample increases as well due to convection. Therefore, the crystallization growth in the center is suppressed and the distribution of crystal volume fraction is increased even more. As a result, almost no crystal fraction is seen at the centre of the polymer. In Figure 3.7, also the amount of orientation, $\text{tr}(\boldsymbol{c}_{\text{avg}})$ is visualized. This orientation parameter is used in the growth rate of alpha parents (see Equation (77)). The orientation parameter is affected by the distribution of strain rates. This eventually also affects the distribution of crystallization fraction.
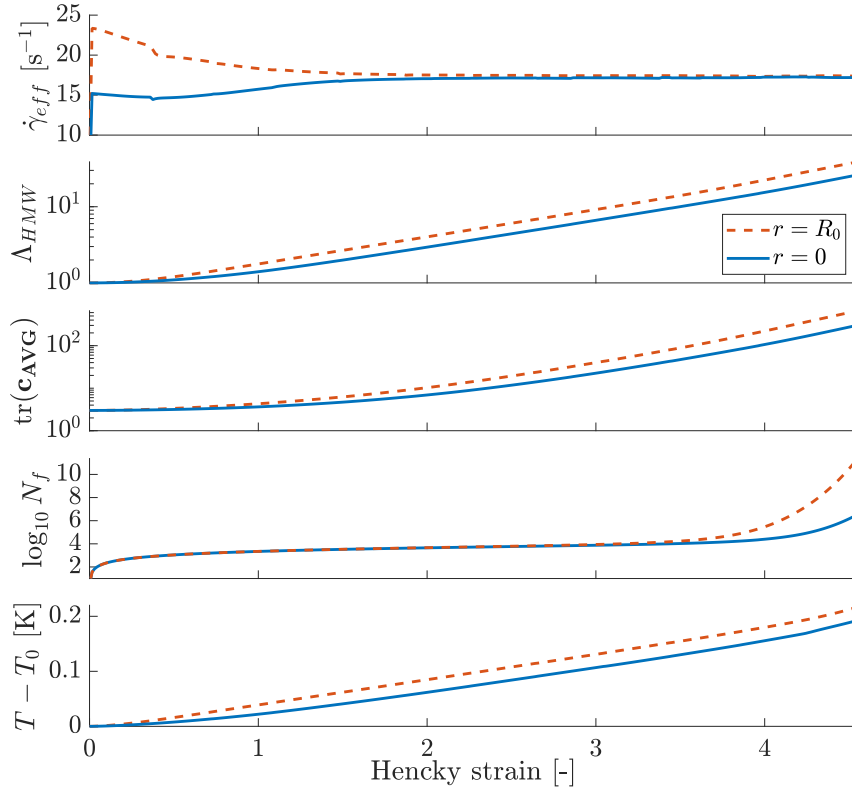
Figure 3.7: Important parameters for crystal growth before crystallization (for $\langle \chi_{\text{tot}} \rangle < 10^{-5}$) at a strain rate and temperature of $\dot{\varepsilon} = 10 \text{ s}^{-1}$ and $T_0 = 140$ °C. The used compressed aspect ratio is $\Lambda_c = 0.29$.

3.4.2 Effect of processing conditions

One of the goals of this study is to give advise about processing conditions and their effect on crystallization in a FiSER. In this part of the report, the effects of the applied strain rate and temperature on the crystallization of iPP is investigated. The flow in the FiSER is simulated for the following range of strain rates and temperatures: $\dot{\varepsilon} = [0.71, 1.71, 4.14, 10] \text{ s}^{-1}$ and $T = [110 \ 120 \ 130 \ 140]$ °C. In Figure 3.8, the simulated extensional viscosity for the different processing conditions is shown.
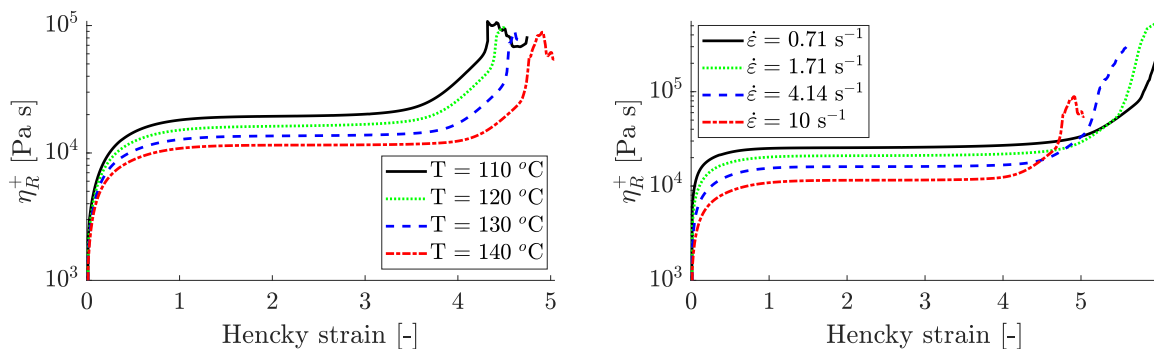
Figure 3.8: Simulated extensional viscosity for the different processing conditions. In the left figure, a strain rate of 10 s^{-1} is applied. In the right figure, the temperature was set to 140 °C.

From this figure it follows that the extensional viscosity decreases with increasing temperature and strain rate. When looking at the onset of crystallization, it can be seen that the strain at which crystallization starts is increased by increasing the temperature. On the other hand, an increase of strain rate, decreases the strain at which crystallization starts. To quantify this onset of crystallization, the critical crystallization strain ε_c was introduced by White et al. [15]. This strain is defined as the strain at which a sudden increase of flow-induced crystallization fraction is measured (i.e. a steep increase in extensional viscosity). White et al. [15] found that for small strain rates a constant critical crystallization strain exists for iPP. In their measurements, no radius-based controller was used, but an exponential velocity profile was imposed on the pistons instead. In this type of experiments, the length of the fluid filament is commanded to follow the exponential profile $L(t) = L_0 \exp(\dot{\varepsilon}t)$. The resulting extension rate imposed on the fluid filament can then be calculated from the radius decay and is higher than the applied strain rate. For an applied strain rate range of $0.01 < \dot{\varepsilon} < 0.15$ s^{-1} they found that the critical crystallization strain for iPP is $\varepsilon_c = 5.8$ [15].

In Figure 3.9, the average crystallization is plotted versus the Hencky strain for the different processing conditions. Here, the critical crystallization strain is marked by a circular marker. It can be seen that the critical crystallization strains are not equivalent for a strain rate range of $0.71 < \dot{\varepsilon} < 10$ s^{-1} but they depend on both the strain rate and temperature. Though not the same type of experiments are done, it can be concluded that no constant crystallization strain can be defined for iPP extended in the strain rate range of $0.71 < \dot{\varepsilon} < 10$ s^{-1}. By comparing Figure 3.8 with Figure 3.9 it is concluded that the strain at which the second steep upswing in extensional viscosity starts, matches the critical crystallization strain. This applies for all the simulations done here.

The simulations with an initial temperature of 110 °C show a significant increase of the average crystallization from the start of the simulation (see Figure 3.9). This is a result of quiescent crystallization. Because of crystallization, the sample is heating up. As a result, crystallization is suppressed and the rate of quiescent crystallization decreases. At larger strains, the molecules are stretched to an extend that flow-induced crystallization starts, resulting in a steep increase of the average crystallization. Because of the fast increase in crystallization, the radius of the sample slightly increases. As a result, the radius-based controller adjusts the velocity of the pistons in such a way that the pistons velocity can become negative or very high. This results in jumps in the extensional viscosity and average crystallization as shown in Figures 3.8 and 3.9. Simulations with an initial temperature of 130 and 140 °C show no quiescent crystallization, while for the simulations with an initial temperature of 120 °C, this depends on the applied strain rate (see Figure 3.9). For high strain rates, there is no time for the sample to crystallize under quiescent conditions (at 120 °C). Though, the goal is to study flow-induced crystallization only, it is chosen to use all the data, because a clear distinction between quiescent and flow-induced crystallization can be seen.
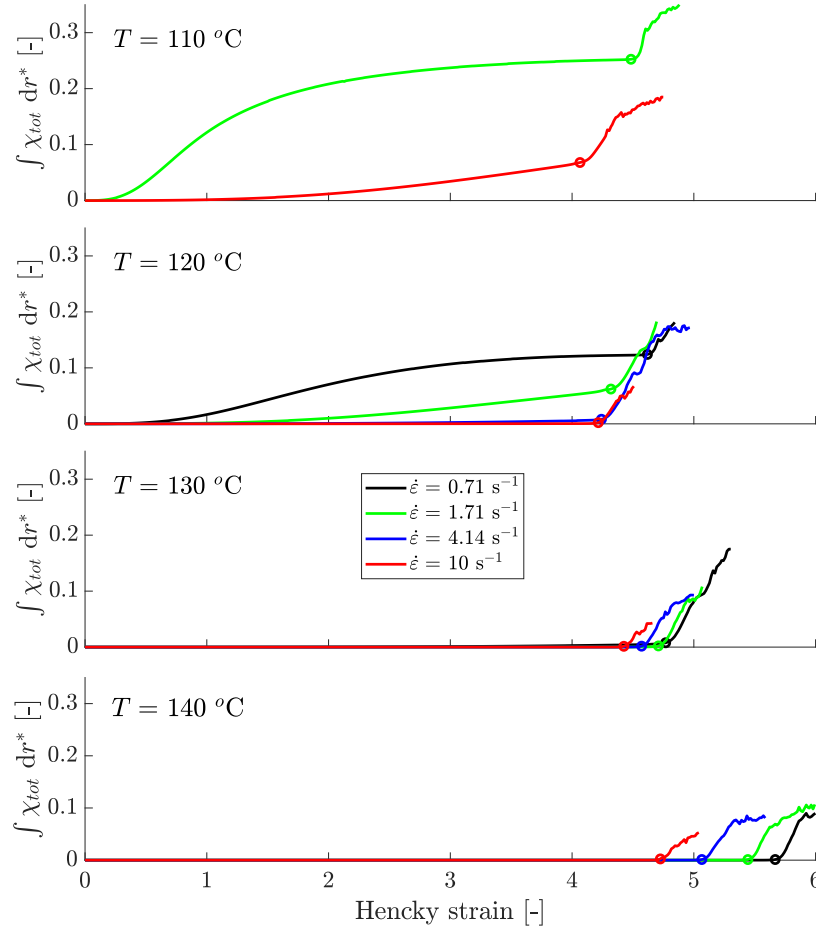
Figure 3.9: Average crystallinity for the different processing conditions, with a compressed aspect ratio of $\Lambda_c = 0.29$. The markers visualize the critical crystallization strain ε_c at each processing condition.

An overview of the dependency of the critical crystallization strain on the different processing conditions is given in Figure 3.10. From this figure two general trends follow:

- The critical crystallization strain is increasing with increasing temperature (excluding the simulation of $T = 110$ °C and $\log(\dot{\varepsilon}) = 0.54$).
- The critical crystallization strain is decreasing with increasing strain rate.

It should be noted that the critical crystallization strains at $T = 110$ °C are affected by the quiescent crystallization. This can be seen by the fact that the crystallization starts at small strains, i.e. at a weak flow (see Figure 3.9). This is also true for the strain rate of 0.71 s^{-1} is and 1.71 s^{-1} is at $T = 120$ °C. In Figure 3.10, it can be seen that the critical crystallization strain at $T = 110$ °C and $\dot{\varepsilon} = 1.71$ (or $\log(\dot{\varepsilon}) = 0.54$) is inconsistent with the general trend. The other simulations, which are less affected by quiescent crystallization, are consistent with the pure flow-induced crystallization simulations.

41
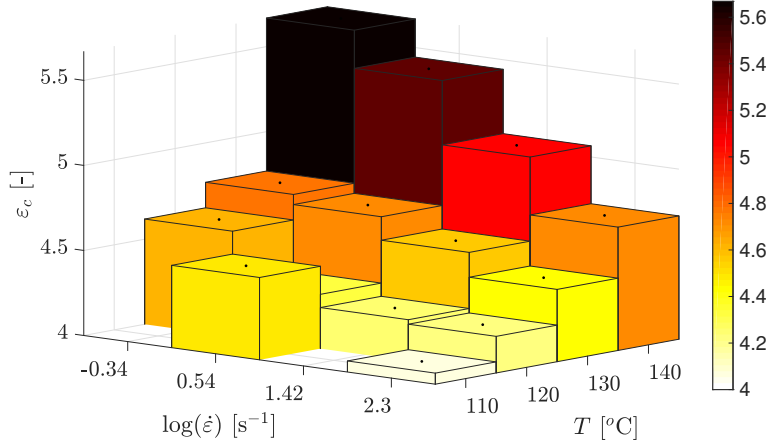
Figure 3.10: Three-dimensional representation which shows the dependency of critical crystallization strain on the strain rate and temperature for a sample with a compressed aspect ratio of $\Lambda_c = 0.29$.

3.4.3 Dependency of crystallization on the aspect ratio

Since the shear contributions at the start of the simulation seem to affect the flow-induced crystallization, a study on the dependency of crystallisation on the aspect ratio is done. It is shown in Section 2 that by increasing the compressed aspect ratio the shear contributions decrease. To investigate whether this reduces the crystallization distribution over the mid-radius of the sample, the geometries in Table 3.1 are simulated at a strain rate of 10 s^{-1} at 130 and 140 °C. A strain rate of 10 s^{-1} is chosen because it has the shortest simulation time of the strain rates used in this study. At the chosen temperatures, quiescent crystallization growth is negligible and therefore crystallization only consists of flow-induced-crystallization.

In Figure 3.11, the distribution of the crystallization over the radius for geometry 2 (upper) and 4 (bottom) are given. These geometries have a compressed aspect ratio of 0.5 and 1.5, respectively. In this figure it can be seen that the distribution of crystallization is affected by the initial dimensions of the sample. For a higher compressed aspect ratio, using the same pre-stretch, the difference in crystallization over the radius of the sample is reduced. In other words, the amount of crystallinity at the free surface is close to that at the centre of the sample. Though, for the geometry used in the bottom figure an initial aspect ratio of $\Lambda_0 = 8.9$ is used, there still is a small distribution of crystallization over the mid-radius of the sample.
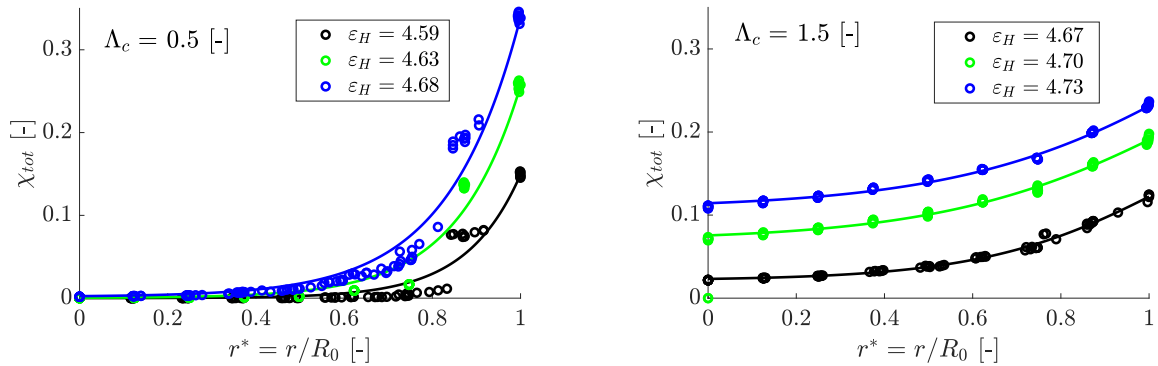

Figure 3.11: Crystallization distributions results for geometry 2 and 4 simulated at a strain rate of 10 s^{-1} and temperature of 130 °C. For the left figure a compressed aspect ratio of $\Lambda_c = 0.5$ is used and for the right figure a compressed aspect ratio of $\Lambda_c = 1.5$ is used. The lines are a guide for the eye.

For the geometries in Table 3.1, the corresponding critical crystallization strains are given in Figure 3.12. In these simulations, a strain rate of $\dot{\varepsilon} = 10 \text{ s}^{-1}$ is used and the temperature is set to 130 and 140 °C. The critical crystallization strain seems to be converging when increasing the aspect ratio at both temperatures. This is as expected, because the contribution of the shear components is decreasing when increasing the aspect ratio. However, because of the stationary flow near the pistons there will always be some shear effects that affect the flow and thereby the onset of crystallization. Nevertheless, from upon a compressed aspect ratio of $\Lambda_c = 1.5$ ($\varepsilon_{pre} = 1.74$, so $\Lambda_0 = 8.9$), the onset of crystallization will only slightly increase. Therefore, it is advised to use an initial aspect ratio of at least $\Lambda_0 = 8.9$, when performing in-situ crystallization measurements in a FiSER. For pure rheological measurements a much lower pre-stretch is required to make the shear contributions disappear in the extensional viscosity. For a sample with $\varepsilon_{pre} = 0.8$ and $\Lambda_0 = 2.5$, the error due to shear contributions on the extensional viscosity is less than 5 % (see Figure 2.14). Therefore, the sample dimensions are even more important for in-situ crystallization measurements in a FiSER.
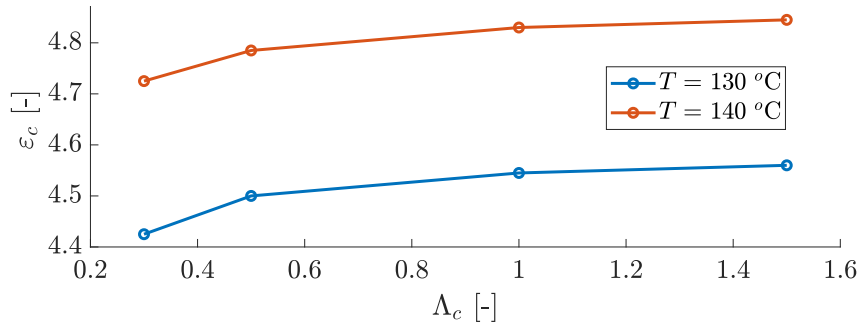

Figure 3.12: Critical crystallization strain as a function of the compressed aspect ratio ($\dot{\varepsilon} = 10 \text{ s}^{-1}$).

To quantify the effect of the aspect ratio on in-situ crystallization measurements, the simulated average crystallization is plotted for different aspect ratios in Figure 3.13. As mentioned above, the critical crystallization strain is different per aspect ratio. Therefore, the critical strain is subtracted from the Hencky strain, resulting in strain definition in only the flow-induced crystallization regime. Since for small aspect ratios, the crystallization only grows at the free surface, the average crystallization also grows slower. This can be seen in the figure above, because the rate of crystallization is lower for small aspect ratios. Unfortunately, the simulations crash at some point after crystallization. This because crystallization in the middle of the filament affects the rheology in such a way that the mid-radius of the sample drastically changes. As a result, the controller drastically changes the piston velocity and the simulation becomes unstable. Therefore, it is not possible to study the crystallisation rate in more detail. Nevertheless, a clear relation between the aspect ratio and the onset of crystallization is shown. Besides, an increase in aspect ratio results in less difference in crystallization fractions over the middle of the sample. From these findings has been concluded that an initial aspect ratio of at least $\Lambda_0 = 8.9$ (with $\varepsilon_{pre} = 1.74$) is needed to perform proper in-situ crystallization measurements in a FiSER. These measurements will then only contain a small distribution of crystallization fraction over the mid-radius of the sample.
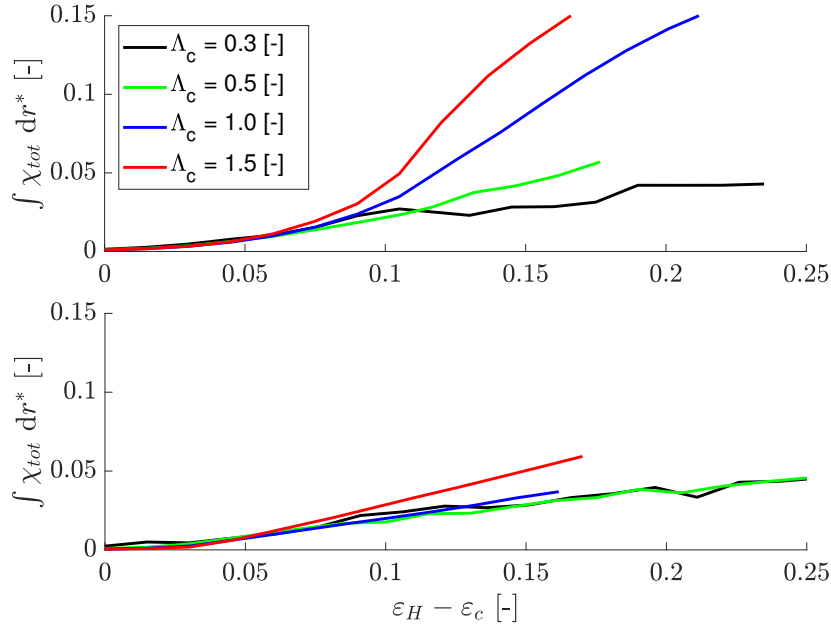
Figure 3.13: Average crystallization for different aspect ratios at $T = 130$ °C (upper) and $T = 140$ °C (bottom). A strain rate of $10\ \mathrm{s}^{-1}$ is used.

3.5 Summary

In this work, finite element simulations are developed which can capture the rheology and crystallization of iPP in a filament stretching rheometer. A broad range of processing conditions have been investigated by varying the initial temperature and the applied strain rate. From these simulations it follows that the extensional viscosity increases in steps. The first increase is due to the increase in the Rouse relaxation times during flow. This increase is a result of the increase of nuclei during flow, which are assumed to act as physical cross-links. The second steep increase is a result of crystal growth. During the formation of crystals, a sharp increase in the moduli of the polymer sample can be seen. As a result, the extensional viscosity rapidly increases.

While White et al. [15] found a constant critical crystallization strain at low strain rates, it has been shown that this is not the case for the simulations done in this study for a strain rate range of $\dot{\varepsilon} > 0.71$ s^{-1}. Namely, the critical crystallization strain decreases with increasing strain rate. Besides, an increase in temperature increases the critical crystallization strain. So, the behaviour is more complex because the critical crystallization strain depends on the strain rate and temperature.

Before crystallization, the shear contributions at the pistons affect the flow in such a way that no pure uniaxial extensional flow is present in the FiSER. Therefore, the molecular stretch is not homogeneously distributed over the radius of the filament. The molecular stretch determines the amount of flow-induced nuclei and therefore affects the onset of crystallization. As a result of the molecular stretch distribution, the crystallization fraction at the free surface is higher than the crystallization fraction at the centre of the sample, resulting in a distribution of crystallization over the radius of the sample. Because the shear contributions at the pistons are dependent on the initial aspect ratio, it has been shown that the distribution of crystallization fraction can be reduced by increasing the initial aspect ratio. Subsequently, the effect of the initial aspect ratio on the critical crystallization strain has been studied. It followed that an initial aspect ratio of at least $\Lambda_0 = 8.9$ has to be used to perform proper in-situ crystallization measurements in a FiSER. These measurements will then only contain a small distribution of crystallization fraction over the mid-radius of the sample.

B Appendix

B.1 Crystallization characterization

The meaning of the different parameters in tables below can be found in the List of symbols.

Table B.1: Crystallization parameters for iPP. The second column is retrieved from the work of Roozemond et al. [17]. The third column is derived by molecular considerations (see the work of Grosso et al. [20]) and is used in this report.

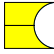|	extens. [17]			molec. [20]			Units
Nucleation density							
N_{ref}	$2.2 \cdot 10^{15}$			$2.2 \cdot 10^{15}$			$1/\mathrm{m}^3$
$T_{N,\mathrm{ref}}$	383			383			K
c_N	0.211			0.211			$1/\mathrm{K}$
Crystal growth	α-phase	β-phase	γ-phase	α-phase	β-phase	γ-phase	
$G_{\mathrm{max},0}$	$4.8 \cdot 10^{-6}$	$7.1 \cdot 10^{-6}$	$1.1 \cdot 10^{-6}$	$19.2 \cdot 10^{-6}$	$7.1 \cdot 10^{-6}$	$4.4 \cdot 10^{-6}$	m/s
$T_{G,\mathrm{ref},0}$	363	380	377	363	380	377	K
c_G	$2.3 \cdot 10^{-3}$	$6.6 \cdot 10^{-3}$	$3.5 \cdot 10^{-3}$	$2.3 \cdot 10^{-3}$	$6.6 \cdot 10^{-3}$	$3.5 \cdot 10^{-3}$	$1/\mathrm{K}$
α	0	0	$7.7 \cdot 10^{-4}$	0	0	$7.7 \cdot 10^{-4}$	1/bar
ζ	27			27			K/bar
FIC							
$g_{n,\mathrm{ref}}$	10^{12}			10^{13}			$1/(\mathrm{m}^3\mathrm{s})$
$c_{n,T}$	-0.016			-0.016			$1/\mathrm{K}$
$c_{n,p}$	$7.58 \cdot 10^{-4}$			$7.58 \cdot 10^{-4}$			1/bar
μ_n	0.03			0.015			-
ξ_{seg}	$5 \cdot 10^{-9}$			$5 \cdot 10^{-9}$			m

4 Outlook: X-ray induced cross-linking during in-situ crystallization measurements in a FiSER

In this outlook, the progress of comparing simulations of a HMW iPP in a filament extensional stretching rheometer with in-situ crystallization measurements is given. The iPP used is Sabic PP 531P ($M_w = 740$ g/mol and $M_n = 140$ g/mol). The same methods and models are used as in Chapter 3. The in-situ crystallization measurements with the FiSER are performed by J. Pepe [16].

4.1 Geometry

The dimensions of the sample used in the simulations are given in Table 4.1. These dimensions match the ones used in the in-situ crystallization measurments performed by J. Pepe [16].

Table 4.1: Dimensions of the sample used by J. Pepe in the in-situ crystallization measurements [16]. The dimensions of the compressed and pre-stretched state are given. Simulations start from the (pre-stretched) initial shape.

N_{geo}	R_c [mm]	L_c [mm]	Λ_c [-]	Compressed shape	R_0 [mm]	L_0 [mm]	Λ_0 [-]	$\varepsilon_{\mathrm{pre}}$ [-]	Initial shape
1	4.00	1.80	0.45		2.37	3.70	1.56	1.05	

4.2 Characterization

Since the used HMW iPP was not fully characterized yet, the model described in Chapter 3 could not be used initially. To solve this problem, firstly a rheological characterization is done by means of small amplitude oscillatory shear and FiSER measurements. Second, crystallization parameters are assumed using the results of the work of Troisi et al. [47] on iPP with a lower molecular weight. Both characterizations are explained in the following subsections.

4.2.1 Rheology

To characterize the rheological behaviour of the HMW iPP, the relaxation spectrum is determined by J. Pepe [16]. The results are given in Table 4.2. The activation energy at a reference temperature of $T_{\mathrm{ref}} = 200$ °C is $E_a = 36.75$ kJ/mol [16]. Since the XPP model is used to capture the rheological behaviour of iPP, also the non-linear parameters of this constitutive relation have to be determined. To do so, extensional viscosity measurements at a temperature of 200 °C are fitted with pure uniaxial XPP predictions. The best fit is shown in Figure 4.1. The corresponding non-linear parameters are given in Table 4.2. Since for these characterization measurements only two different strain rates are applied, the corresponding XPP parameters are only valid for these limited strain rates ($\dot{\varepsilon} = 0.1 \, \mathrm{s}^{-1}$ and $\dot{\varepsilon} = 0.4 \, \mathrm{s}^{-1}$).

Table 4.2: Viscoelastic model parameters of the XPP model for the HMW iPP at a reference temperatures of $T_{\mathrm{ref}} = 200$ °C.

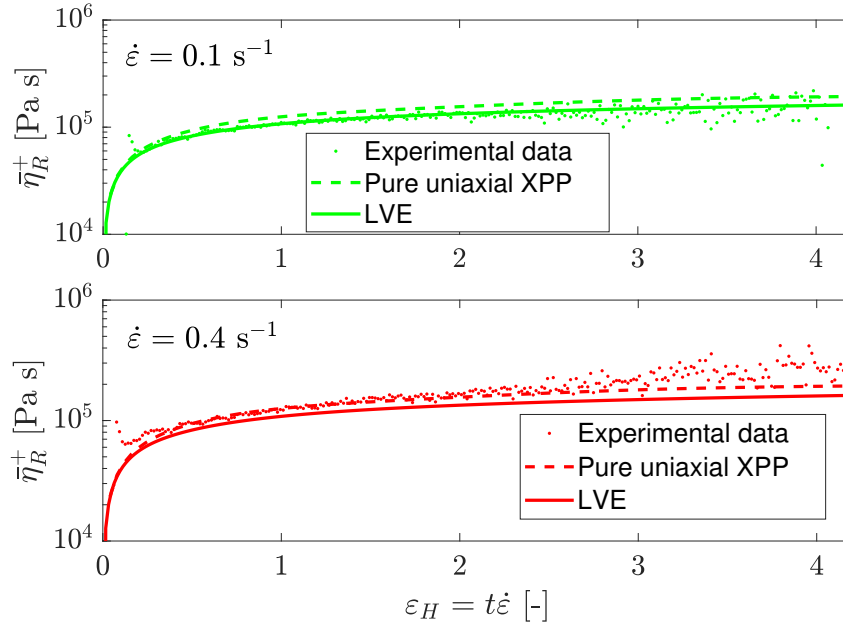| N	η_i [Pa s]	$\lambda_{b,i}$ [s]	$\lambda_{s,i}$ [s]	ν_i [-]
1	$7.20 \cdot 10^2$	0.00649	0.0011	2
2	$2.76 \cdot 10^3$	0.0475	0.0079	2
3	$8.39 \cdot 10^3$	0.249	0.0415	2
4	$1.75 \cdot 10^4$	1.25	0.2083	2
5	$2.34 \cdot 10^4$	6.29	1.0483	2
6	$2.23 \cdot 10^4$	35.9	5.98	0.33

Figure 4.1: Extensional viscosity measurements performed by Pepe et al. [16] at $T_{\text{ref}} = 200$ °C. These measurements are used to determine the non-linear parameters of the XPP model for the HMW iPP.

4.2.2 Crystallization

Since it was not possible to fully characterize the HMW iPP within the time span of this project, it is assumed that the flow-induced crystallization parameters of the HMW iPP are the same as the ones of the iPP given in Chapter 3. This assumption is based on the work of Troisi et al. [47]. Herein, only the growth rate and nucleation density are taken as a function of the molecular weight of iPP. It is concluded that the model prediction of the crystallization temperatures and of the volume fractions of the α- and γ-phase show reasonably good agreement with the experimental data, fully capturing the experimentally observed trends. To find the correct growth rate and nucleation density function, the values found by Troisi et al. [47] for different molecular weights are linearly interpolated. At a molecular weight of $M_w = 740$ g/mol, the resulting crystallization parameters of the HWM iPP are:

- $G_{\text{max},\alpha} = 3$ μm/s
- $G_{\text{max},\gamma} = 0.65$ μm/s
- $N_{\text{ref}} = 2.2 \cdot 10^{12}$ 1/mm^3
- $T_{N,\text{ref}} = 418$ K

In the upcoming results, these parameters are used. For the other (unchanged) crystallization parameters see Chapter 3 and Appendix B.1.

4.3 Results and discussion

4.3.1 Comparing simulations to FiSER measurements

With the characterization described above and the geometry given in Table 4.1, the extension of a HMW iPP in the FiSER is simulated. The temperature is 130 °C and the applied strain rate is 0.1 s^{-1}. The results of the simulated extensional viscosity are given in Figure 4.2. It can be seen that the initial set of parameters (with $\alpha_s = 10^{-4}$ mm^3) is not able to describe the measured extensional viscosity. This measurement was done at the TU/e by Pepe et al. [16]. The measured extensional viscosity starts increasing from the pure uniaxial solution of the XPP model at a Hecnky strain of 1. As previously explained in Chapter 3, this increase is the result of the increase of flow-induced nuclei, which are

assumed to act as physical cross-links. The effect of these cross-links on the rheology is modeled via the Rouse time as shwon in Equation 84. Since with the current simulation which uses $\alpha_s = 10^{-4}$ mm^3 the increase in extensional viscosity is overpredicted for the HMW iPP, multiple simulations are performed with different values for α_s. The results of these simulations are shown in Figure 4.2. Here it can be seen that the simulated extensional viscosity decreases if the value of α_s decreases. The measurement shows good agreement with the simulation that uses a value of $\alpha_s = 8 \cdot 10^{-7}$ mm^3.
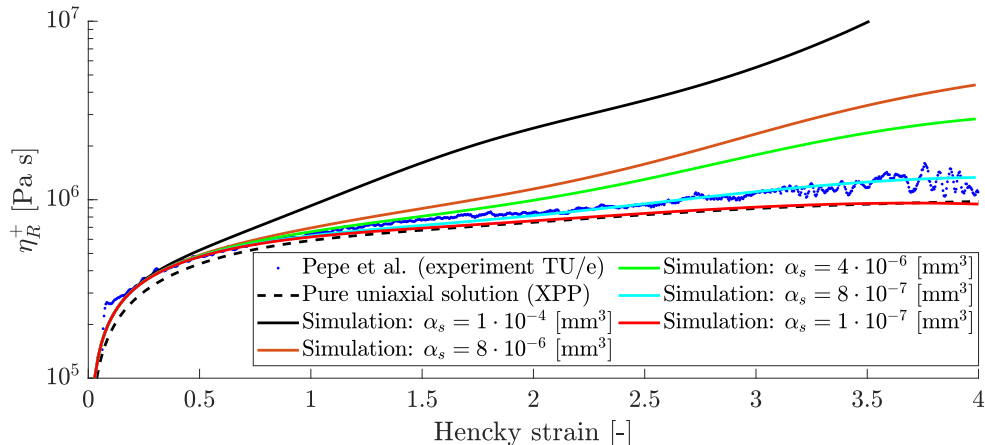
Figure 4.2: Extensional viscosity as a function of the strain for $T = 130$ °C and $\dot{\varepsilon} = 0.1$ s^{-1}. The solid lines are the result of the finite element simulation using the parameters as described in Section 4.2.2, but different values of α_s. The experimental data is taken from Pepe et al. [16]. This data is produced with the home-build FiSER without in-situ crystallization measurements. .

Pepe et al. [16] also performed a filament stretching experiment with in-situ crystallization measurements. This experiment was done at the Alba X-ray synchroton facility using a X-ray beam [55]. The flux of this beam is The measured extensional viscosity is compared to the one without X-rays in Figure 4.3. In this figure also the results of simulations with different values of α_s are shown. Surprisingly, the two measurements with and without X-rays do not match. According to the simulation which describes the measurement done without an X-ray beam, $\alpha_s = 8 \cdot 10^{-7}$ mm^3 should be used for this material. But for $\alpha_s = 8 \cdot 10^{-6}$ mm^3, the simulation is able to describe the measurement with an X-rays up to a Hencky strain of 3.

From the in-situ crystallization measurements it follows that up to a strain of 3, there is no flow-induced crystallization [16]. Nevertheless, the extensional viscosity is higher for the measurement with X-rays compared to the measurement without X-rays in this region. Since no strain hardening is expected to happen, according to the pure uniaxial XPP solution, this increase of the extensional viscosity must originate from something else. In this work, it is believed that this is the result of physical cross-linking. This cross-linking can originate from either nuclei created by the X-ray beam or from nuclei created during flow. Since the flow-induced cross-linking is already captured in the measurement without X-rays by using $\alpha_s = 8 \cdot 10^{-7}$ mm^3, the resulting increase in extensional viscosity is a result of the X-ray beam. Here it is assumed that the X-ray beam only initiates cross-linking in the polymer. For strains larger than 3, a steep increase in the extensional viscosity for the measurement with X-rays can be seen in Figure 4.3. According to Pepe et al. [16], the upswing is a result of flow-induced crystallization. In the following subsection, an improvement to the current model will be suggested to capture the effect of X-ray induced cross-linking. It is aimed to improve to model in such a way, that also the second upswing at $\varepsilon_H > 3.5$ can be captured as well.
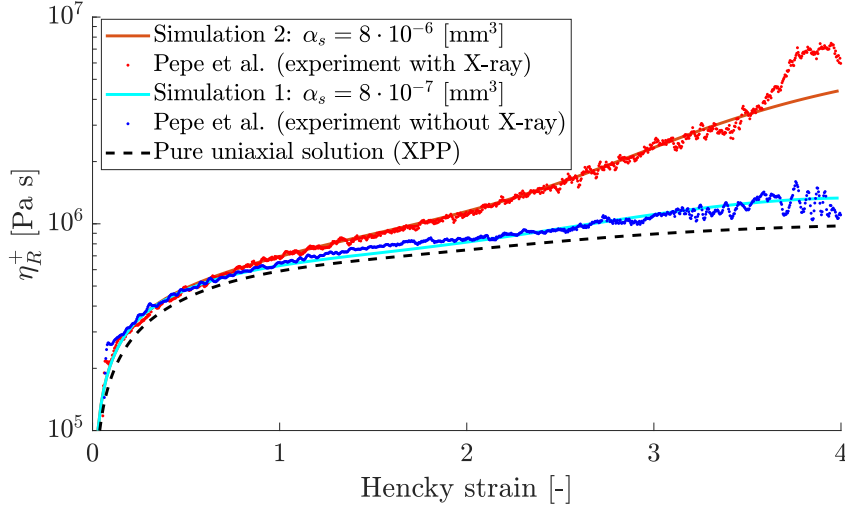
Figure 4.3: Transient extensional viscosity measurements by Pepe et al. [16] compared to simulations of the FiSER. For the measurements with a high intensity X-ray beam, the extensional viscosity is increased. This measurement was done at the Alba X-ray synchroton facility using a X-ray beam to perform in-situ crystallization measurements [55]. The measurements and simulations were performed at a strain rate of $\dot{\varepsilon} = 0.1$ s^{-1} at $T = 130$ °C.

4.3.2 Radiation-induced cross-linking

In the same way as $\alpha_s N_f$ in Equation (84), the parameter $\beta_s N_b$ is introduced to describe physical cross-linking due to X-rays. This is done by assuming that X-ray induced nuclei N_b is increasing as a function of the intensity of the X-ray beam and time according to:

$$N_b = c_b I_b t, \tag{86}$$

with I_b the intensity of the beam in kg s^{-3} and c_b a constant in s^{2}kg^{-1}mm^3 and t the time in s. Implementing the relation for the X-ray induced nuclei in Equation (84) gives:

$$\lambda_{s,i} = \lambda_{s,i_0} a_T a_p (1 + \alpha_s N_f + \beta_s N_b) = \lambda_{s,i_0} a_T a_p (1 + \alpha_s N_f + b_s t), \tag{87}$$

with $b_s = \beta_s c_b I_b$ in s^{-1}. In literature it has been shown that in polymers the cross-link density is proportional to the radiation dose $R_{\text{X-ray}}$ [56]:

$$q = q_0 R_{\text{X-ray}}. \tag{88}$$

Here q is the proportion of units cross-linked and q_0 the proportion of units cross-linked per unit of radiation dose. By assuming that the radiation dose is proportional with time and intensity: $R_{\text{X-ray}} \sim tI$, a linear relation between the amount of X-ray induced nuclei (i.e. cross-links) and time is suggested.

Since the two simulations in Figure 4.3 match the measured extensional viscosities with and without beam, it is possible to estimate a value of b_s. This is done by using Equation (84) and (87). First the measurements with and without beam, shown in Figure 4.3, are simulated with the model that does not include radiation-induced nucleation (see Equation (84)). For the measurement without beam, the value of $\alpha_{s,1} = 8 \cdot 10^{-7}$ mm^3 is found and is taken as the correct constant to describe the flow-induced crystallization of iPP (also in the presence of the X-ray beam). For the measurement with the X-ray beam, the value of $\alpha_{s,2} = 8 \cdot 10^{-6}$ mm^3 is found when using Equation (84). This value is used to determine b_s according to:

$$\alpha_{s,1} N_{f,1}(t) + b_s t = \alpha_{s,2} N_{f,2}(t) \tag{89}$$

Here, $N_{f,i}$ is the simulated nucleation density for the model without radiation-induced nucleation. The subscript $_1$ is used to describe the measurement without beam and subscript $_2$ is used to describe the measurement with beam. The difference between the flow-induced nucleation terms is given by $\Delta N_f^*(t) = \alpha_{s,2}N_{f,2}(t) - \alpha_{s,1}N_{f,1}(t)$. This implies that the value of b_s can be determined by fitting $b_s t$ to $\Delta N_f^*(t)$. In Figure 4.4, it can be seen that at the start of the simulation, $\Delta N_f^*(t)$ is approximately linear with time. In this region a value of $b_s = 0.23$ s^{-1} is found (for $0 \leq t < 20$). At later times, this relation does not hold anymore.
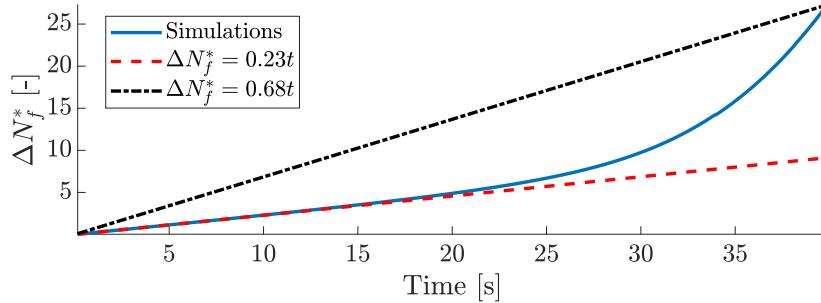
Figure 4.4: Flow-induced nucleation difference ΔN_f^* as a function of time. To create this figure, $N_f^* = N_{f,i}\alpha_{s,i}$ is used for the simulations with ($i = 2$) and without ($i = 1$) X-ray beam (see Equation (89)). The dashed lines are fits, where the slope equals b_s. Since a strain rate of $\dot{\varepsilon} = 0.1$ s^{-1} is used, the sample is extended with a strain of $\varepsilon_H = 1$ per 10 seconds.

To see whether the radiation-induced nucleation model can capture the second upswing in extensional viscosity for the measurements with an X-ray beam in Figure 4.3, multiple simulations are performed with different values of b_s. The following values of b_s are simulated: $b_s = [0.0023, 0.023, 0.23, 0.68, 2.3]$ s^{-1}, where $b_s = 0.23$ s^{-1} is found from $\Delta N_f^*(t)$ in Figure 4.4. The results of these simulation are shown in Figure 4.5. Here, it can be seen that the simulation with $b_s = 0.23$ s^{-1} shows good agreement with the measurement with a high-intensity X-ray beam up to a Hencky strain 3.5. After this strain, the second upswing in extensional viscosity is not predicted. When b_s is decreased with a factor 10-100 (i.e. $b_s = 0.023$ or $b_s = 0.0023$ s^{-1}), the extensional viscosity matches the measurement without X-ray beam. This result suggest that the intensity of the beam used in Alba [16] should be reduced by at least a factor 10-100, to eliminate the effect of radiation-induced nucleation on the FiSER measurements.
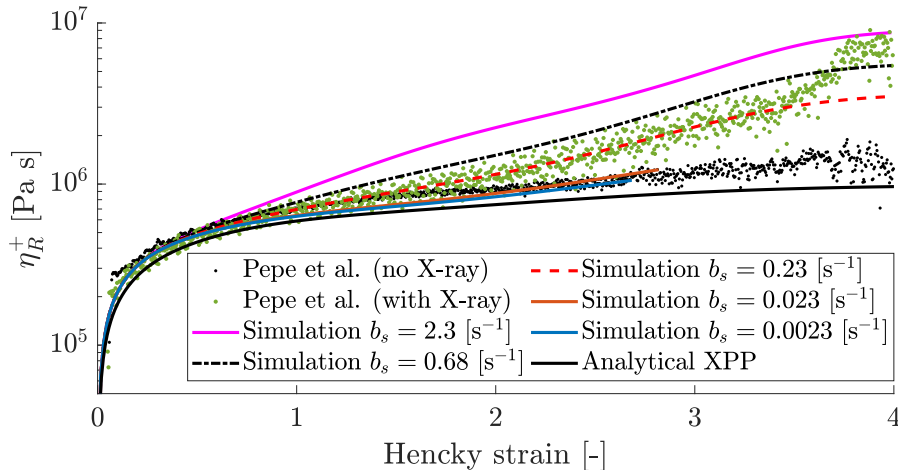

Figure 4.5: Extensional viscosity for simulations using the model that includes X-rays. For all simulations, $\alpha_s = 8 \cdot 10^{-7}$ mm^3 is used. The measurements and simulations were done at $\dot{\varepsilon} = 0.1$ s^{-1} at $T = 130$ °C.

The amount of flow-induced nuclei for the simulations with and without the X-ray cross-linking model are shown in Figure 4.6. Here, $b_s = 0.23$ s^{-1} is taken as the improved model with radiation-based nucleation. Though the X-ray model does not show a second steep increase in extensional viscosity, it does show an increase in flow-induced nuclei. Because the relaxation time increases in time, due to radiation-based cross-linking, the amount of flow-induced nuclei also increases. But as shown in Figure 4.6, the amount of flow-induced nuclei does not exceed that obtained for the fit with $\alpha_s = 8 \cdot 10^{-6}$ mm^3. Since for the simulation with $\alpha_s = 8 \cdot 10^{-6}$ mm^3 no second upswing in extensional viscosity is seen, there is also no upswing for the simulation with the X-ray model ($\alpha_s = 8 \cdot 10^{-7}$ mm^3 and $b_s = 0.23$ s^{-1}). This strongly suggests that the linear relation between radiation-based nucleation and time does not hold. To improve the X-ray model, additional research has to be done to determine the relation between X-ray intensity and radiation-based nucleation. Moreover, the flow-induced characterization has been taken from a different iPP. It is likely that these parameters are not suitable for the characterization of the used HMW iPP.

Besides, X-ray radiation does not only cross-link polymers, but it can also cause chain scission and branching [57]. These effects are not taken into account, but can lead to the loss of structural integrity (degradation) and therefore change the rheology. One could take branching into account by adjusting the number of dangling arms at both ends of the backbone q_i in the XPP model via $\nu_i = 2/q_i$. But again, more research has to be done to determine whether these processes are relevant.
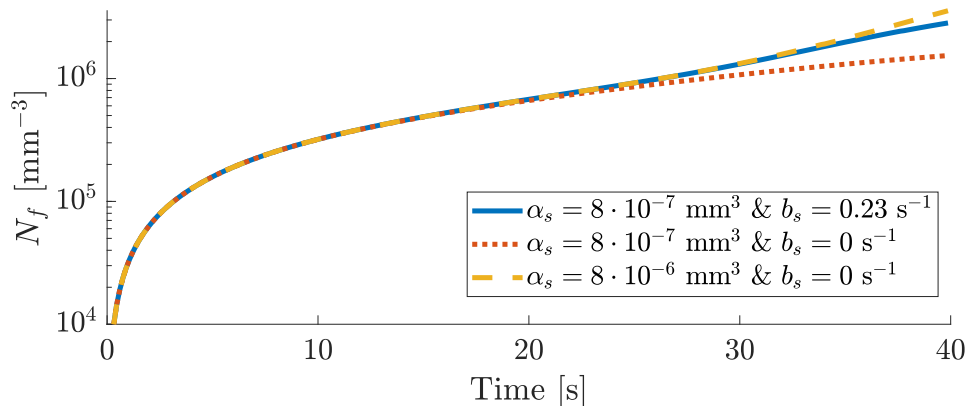

Figure 4.6: Flow-induced nucleation difference N_f as a function of time. The solid line represents the simulations of the X-ray model and the dashed and dotted lines are simulation results without X-ray parameter $b_s t (=0)$. The measurements and simulations were performed at $\dot{\varepsilon} = 0.1$ s^{-1} at $T = 130$ °C.

Unfortunately, it was not possible to give advise about improving the crystallization model given in Chapter 3. This because the HMW iPP used was not fully characterized and the in-situ measurements performed by Pepe et al [16] were not post-processed by the time this report was written. However, with the information available, it can be concluded that the finite element model suffices to capture the rheology and crystallization of iPP extended in a FiSER.

5 Conclusions

A complete numerical tool, reproducing the flow (rheology) and crystallization of crystal structure development of iPP in a FiSER, is presented. In particular, finite element simulations are used that simultaneously solve the crystallization equations (Roozemond et al. [17]), the slightly compressible flow equations, the heat balance and a non-linear viscoelastic constitutive (XPP) model. Also a controller is added to mimic the local uniaxial extensional flow in the FiSER. The simulations are validated by comparing force results with experiments and analytical predictions. The typical force overshoot at the start of a filament stretching experiment, caused by shear effects near the pistons, is also present in the simulations. Therefore, it is possible to investigate the shear effects for the non-linear viscoelastic iPP. To correct for these shear effects, an empirical correlation for the non-linear shear correction factor is derived. This shear correction factor shows good agreement with the simulations and has been validated for two polymers at different strain rates and aspect ratios. Compared to the linear shear correction factors found in literature, the derived shear correction in this study is more accurate (only 3 % error compared to the non-linear simulations).

Next, the crystallization in the FiSER has been studied. From the crystallization simulations it follows that the extensional viscosity increases in steps. The first increase is due to the increase in the Rouse relaxation times during flow. This increase is a result of the increase of nuclei during flow, which are assumed to act as physical cross-links. The second steep increase is a result of crystal growth. During the formation of crystals, a sharp increases in the moduli of the polymer sample can be seen. As a result, the extensional viscosity rapidly increases. Subsequently, the onset of crystallization in a FISER has been investigated. While White et al. [15] found a constant critical crystallization strain at low strain rates, it has been shown that this is not the case for the simulations done in this study for a strain rate range of $\dot{\varepsilon} > 0.71$ s^{-1}. Namely, the critical crystallization strain decreases with increasing strain rate. Besides, an increase in temperature increases the critical crystallization strain. Moreover, due to shear effects, the molecular stretch is not homogeneously distributed over the radius of the filament. As a result of the molecular stretch distribution, the crystallization fraction at the free surface is higher than the crystallization fraction at the centre of the sample, resulting in a distribution of crystallization over the radius of the sample. Because the shear contributions at the pistons are dependent on the initial aspect ratio, it has been shown that the distribution of crystallization fraction can be reduced by increasing the initial aspect ratio. To have a converged critical crystallization strain and only a small distribution of crystallization fraction over the mid-radius of the sample, it is recommended to use an initial aspect ratio of at least $\Lambda_0 = 8.9$ (with $\varepsilon_{pre} = 1.74$). For pure rheological measurements a much lower aspect ratio is required to make the shear contributions disappear in the extensional viscosity. For a sample with $\Lambda_0 = 2.5$ (with $\varepsilon_{pre} = 0.8$), the error due to shear contributions on the extensional viscosity is already less than 5 %. The conclusions above show the beauty of the developed numerical model, since it can be used for other materials as well.

As an example of the application of this numerical code, the effect of X-rays on polymer is investigated. FiSER experiments with in-situ X-ray measurements (performed within our group) has been compared with the simulations. An extension of the model is suggested, where radiation-induced cross-linking is added to the model. Here, it is assumed that nuclei introduced by the X-rays, which act as physical cross-links, are formed proportionally with intensity of the beam and time. It can be seen that the simulation with radiation-induced nucleation shows good agreement with the measurement with a high-intensity X-ray beam before crystallization. By reducing the effect of radiation-induced nucleation in the simulations, the results suggest that the intensity of the beam used in Alba [16] should be reduced by at least a factor 10-100, to eliminate the effect of radiation-induced nucleation on the FiSER measurements. It is recommended to further investigate the effect of radiation on iPP. X-ray radiation does not only cross-link polymers, but can also cause chain scission and branching [57]. These effects are not taken into account, but can lead to the loss of structural integrity (degradation) and therefore change the rheology. One could take branching into account by adjusting the number of dangling arms at both ends of the backbone q_i in the XPP model via $\nu_i = 2/q_i$. But again, additional research has to be done, to determine this relation.

References

[1] E. P. Moore and J. E. Hanser-Gardner. "Polypropylene Handbook". In: *Verlag, Munich* (1996).

[2] A. Peacock. *Handbook of polyethylene: structures: properties, and applications.* CRC Press, 2000.

[3] A. Keller. "A note on single crystals in polymers: Evidence for a folded chain configuration". In: *Philos. Mag.* 2 (1957), pp. 1171–1175. DOI: 10.1080/14786435708242746.

[4] J. D. Hoffman et al. "On the Growth Rate of Spherulites and Axialites from the Melt in Polyethylene Fractions: Regime I and Regime II Crystallization". In: *J. Res. Natl. Bur. Stand. A: Phys. Chem.* 79A (1975), pp. 671–699. DOI: 10.6028/jres.079a.026.

[5] A. Keller. "Crystalline polymers; an introduction". In: *Faraday Discuss. Chem. Soc.* 68 (1979), pp. 145–166. DOI: 10.1039/dc9796800145.

[6] P. Lemstra, N. van Aerle, and C. Bastiaansen. "Chain-extended polyethylene". English. In: *Polymer Journal* 19.1 (1987), pp. 85–98. DOI: 10.1295/polymj.19.85.

[7] T. Kavassalis and P. Sundararajan. "A molecular-dynamics study of polyethylene crystallization". In: *Macromolecules* 26.16 (1993), pp. 4144–4150. DOI: 10.1021/ma00068a012.

[8] J. Hobbs, A. Humphris, and M. Miles. "In-situ atomic force microscopy of polyethylene crystallization. 1. crystallization from an oriented backbone". In: *Macromolecules* 34.16 (2001), pp. 5508–5519. DOI: 10.1021/ma0104478.

[9] Z. Wang, Z. Ma, and L. Li. "Flow-Induced Crystallization of Polymers: Molecular and Thermodynamic Considerations". In: *Macromolecules* 49.5 (2016), pp. 1505–1517. DOI: 10.1021/acs.macromol.5b02688.

[10] S. Kase and T. Matsuo. "Studies on melt spinning. I. Fundamental equations on the dynamics of melt spinning". In: *Journal of Polymer Science Part A: General Papers* 3.7 (1965), pp. 2541–2554. DOI: 10.1002/pol.1965.100030712.

[11] F. N. Cogswell. "Converging flow of polymer melts in extrusion dies". In: *Polymer Engineering & Science* 12.1 (1972), pp. 64–73. DOI: 10.1002/pen.760120111.

[12] M. I. Kolte, H. K. Rasmussen, and O. Hassager. "Transient filament stretching rheometer". In: *Rheologica Acta* 36.3 (1997), pp. 285–302. DOI: 10.1007/BF00366670.

[13] M. Sentmanat. "A novel device for characterizing polymer flows in uniaxial extension". In: *Annual Technical Conference - ANTEC, Conference Proceedings* 1 (Jan. 2003), pp. 992–996.

[14] M. Sentmanat, O. Delgadillo-Velázquez, and S. G. Hatzikiriakos. "Crystallization of an ethylene-based butene plastomer: the effect of uniaxial extension". In: *Rheologica Acta* 49.9 (2010), pp. 931–939. DOI: 10.1007/s00397-010-0461-x.

[15] E. E. Bischoff White, H Winter, and J. Rothstein. "Extensional-flow-induced crystallization of isotactic polypropylene". In: *Rheologica Acta* 51 (2011). DOI: 10.1007/s00397-011-0595-5.

[16] J. Pepe. Personal communication. 2019.

[17] P. C. Roozemond et al. "Modeling flow-induced crystallization in isotactic polypropylene at high shear rates". In: *Journal of Rheology* 59.3 (2015), pp. 613–642. DOI: 10.1122/1.4913696.

[18] P. C. Roozemond, T. B. van Erp, and G. W. Peters. "Flow-induced crystallization of isotactic polypropylene: Modeling formation of multiple crystal phases and morphologies". In: *Polymer* 89 (2016), pp. 69 –80. DOI: 10.1016/j.polymer.2016.01.032.

[19] M. A. Hulsen. *TFEM - A toolkit for the finite element method, Software package.* 2012.

[20] G. Grosso et al. "Modelling of flow induced crystallization of IPP: multiple phases and multiple morphologies". In: *Polymer* (2019). DOI: 10.1016/j.polymer.2019.121806.

[21] J. M. R. Marín et al. "A control scheme for filament stretching rheometers with application to polymer melts". In: *Journal of Non-Newtonian Fluid Mechanics* 194 (2013), pp. 14 –22. DOI: 10.1016/j.jnnfm.2012.10.007.

[22] V Tirtaatmadja and T. Sridhar. "A Filament Stretching Device for Measurement of Extensional Viscosity". In: *Journal of Rheology* 37 (1993), pp. 1081–1102. DOI: 10.1122/1.550372.

[23] S. Spiegelberg, D. C. Ables, and G. Mckinley. "The role of end-effects on measurements of extensional viscosity in filament stretching rheometers". In: *Journal of Non-Newtonian Fluid Mechanics* 64 (1996), pp. 229–267. DOI: `10.1016/0377-0257(96)01439-5`.

[24] J. Housmans et al. "Structure-property relations in molded, nucleated isotactic polypropylene". English. In: *Polymer* 50.10 (2009), pp. 2304–2319. DOI: `10.1016/j.polymer.2009.02.050`.

[25] T. B. van Erp, P. C. Roozemond, and G. W. M. Peters. "Flow-enhanced Crystallization Kinetics of iPP during Cooling at Elevated Pressure: Characterization, Validation, and Development". In: *Macromolecular Theory and Simulations* 22.5 (2013), pp. 309–318. DOI: `10.1002/mats.201300004`.

[26] Q. Huang et al. "Stress relaxation and reversed flow of low-density polyethylene melts following uniaxial extension". In: *Journal of Rheology* 56.6 (2012), pp. 1535–1554. DOI: `10.1122/1.4752759`.

[27] W. M. H. Verbeeten, G. W. M. Peters, and F. P. T. Baaijens. "Numerical simulations of the planar contraction flow for a polyethylene melt using the XPP model". In: *Journal of Non-Newtonian Fluid Mechanics* 117.2 (2004), pp. 73 –84. DOI: `10.1016/j.jnnfm.2003.12.003`.

[28] W. M. H. Verbeeten, G. W. M. Peters, and F. P. T. Baaijens. "Differential constitutive equations for polymer melts: the extended Pom-Pom model". English. In: *Journal of Rheology* 45.4 (2001), pp. 823–843. DOI: `10.1122/1.1380426`.

[29] R. Cardinaels, P. van Puyvelde, and P. Moldenaers. "Evaluation and comparison of routes to obtain pressure coefficients from high-pressure capillary rheometry data". In: *Rheologica Acta* 46.4 (2007), pp. 495–505. DOI: `10.1007/s00397-006-0148-5`.

[30] S. E. Kadijk and B. H.A. A. van den Brule. "On the pressure dependency of the viscosity of molten polymers". In: *Polymer Engineering & Science* 34.20 (1994), pp. 1535–1546. DOI: `10.1002/pen.760342004`.

[31] D. Acierno et al. "Rheological and heat transfer aspects of the melt spinning of monofilament fibers of polyethylene and polystyrene". In: *Journal of Applied Polymer Science* 15.10 (1971), pp. 2395–2415. DOI: `10.1002/app.1971.070151007`.

[32] C. Hirt, A. Amsden, and J. Cook. "An arbitrary Lagrangian-Eulerian computing method for all flow speeds". In: *Journal of Computational Physics* 14.3 (1974), pp. 227–253. DOI: `10.1016/0021-9991(74)90051-5`.

[33] N. Jaensson, M. Hulsen, and P. Anderson. "Stokes-Cahn-Hilliard formulations and simulations of two-phase flows with suspended rigid particles". In: *Computers and Fluids* 111 (2015), pp. 1–17. DOI: `10.1016/j.compfluid.2014.12.023`.

[34] G. D'Avino, M. Hulsen, and P. Maffettone. "Decoupled transient schemes for viscoelastic fluid flow with inertia". English. In: *Computers and Fluids* 66 (2012), pp. 183–193. DOI: `10.1016/j.compfluid.2012.06.023`.

[35] A. Bogaerds. "Stability analysis of viscoelastic flows". English. PhD thesis. Technical University of Eindhoven, 2002. DOI: `10.6100/IR558902`.

[36] A. N. Brooks and T. J. Hughes. "Streamline upwind/Petrov-Galerkin formulations for convection dominated flows with particular emphasis on the incompressible Navier-Stokes equations". In: *Computer Methods in Applied Mechanics and Engineering* 32.1 (1982), pp. 199 –259. DOI: `10.1016/0045-7825(82)90071-8`.

[37] M. A. Hulsen, R. Fattal, and R. Kupferman. "Flow of viscoelastic fluids past a cylinder at high Weissenberg number: Stabilized simulations using matrix logarithms". In: *Journal of Non-Newtonian Fluid Mechanics* 127.1 (2005), pp. 27–39. DOI: `10.1016/j.jnnfm.2005.01.002`.

[38] N. Jaensson. "Handling small relaxation times in multi-mode viscoelastic fluid flow". In: *A toolkit for the finite element method, TFEM user's guide by Hulsen, M.* (2014), pp. 106–109.

[39] J. K. Nielsen, H. K. Rasmussen, and O. Hassager. "Stress relaxation of narrow molar mass distribution polystyrene following uniaxial extension". In: *Journal of Rheology* 52.4 (2008), pp. 885–899. DOI: `10.1122/1.2930872`.

[40] H. K. Rasmussen et al. "Experimental evaluation of the pure configurational stress assumption in the flow dynamics of entangled polymer melts". In: *Journal of Rheology* 54.6 (2010), pp. 1325–1336. DOI: `10.1122/1.3496378`.

[41] C. Navier. "Mémoire sur les lois du mouvement des fluides". In: *Mémoires de l'Académie Royale des Sciences de l'Institut de France* 6.1823 (1823), pp. 389–440.

[42] R. B. Bird. "Useful Non-Newtonian Models". In: *Annual Review of Fluid Mechanics* 8.1 (1976), pp. 13–34. DOI: `10.1146/annurev.fl.08.010176.000305`.

[43] X.-M. Zhang et al. "Rheological properties and morphological evolutions of polypropylene/ethylene-butene copolymer blends". In: *Polymer Engineering & Science* 52.8 (2012), pp. 1740–1748. DOI: `http://dx.doi.org/10.1002/pen.23116`.

[44] M. van Drongelen. "Structure development in semi-crystalline polymers under processing conditions : an experimental approach". English. PhD thesis. Department of Mechanical Engineering TU/e, 2015. ISBN: 978-90-386-3867-6.

[45] P. C. Roozemond et al. "Multimorphological Crystallization of Shish-Kebab Structures in Isotactic Polypropylene: Quantitative Modeling of Parent-Daughter Crystallization Kinetics". In: *Macromolecules* 47.15 (2014), pp. 5152–5162. DOI: `10.1021/ma501108c`.

[46] V. B. F. Mathot and M. F. J. Pijpers. "Heat capacity, enthalpy and crystallinity for a linear polyethylene obtained by DSC". In: *Journal of thermal analysis* 28.2 (1983), pp. 349–358. DOI: `10.1007/BF01983270`.

[47] E Troisi, H J. M. Caelers, and G. Peters. "Full Characterization of Multiphase, Multimorphological Kinetics in Flow-Induced Crystallization of IPP at Elevated Pressure". In: *Macromolecules* 50 (2017), pp. 3868–3882. DOI: `10.1021/acs.macromol.7b00595`.

[48] M. Arif, N. Kalarikkal, and S. Thomas. "Chapter 1 - Introduction on Crystallization in Multiphase Polymer Systems". In: *Crystallization in Multiphase Polymer Systems.* Ed. by M. Arif, B. Gowd, and N. Kalarikkal. Elsevier, 2018, pp. 1 –16. ISBN: 978-0-12-809453-2. DOI: `10.1016/B978-0-12-809453-2.00001-3`.

[49] L. Hanna et al. "Vibrational spectroscopic study of structural changes in isotactic polypropylene below the melting point". In: *Polymer* 29.10 (1988), pp. 1843 –1847. DOI: `10.1016/0032-3861(88)90401-6`.

[50] S. L. Wingstrand et al. "Influence of Extensional Stress Overshoot on Crystallization of LDPE". In: *Macromolecules* 50.3 (2017), pp. 1134–1140. DOI: `10.1021/acs.macromol.6b02543`.

[51] W Schneider, A Köppl, and J Berger. "Non-Isothermal Crystallization of Polymers: System of Rate Equations". In: *International Polymer Processing* 2.3-4 (1988), pp. 151–154. DOI: `10.3139/217.880150`.

[52] H. Zuidema, G. W. M. Peters, and H. E. H. Meijer. "Development and Validation of a Recoverable Strain-Based Model for Flow-Induced Crystallization of Polymers". In: *Macromolecular Theory and Simulations* 10.5 (2001), pp. 447–460. DOI: `10.1002/1521-3919(20010601)10:5<447::AID-MATS447>3.0.CO;2-C`.

[53] R. J. A. Steenbakkers and G. W. M. Peters. "A stretch-based model for flow-enhanced nucleation of polymer melts". In: *Journal of Rheology* 55.2 (2011), pp. 401–433. DOI: `10.1122/1.3545844`.

[54] L. Fernandez-Ballester et al. "Effect of Long Chains on the Threshold Stresses for Flow-Induced Crystallization in iPP: Shish Kebabs vs Sausages". In: *Macromolecules* 45 (2012), 6557–6570. DOI: `10.1021/ma3000384`.

[55] J. Juanhuix et al. "Developments in optics and performance at BL13-XALOC, the macromolecular crystallography beamline at the ALBA synchrotron". In: *Journal of synchrotron radiation* 21.4 (2014), pp. 679–689. DOI: `10.1107/S160057751400825X`.

[56] A. Charlesby. "Chapter 9 - The properties of a crosslinked network". In: *Atomic Radiation and Polymers.* Ed. by A. Charlesby. Vol. 1. International Series of Monographs on Radiation Effects in Materials. Pergamon, 1960, pp. 134 –158. ISBN: 978-1-4831-9776-0. DOI: `10.1016/B978-1-4831-9776-0.50013-9`.

[57] H. Otaguro et al. "High-energy radiation forming chain scission and branching in polypropylene". In: *Radiation Physics and Chemistry* 79.3 (2010), pp. 318 –324. DOI: `10.1016/j.radphyschem.2009.11.003`.

Summary

A wide range of techniques can be used to obtain information about the rheological properties of polymers. In this work, the filament stretching rheometer is studied. This type of rheometer is used to characterize molten polymers in a pure uniaxial extensional flow. Although the flow at the midfilament region is controlled to be pure uniaxial extension, shear contributions near the plates can affect the measured force signal. In this paper, these shear contributions are investigated by means of finite element simulations. To model the non-linear viscoelastic flow behaviour of polymers, the extended pom-pom constitutive equation is used. The work presented in this paper aims at developing a correction factor for the shear contributions in non-linear viscoelastic materials. For this purpose, a set of simulations on isotactic polypropylene are performed in which different temperatures, strain rates and initial aspect ratios (geometries) have been used. To correct for the shear contributions shown in these simulations, a new empirically shear correction factor is developed. It turns out that the developed shear correction factor shows good agreement with the simulated shear correction factors of isotactic polypropylene. Moreover, the developed shear correction factor has been validated for two polymers which show completely different rheological behaviour.

Besides, the extensional flow-induced crystallization of isotactic polypropylene in a filament stretching rheometer has been modelled. Finite element simulations are developed which can capture the rheology and crystallization of isotactic polypropylene in a filament stretching rheometer. A broad range of processing conditions have been investigated by varying the initial temperature and the applied strain rate. From these simulations it follows that the extensional viscosity increases in steps. The first increase is due to the increase in the Rouse relaxation times during flow. This increase is a result of the increase of nuclei during flow, which are assumed to act as physical cross-links. The second steep increase is a result of crystal growth. During the formation of crystals, a sharp increases in the moduli of the polymer sample can be seen. As a result, the extensional viscosity rapidly increases. While White et al. [15] found a constant critical crystallization strain at low strain rates, it has been shown that this is not the case for the simulations done in this study for a strain rate range of $\dot{\varepsilon} > 0.71$ s^{-1}. Namely, the critical crystallization strain decreases with increasing strain rate. Besides, an increase in temperature increases the critical crystallization strain. Before crystallization, the shear contributions at the pistons affect the flow in such a way that no pure uniaxial extensional flow is present in the filament stretching rheometer. Therefore, the molecular stretch is not homogeneously distributed over the radius of the filament. The molecular stretch determines the amount of flow-induced nuclei and therefore affects the onset of crystallization. As a result of the molecular stretch distribution, the crystallization fraction at the free surface is higher than the crystallization fraction at the centre of the sample, resulting in a distribution of crystallization over the radius of the sample. Because the shear contributions at the pistons are dependent on the initial aspect ratio, it has been shown that the distribution of crystallization fraction can be reduced by increasing the initial aspect ratio. Subsequently, the effect of the initial aspect ratio on the critical crystallization strain has been studied. It was found that an initial aspect ratio of at least $\Lambda_0 = 8.9$ has to be used to perform proper in-situ crystallization measurements in the filament stretching rheometer. These measurements then only contain a small distribution of the crystallization fraction over the mid-radius of the sample.

Furthermore, a first attempt has been made to model radiation-induced cross-linking of a high-molecular-weight isotactic polypropylene in a filament stretching rheometer. This is done by assuming that the radiation-induced nuclei increase proportionally with intensity of the X-ray beam and proportionally with time. By fitting simulations on measurments with and without X-ray beam, the suggested model has been tested. Finally, an estimation has been made to predict the effect of X-ray beam intensity on the extensional viscosity of a high-molecular-weight isotactic polypropylene. The beauty of the developed numerical model is that it can be used for multiple materials, geometries, strain rates and temperatures. Therefore, it is applicable in a wide range of filaments stretching experiments. Moreover, it is possible to simulate complex physical phenomena like flow-induced nucleation and crystallization and radiation-based cross-linking with the developed numerical model.

Samenvatting

Een breed scala aan technieken kan worden gebruikt om informatie over de eigenschappen van polymeren te verkrijgen. In dit artikel wordt de "filament stretching rheometer" bestudeerd. Dit type reometer wordt gebruikt om polymeren te karakteriseren in een pure uniaxiale rekstroming. Het nadeel van deze reometer is dat contributies van afschuiving de rekstroming in de buurt van de platen kunnen beïnvloeden. In dit artikel worden deze afschuifbijdragen onderzocht door middel van eindige-elementen simulaties. Om het niet-lineaire visco-elastisch gedrag van polymeren te modelleren wordt de "extended pom-pom" constitutieve vergelijking gebruikt. Het werk dat in dit artikel wordt gepresenteerd is gericht op het ontwikkelen van een correctiefactor voor de afschuifcontributies in niet-lineaire visco-elastische materialen. Hiervoor worden een set simulaties van een isotactisch polypropyleen uitgevoerd, waarin verschillende temperaturen, reksnelheden en initiële aspect ratio's (geometrieën) gebruikt zijn. Het blijkt dat de ontwikkelde correctiefactor voor afschuiving overeenkomt met de gesimuleerde correctiefactoren voor afschuiving van isotactisch polypropyleen. Bovendien is de ontwikkelde correctiefactor gevalideerd voor twee polymeren die volledig verschillend reologisch gedrag vertonen.

Daarnast is kristallisatie geïnduceerd door extensieve stroming van isotactisch polypropyleen in een "filament stretching rheometer" gemodelleerd. Er zijn eindige-elementen simulaties ontwikkeld die de reologie en kristallisatie van isotactisch polypropyleen kunnen beschrijven in de "filament stretching rheometer". Een aantal procescondities zijn onderzocht door de begintemperatuur en de toegepaste reksnelheid te variëren. Uit deze simulaties volgt dat de rekviscositeit in stappen toeneemt. De eerste toename is te wijten aan de toename van de Rouse relaxatietijden tijdens flow. Deze toename is een gevolg van de toename van het aantal nuclei tijdens stroming, waarvan wordt aangenomen dat ze fungeren als fysische cross-links. De tweede steile toename is een gevolg van kristallisatie; de vorming van kristallen verhoogt de moduli van het polymeer. Als gevolg hiervan neemt de rekviscositeit snel toe. Terwijl White et al. [15] een constante kritische kristallisatie rek vonden bij lage reksnelheden, is het aangetoond dat dit niet het geval is voor de simulaties die in deze studie zijn gedaan voor reksnelheden van $\dot{\varepsilon} > 0.71$ s^{-1}. Het blijkt dat de kritische kristallisatie rek afneemt met toenemende reksnelheid. Bovendien zorgt een toename van de temperatuur voor een toename van de kritische kristallisatie rek.

Voorafgaand aan kristallisatie beïnvloeden de afschuifcontributies de stroming zodanig dat er geen pure uniaxiale rekstroming aanwezig is in de reometer. Daarom is de moleculaire rek niet homogeen verdeeld over de straal van het filament. De moleculaire rek bepaalt de hoeveelheid door stroming geïnduceerde nuclei en beïnvloedt daarom het begin van kristallisatie. Als gevolg van de moleculaire rekverdeling is de kristallisatiefractie aan het vrije oppervlak hoger dan de kristallisatiefractie in het midden van het filament. Dit resulteert in een verdeling van de kristallisatie over de straal van het filament. De contributie van afschuiving is afhankelijk van de initiële aspect ratio. Er is aangetoond dat de verdeling van de kristallisatiefractie kan worden verminderd door de initiële aspect ratio te vergroten. Vervolgens is het effect van de initiële aspect ratio op de kritische kristallisatie rek onderzocht. Hieruit volgde dat een initiële aspect ratio van ten minste 8.9 moet worden gebruikt om goede in-situ kristallisatiemetingen uit te voeren in de "filament stretching rheometer". Deze metingen bevatten dan slechts een kleine verdeling van de kristallisatiefractie over de straal in het midden van het filament.

Verder is een eerste poging gedaan om de door straling geïnduceerde cross-links van een isotactisch polypropyleen met een hoog moleculair gewicht te modelleren. Dit wordt gedaan door aan te nemen dat de door straling geïnduceerde nuclei evenredig toenemen met de intensiteit van de X-rays en de tijd. Door simulaties te fitten op metingen met en zonder X-rays is het voorgestelde model getest. Ten slotte is een schatting gemaakt om het effect van de intensiteit van de X-rays op de rekviscositeit van een isotactisch polypropyleen met hoog moleculgewicht te voorspellen. Het mooie van dit numerieke model is dat het te gebruiken is voor meerdere materialen, geometrieën, reksnelheden en temperaturen. Daarom kan dit model gebruikt worden om voorspellingen te doen over een breed scala van "filament stretching experiments". Overigens is het mogelijk om ingewikkelde fysische fenomenen zoals kristallisatie geïnduceerd door stroming en het effect van radiatie op polymeren te simuleren met dit model.

Dankwoord

Deze thesis was er nooit gekomen zonder de unieke samenwerking binnen de Polymer Technology groep en de steun van naasten. Daarom wil ik van deze gelegenheid gebruik maken om een aantal personen te bedanken.

Als eerste natuurlijk Ruth. In de afgelopen periode hebben we regelmatig meetings gehad. Ik waardeer het dat u hier zo veel tijd voor vrij heeft gemaakt. U heeft er mede voor gezorgd dat dit numeriek project ook experimentele relevantie heeft. Bedankt voor het gestelde vertrouwen om mij ook regelmatig mijn eigen plan te laten trekken. Patrick, ook u bedankt voor de bijdrage aan deze thesis en de tijd die u hiervoor vrij gemaakt heeft. Als ik vragen had, over onder andere numerieke kwesties, kon ik altijd bij u terrecht. Daarnaast wil ik Martien, Michelle en Caroline bedanken voor het verhelpen van vele numerieke problemen en hun contributies aan de modules in TFEM die ik gebruikt heb.

Het grootste deel van mijn afstuderen heb ik toch wel doorgebracht in kantoor-kelder 0.05. Zonder alle namen te noemen wil ik dan ook alle (oud-)kantoorgenoten bedanken voor de samenwerking, discussies, leuke humor en slechte humor. Zonder onze dartsessies, het hartenjagen en borrels zou ik nu nog steeds tegen mijn computer aan het praten zijn.

Besides, I would like to thank Jessica. Many thanks for all experimental results with the FiSER and the discussions we had about crystallization and radiation-induced cross-linking of iPP. Giovanna, thanks for the opportunity to use and modify the crystallization module you wrote in TFEM.

Verder wil ik ook mijn vriendin bedanken. Vera, welke plannen voor werk of studie ik ook heb, op jou steun, hulp en interesse kan ik altijd rekenen. Dit heb je ook tijdens dit project weer laten zien en daar ben ik je heel dankbaar voor. Ten slotte wil ik mijn vrienden in Lieshout en daarbuiten bedanken die zich wat minder bezighouden met polymeren, maar wat afleiding en gezelligheid buiten het werk is tenslotte ook belangrijk. Hopelijk volgen er nog vele leuke avonden in de kantine, op stap en op feestjes.

Eindhoven, October, 2019